

Copyright Undertaking

This thesis is protected by copyright, with all rights reserved.

By reading and using the thesis, the reader understands and agrees to the following terms:

- 1. The reader will abide by the rules and legal ordinances governing copyright regarding the use of the thesis.
- 2. The reader will use the thesis for the purpose of research or private study only and not for distribution or further reproduction or any other purpose.
- 3. The reader agrees to indemnify and hold the University harmless from and against any loss, damage, cost, liability or expenses arising from copyright infringement or unauthorized usage.

IMPORTANT

If you have reasons to believe that any materials in this thesis are deemed not suitable to be distributed in this form, or a copyright owner having difficulty with the material being included in our database, please contact lbsys@polyu.edu.hk providing details. The Library will look into your claim and consider taking remedial action upon receipt of the written requests.

SYNERGETIC-ENGINEERED ALL VAN DER WAALS PHOTODIODES FOR FAST-BROADBAND PHOTODETECTION AND MULTIFUNCTIONAL OPTOELECTRONICS

TAWSIF IBNE ALAM

PhD

The Hong Kong Polytechnic University

2025

The Hong Kong Polytechnic University Department of Applied Physics

Synergetic-engineered All van der Waals photodiodes for fast-broadband photodetection and Multifunctional Optoelectronics

Tawsif Ibne Alam

A thesis submitted in partial fulfilment of the requirements for the degree of Doctor of Philosophy

December 2024

Certificate of Originality

I hereby declare that this thesis is my own work and that, to the best of my knowledge and belief, it reproduces no material previously published or written, nor material that has been accepted for the award of any other degree or diploma, except where due acknowledgement has been made in the text.

_____(Signed)

Tawsif Ibne Alam (Name of Student)

To my mom, dad, sister and lovely wife

Abstract

In this report, a multifactorial study of van der Waals (vdW) photodiodes was conducted, with the aim of suppressing dark currents for ultra-low light detection, structural and contact optimization for efficient synergistic engineering of GaS-WSe₂ all van der Waals (a-vdW) photodiodes. The term "all van der Waals" in this study signifies the integration of the metal contacts using van der Waals technique. The synergistically optimized device exhibit broadband detection; 275 nm - 1064 nm, multispectral unity approaching linearity, alongside a substantial LDR of 106.78 dB. Additionally, the photodiode achieve a remarkable on/off ratio of 10^5 and rapid response edges of $545 \mu s/471 \mu s$, exhibiting ultra-low light detection capabilities, with dark currents in the fA range, culminating in a peak responsivity of 376.78 mA/W and a detectivity of 4.12 × 10¹¹ Jones, complemented by a EQE of 30% and a fill factor of ~ 0.33 -all achieved through a single junction. For the first time, based on our analysis of multiple a-vdW devices and traditional electron beam lithography (EBL) patterned device, we highlight the importance of fermi-level pinning (FLP) free metal-2D interface engineering for GaS based photodiodes, that enables effective modulation of the Schottky barrier height via vdW metal contacts and employ meticulous thickness-engineered layers in developing a robust depletion region within the type-II GaS-WSe₂ heterojunction, ultimately achieving a favorable balance among photocarrier generation-recombination, separation, transport, and extraction.

We analyze and compare key figure of merits such as power exponent α and recombination order β and its evolution in multiple devices to achieve near unity value in a-vdW device, portraying recombination-trapping resilient operation, while a similar device having patterned with EBL shows significant degradation to the value of α . This suggests most of the recombination-trapping and degradation of performance occurs at the metal-2D interface, asserting our claim of renewed thinking for contact integration strategies to 2D photodiodes. Additionally, power conversion efficiency analysis along with the measured fermi-level

alignment at the heterojunction of our a-vdW devices suggest the importance of achieving the perfect thickness engineered layers for realizing a robust p-n junction, balancing photocarrier generation-recombination, separation, transport, and extraction.

Moreover, due to the excellent photovoltaic performance of the photodiode, it was utilized for demonstration of multi-band imaging applications as a single pixel detector. Additionally, owing to the FLP free metal contacts, excellent gate tunable open circuit voltage was achievable and the device was utilized for demonstration of gate tunable optoelectronic logic AND gate, paving the way for a single device to be used for multi-functional optoelectronics.

Additionally, Schottky junction based Gr-GaS-Au photodiodes fabricated utilizing the a-vdW method demonstrated a novel double spiking photocurrent temporal response like that of pyroelectric detectors, under ultra-low light conditions, with a maximum spiking responsivity of 0.7A/W, with rise and fall time of 15ms and 36 ms respectively.

Our comprehensive investigation not only advances the understanding of a-vdW heterojunction photodiodes from the perspective of contact induced FLP degradation and meticulous thickness engineering, especially for moderately wide bandgap like GaS based devices, but also sets the stage for renewed thinking of contact integration strategy specially for large area industrial scale future developments in critically engineered next generation vdW optoelectronics.

List of Publications

- Tawsif Ibne Alam, Sumaiya Umme Hani, Zongliang Guo, Safayet Ahmed, Ahmed Mortuza Saleque, Md. Nahian Al Subri Ivan, Shuvra Saha and Yuen Hong Tsang.
 "Synergistically-engineered all van der Waals GaS-WSe2 photodiodes: Approaching near unity polychromatic linearity for multi-functional optoelectronics". Small 2025.
 DOI: 10.1002/sml1.202410841
- 2. Tawsif Ibne Alam, Sumaiya Umme Hani, and Yuen Hong Tsang. "Synergetic engineered all van der Waals photodetectors for robust photodetection". Proc. SPIE 13368, 2D Photonic Materials and Devices VIII, (2025)
- **3.** Tawsif Ibne Alam, Kunxuan Liu, Sumaiya Umme Hani, Safayet Ahmed and Yuen Hong Tsang. "Advances in Group-10 Transition Metal Dichalcogenide PdSe₂-Based Photodetectors: Outlook and Perspectives". *Sensors* **2024**, *24*, 6127.

DOI: 10.3390/s24186127

4. Tawsif Ibne Alam, Sumaiya Umme Hani, Safayet Ahmed and Yuen Hong Tsang. "All van der Waals Photodetector for Ultralow Dark Current". Proc. SPIE 12888, 2D Photonic Materials and Devices VII, 128880A (12 March 2024)

DOI: 10.1117/12.3017997

- 5. Zongliang Guo, Hao Cheng, Ming Yang, Chi Ho Wong, Tawsif Ibne Alam, Shu Ping Lau, and Yuen Hong Tsang* "Phase-pure 1T' Molybdenum Disulfide Synthesis and Stabilization", *Small Science* (2025). DOI:10.1002/smsc.202500107
- 6. Sumaiya Umme Hani, Tawsif Ibne Alam, and Yuen Hong Tsang. "Nonlinear Optical Activities in Van der Waals Ternary Transition Metal Dichalcogenides" Proc. SPIE 13368, 2D Photonic Materials and Devices VIII, (2025)
- Sumaiya Umme Hani, Safayet Ahmed, Tawsif Ibne Alam, Ahmed Mortuza Saleque,
 Md. Nahian Al Subri Ivan, Shuvra Saha, Linli Xu and Yuen Hong Tsang "Germanium-

- based Ternary Chalcogenide: An Emerging low-dimensional Material for Nonlinear Optics and Ultrafast Photonics" *Applied Materials Today* **42** (2025) 102555 **DOI:** 10.1016/j.apmt.2024.102555
- 8. Sumaiya Umme Hani, Safayet Ahmed, Tawsif Ibne Alam, and Yuen Hong Tsang, "Nonlinear optical responses of ternary 2D GeSeTe nanosheets in NIR regime". Proc. SPIE 12888, 2D Photonic Materials and Devices VII, 1288809 (12 March 2024).
 DOI: 10.1117/12.3015104
- 9. Safayet Ahmed, Yiyu Gan, Ahmed Mortuza Saleque, Honglei Wu, Junpeng Qiao, Md. Nahian Al Subri Ivan, Sumaiya Umme Hani, Tawsif Ibne Alam, Qiao Wen and Yuen Hong Tsang, "2D Semi-metallic Hafnium Ditelluride: A Novel Nonlinear Optical Material for Ultrafast and Ultranarrow Photonics Applications", Small Methods 2024, 8, 2300239. DOI: 10.1002/smtd.202300239
- 10. Nahian Al Subri Ivan, Ahmed Mortuza Saleque, Safayet Ahmed, Zong Liang Guo, Zu Di, Linli Xu, Tawsif Ibne Alam, Sumaiya Umme Hani, Yuen Hong Tsang. "Jute stick derived self-regenerating sustainable solar evaporators with different salt mitigation mechanisms for highly efficient solar desalination"- Journal of Materials Chemistry A (RSC Publishing). 8, 2023. DOI: 10.1039/D2TA08237C
- 11. Ahmed Mortuza Saleque, Shuvra Saha, Md Nahian Al Subri Ivan, Safayet Ahmed, Tawsif Ibne Alam, Sumaiya Umme Hani, Yuen Hong Tsang," Reduced graphene oxide/TiTe2 quantum dot coated waste face mask recycled for highly efficient solar steam generation". Solar Energy Materials and Solar Cells, (253) 2023, 112232, DOI: 10.1016/j.solmat.2023.112232.
- 12. Safayet Ahmed, Ping Kwong Cheng, Junpeng Qiao, Wei Gao, Ahmed Mortuza Saleque, Md. Nahian Al Subri Ivan, Ting Wang, Tawsif Ibne Alam, Sumaiya Umme Hani, Zong Liang Guo, Siu Fung Yu, and Yuen Hong Tsang "Nonlinear Optical Activities in Two-

- Dimensional Gallium Sulfide: A Comprehensive Study". **ACS Nano 2022** 16 (8), 12390-12402, **DOI:** 10.1021/acsnano.2c03566
- 13. Md. Nahian Al Subri Ivan, Ahmed Mortuza Saleque, Safayet Ahmed, Ping Kwong Cheng, Junpeng Qiao, Tawsif Ibne Alam, and Yuen Hong Tsang, "Waste Egg Tray and Toner-Derived Highly Efficient 3D Solar Evaporator for Freshwater Generation"; ACS Applied Materials & Interfaces 2022 14 (6), 7936-7948, DOI: 10.1021/acsami.1c22215
- 14. Safayet Ahmed, Junpeng Qiao, Ping Kwong Cheng, Ahmed Mortuza Saleque, Md. Nahian Al Subri Ivan, Tawsif Ibne Alam, and Yuen Hong Tsang, "Two-Dimensional Gallium Sulfide as a Novel Saturable Absorber for Broadband Ultrafast Photonics Applications", ACS Applied Materials & Interfaces 2021 13 (51), 61518-61527, DOI: 10.1021/acsami.1c18155

Acknowledgements

"All praises are for ALLAH—Lord of the worlds, the Most Beneficent, the Most Merciful. Master of the day of judgement. You 'alone' we worship and You 'alone' we ask for help." (Chapter 1, Al-Quran, Verse: 1-5)

First and foremost, I would like to thank God Almighty Allah for HIS countless blessings, providing me with wisdom, good health, patience and perseverance to navigate through this journey of doctoral study.

I would like to express my sincere gratitude to my supervisor, Prof. Yuen Hong Tsang, for the opportunity to work on these engaging projects. I am profoundly thankful for his unwavering support, both in my research and in personal matters, which has continually motivated me to stay focused. I appreciate his efforts in securing research funding and facilitating insightful discussions, allowing me to explore previously uncharted topics. His encouragement during challenging times has been invaluable, inspiring me to maintain a positive outlook even amidst setbacks.

I would like to extend my heartfelt thanks to my colleagues, particularly Mr. Zongliang Guo and Mr. Jianmin Yan, for their generous support in helping me pickup technical equipment skills during the first year of my doctoral studies. I am also grateful to my other group members, Dr. Safayet Ahmed and Dr. Ahmed Mortuza Saleque, for their assistance and encouragement during the first year of my PhD.

I would like to express my gratitude to my instructors, Prof. Jiyan Dai, Prof. S.P. Lau, Dr. Ye Zhu, Prof. Yang Chai, and Dr. Jiong Zhao, for their insightful discussions and guidance, which have greatly enriched my learning experience.

I also wish to thank the staff members: Dr. Wei Lu from the Center for Atomic Electron Microscopy, Dr. Hon Fai Wong from the AP Department, Dr. Hardy Lui, and Ms. Pendy Ho from the Materials Research Center, as well as Dr. Terrence Wong from the Clean Room. Their training sessions and ongoing support in operating the equipment have significantly facilitated access to essential resources for my research.

I would like to extend my gratitude to The Hong Kong Polytechnic University, the Department of Applied Physics, the Materials Research Center, and the Center for Atomic Electron Microscopy for providing the research facilities that enabled me to learn and apply my knowledge for the benefit of humanity. Additionally, I am thankful to the University Grants Commission (UGC) of Hong Kong for funding my research studies through the Hong Kong PhD Fellowship Scheme (HKPFS). The support has been instrumental in my academic journey.

I would like to express my heartfelt gratitude to my loving mom, dad, sister, in-laws, and extended family members for their unwavering motivation, support, and prayers throughout my doctoral research journey.

Lastly, I want to sincerely appreciate my wonderful and caring wife, who has been a constant source of support during both the highs and lows of this journey. Despite her own commitments as a PhD student, she has taken care of me, prepared our meals, and managed household tasks, easing my burden. Additionally, she has been a patient listener to my endless stream of research-related ideas, for which I am incredibly grateful.

Table of Contents

Certificate of Originality
AbstractIII
List of PublicationsV
AcknowledgementsVIII
Table of ContentsX
List of Figures:XIV
List of Tables:XXIII
Chapter 1: Introduction:1
1.1. Background and Motivation:1
1.2. Rationale:
1.3. Accomplishments presented in this thesis:
1.4. Thesis outline4
Chapter 2: van der Waals optoelectronics: Overview and Synergistic Optimization
Prospects 6
2.1. Introduction:6
2.2. Overview on 2D layered materials:6
2.3. Figure of merits (FoM) for photodetectors:9
2.4. Broad Classification of vdW-m based Photodetectors
2.4.1. Photovoltaic Type Photodetectors
2.4.2. Photoconductive and Photo-Gated Photodetectors
2.4.3. Photothermoelectric (PTE) Photodetectors:

2.4.4.	Photobolometric Photodetectors
2.5. Syr	nergetic optimized strategies considered in this thesis:
2.5.1.	Contact engineering and its influence on optoelectronic device performance:16
2.5.2.	Route to weakened FLP and efficient charge injection and extraction:22
2.5.3.	Strategy for obtaining ultra-low dark currents:
2.5.4.	Utilizing Band Alignment Engineering for dark current suppression:32
2.5.5.	Utilizing localized field modulation induced suppression of dark currents:34
2.5.6.	Repression of trap state induced dark current utilizing interfacial engineering:
	35
2.5.7.	Role of underlying substrate on ultra-thin 2DLM:
2.5.8.	Role of layer thickness on position of fermi-level:37
2.6. Con	nclusion:
Chapter 3:	All van der Waals GaS-WSe2 photodiodes: Synergistically engineered for
Multifunction	nal Optoelectronics:
3.1. Intr	roduction:40
3.2. Res	sults and Discussion:42
3.2.1.	Fabrication of heterojunction:
3.2.2.	Van der Waals contact fabrication and integration:
3.2.3.	Raman and Photoluminescence spectroscopic characterization of the
heteroju	nction:45
3.2.4.	Estimation of band structure profile using UPS and KPFM and height profile
using AI	FM:47

3.2.5.	HR-STEM and HAADF-STEM EDX analysis at the cross-section of a-vdw
heteroju	nction:49
3.2.6.	Electronic transport characteristics of the GaS-WSe ₂ a-vdW photodiode under
dark cor	aditions:
3.2.7.	Charge Transport of the device under illumination conditions:53
3.2.8.	Employment of synergistic device optimization strategies:54
3.2.9.	Optoelectronic characteristics of the Synergistically engineered a-vdW
photodic	ode:
3.2.10.	Comparative performance analysis of the synergistic-engineered photodiodes
	73
3.2.11.	Gate tunable optoelectronic response of the device:
3.2.12.	Potential application in multi-functional optoelectronics:
3.2.13.	Summary Comparison of Key Performance parameters for all fabricated
devices:	83
3.2.14.	Comparison of synergistically engineered photodiode to reported high
perform	ance photodetector devices:
3.2.15.	Comparison of synergistically engineered photodiode to reported high
perform	ance vdW solar cell devices:85
3.3. Con	nclusion:85
Chapter 4:	Graphene contacted GaS all van der Waals photodiodes87
4.1. Inti	oduction: 87
4.2. Gr-	GaS-Au a-vdW heterojunction diode:87
4.2.1.	Fabrication and Characterization of the a-vdW Gr-GaS-Au photodetector:87

4.2.2	2. O ₁	ptoelectronic Characterization of the device:	.89
4.3.	Conclu	sion:	.93
Chapter 5	5: Co	onclusion and Future work:	.94
5.1.	Summa	ary of investigation presented in this thesis:	.94
5.2.	Future	Work: Gr-GaS-WSe ₂ based ultra-efficient photodiodes	.95
5.2.1	l. Fa	abrication of a-vdW Gr-GaS-WSe2 heterojunction:	.96
5.2.2	2. Cl	haracterization of the heterojunction:	.97
5.2.3	3. O ₁	ptoelectronic characteristics of the a-vdW Gr-GaS-WSe ₂ heterojunction:	.99
5.3.	Conclu	sion1	04
Appendix	:		06
Dafaranaa	26	1	111

List of Figures:

Figure 1. 2DLM Family and their corresponding characteristic classification [18]7
Figure 2. Spectral Response of some 2-D materials used in photodetection [19]
Figure 3. Broad classification of vdW-m photodetectors and their outlying internal
mechanisms
Figure 4. Energy band alignment in a typical (a) p-n junction (b) Schottky junction. (c) Typical
I _d -V _d characteristics of a photovoltaic-type photodetector.[19]12
Figure 5.(a) Typical photoconductive effect in a vdW-m based photodetector. The band bending
and charge carrier extraction process requires an applied external bias voltage. (b) I_d - V_d
characteristics of a typical photoconductive photodetector. Typical photogated photodetector
showing (c) n-type characteristics due to p-type charge trapping and (d) p-type characteristics
due to n-type charge trapping. I_d - V_g characteristics of a typical (e) ambipolar photoconductive
photodetector, (f) n-type carrier dominant photodetector and (g) p-type carrier dominant
photodetector.[19]13
Figure 6. Typical PTE photodetector. Localized light spot (green color) generates a temperature
Figure 6. Typical PTE photodetector. Localized light spot (green color) generates a temperature gradient across the entire vdW-m channel material, from the drain to source electrodes,
gradient across the entire vdW-m channel material, from the drain to source electrodes,
gradient across the entire vdW-m channel material, from the drain to source electrodes, developing a photothermoelectric potential (V_{PTE}) . b) I_d - V_d characteristics of a photo
gradient across the entire vdW-m channel material, from the drain to source electrodes, developing a photothermoelectric potential (V _{PTE}). b) I _d -V _d characteristics of a photothermoelectric type photodetector. (c) Typical vdW-m based PB photodetector. Uniform light
gradient across the entire vdW-m channel material, from the drain to source electrodes, developing a photothermoelectric potential (V_{PTE}). b) I_d - V_d characteristics of a photothermoelectric type photodetector. (c) Typical vdW-m based PB photodetector. Uniform light illumination results in a temperature-induced resistance change (ΔR) of the channel material.
gradient across the entire vdW-m channel material, from the drain to source electrodes, developing a photothermoelectric potential (V_{PTE}). b) I_d - V_d characteristics of a photothermoelectric type photodetector. (c) Typical vdW-m based PB photodetector. Uniform light illumination results in a temperature-induced resistance change (ΔR) of the channel material. (d) Typical I_d - V_d characteristics of a PB-type detector.[19]
gradient across the entire vdW-m channel material, from the drain to source electrodes, developing a photothermoelectric potential (V_{PTE}). b) I_d - V_d characteristics of a photothermoelectric type photodetector. (c) Typical vdW-m based PB photodetector. Uniform light illumination results in a temperature-induced resistance change (ΔR) of the channel material. (d) Typical I_d - V_d characteristics of a PB-type detector.[19]
gradient across the entire vdW-m channel material, from the drain to source electrodes, developing a photothermoelectric potential (V_{PTE}). b) I_d - V_d characteristics of a photothermoelectric type photodetector. (c) Typical vdW-m based PB photodetector. Uniform light illumination results in a temperature-induced resistance change (ΔR) of the channel material. (d) Typical I_d - V_d characteristics of a PB-type detector.[19]

interface with hybridization (for example, Ti-MoS₂ contact, where MoS₂ under the contact is metallized by Ti). E_F, E_C and E_V represent the Fermi level of the metal, and the conduction and valence bands of the 2DSC, respectively. T_B and S_B indicate the tunnel and Schottky barrier heights, respectively. A, B, B' and C represent different regions in the current path from the metal to the SC. The blue arrows in b, d and f represent the different injection mechanisms. From top to bottom: thermionic emission, thermionic field emission and field emission (tunnelling). In d, only thermionic emission is available [39]......20 Figure 9. Metal Induced Gap States in a metal-semiconductor interface. [38]21 Figure 10. Inserting ultra-thin tunnel barrier for weakening FLP......23 Figure 11. DFT Calculated band alignment between 2D metals and semiconductors and real 3D metals work functions. Columns on left show the electron affinity and ionization potential of semiconductors. Right column shows work function of 3D metals. The phase is labeled in Figure 12. vdW metal-2DSC interface via 2 step decomposable buffer layer strategy.......27 Figure 13. Using patterned graphene as a diffusion barrier for deposited contacts......29 Figure 14. (a) A type-II (Staggered) heterointerface band alignment (b) A type-III (Broken Gap) Figure 15. Localized field modulation induced dark current repression (a) Localized Gate-field Figure 16. Repression of trap state induced dark currents utilizing (a) graphene as interfacial Figure 18. (a) Schematic Illustration of all van der Waals heterojunction photodetector (Purple and red spheres represent gallium and tungsten metal atoms, while blue and yellow spheres

represent sulfur and selenium atoms respectively). (b) Optical micrograph image of the device.
45
Figure 19. (a) Raman spectroscopy of few layer GaS showing characteristics A ¹ _{1g} , E ¹ _{2g} and
A^2_{1g} modes, ultrathin WSe $_2$ showing characteristics E^1_{2g} and A_{1g} modes and the heterojunction
region showing all the characteristics peaks. Raman mapping of (b) A_{1g} mode (256.94cm ⁻¹) of
WSe_2 (top) and (c) A^2_{1g} (359.58 cm ⁻¹) of GaS, showing evident uniform Raman quenching in
the overlapped regions for both the modes. (d) Photoluminescence spectroscopy of ultrathin
WSe ₂ in the bare and overlapped regions of the heterojunction, with the (e) showing the PL
mapping. Evident PL quenching is observed from both the spectroscopy and mapping results.
46
Figure 20. Inference of heterojunction band structure from UPS (a) Secondary Electron cut-off
for GaS, with the inset showing the position of valence band edge. (b) Secondary Electron cut-
off for WSe ₂ , with the inset showing the position of valence band edge. (c) KPFM image of the
heterojunction region with corresponding SPD profile, showing a SPD of ~200 mV. (d) The
proposed band alignment before contact, with various energies
Figure 21. (a) AFM image of the heterojunction region with corresponding height profiles
showing a thickness of (b) GaS and (c) WSe2 layer of 8.5nm (region A) and 3nm (region B),
respectively
Figure 22. Cross-sectional HR-STEM image of the all vdW region of the heterojunction,
showing (from bottom) h-BN, WSe2, GaS and vdW contact, with pristine interfaces between
constituent junctions
Figure 23. HAADF STEM image of the cross section of the heterojunction and EDX mapping
of the elements in the heterojunction region showing presence of Ga, S, W, Se, B and N
concentrations at respective vdW material layers 51

Figure 24.(a) Dark I _d -V _d profile of the photodiode, showing two distinct linear regions with
ideality factor η_1 and η_2 of 1.6 and 2.96 respectively. (b) $ln(I_d/V_d^2)$ vs $1/V_d$ plot of the diode
forward current regime, showing 3 distinct operation regions (DT, FN and SPLC). (c) Double
log I _d -V _d plot of the forward current. (d) Schematic illustration of transport characteristics of
the photodiode under forward and reverse bias conditions
Figure 25. Pseudo band alignment of the heterojunction under quasi-equilibrium state of
illumination, illustrating intralayer transitions (T ₁ and T ₂) and interlayer transition (T ₃)54
Figure 26. Evolution of layer dependent transition in contact type for GaS-vdW Ag on h-BN.
(a) ohmic-14nm (b) ohmic- 8nm (c) schottky-5nm. (d) Estimation of shift in Schottky barrier
with decreasing thickness, due to shifts in fermi-level and conduction band edges55
Figure 27. Modulation of WSe ₂ fermi-level, with thickness. (a) Optical micrograph of a step
height varying WSe ₂ flake of 15nm. Corresponding (b) AFM image used for height profile. &
(c) KPFM image for surface potential difference. (d) Height profile and surface potential
difference variation in the flake. (e) Strategy for optimization of WSe2 layers for efficient
charge generation, separation and extraction
Figure 28. Carrier extraction pathway for GaS layers with thickness (a) t ₁ (device-1) and (f) t ₂
(device-2), where $t_2 > t_1$
Figure 29. (a) Metalized 2DLM and Fermi level pinning (FLP). (b) Van der Waals contact, free
of FLP, metallized 2DLM and efficient contact engineering
Figure 30. (a) Schematic of a semi-vertical GaS-WSe ₂ heterojunction. (b) Schematic of a lateral
extended channel GaS-WSe2 heterojunction. (c) Transport path of photo carrier in a semi-
vertical heterojunction (d)Transport path of photo carrier a lateral extended channel GaS-WSe ₂
heterojunction62
Figure 31. Optoelectronic characteristics of the device under 450nm illumination. (a) Evolution
of log I _d -V _d characteristics under increased illumination power. (b) Zoomed region of I _d -V _d

showing clear I_{SC} and V_{OC} . (c) I_{SC} and V_{OC} vs power density plot showing a linear region for
I_{SC} and no saturation with a LDR of 106.7 dB and V_{OC} saturation at 0.36 V. (d) Electrical power
characteristics of the photodiode under increased illumination showing various PCE under
varied illumination conditions
Figure 32. (a) Responsivity and detectivity vs power density of the device at 450nm
illumination, showing a peak photovoltaic responsivity of 376.76 mA/W and detectivity of
4.12×10 ¹¹ Jones. (b) EQE at various wavelengths and power densities (c) Fill factor of the
device under visible solar spectrum region with varying power density67
Figure 33. (a) Dark current trace of the synergistic-engineered photodiode at V _{ds} =0 V. (b) Noise
Power Density plot of the device
Figure 34. Temporal photocurrent response of the device at 405 nm illumination, showing (a)
200 cycles of switching stability with no degradation, (b) evolution of stability of the device
under a course of 90 days observation period, (c) rise and fall time of the device showing 545
μs (rise) and 471 μs (fall) edges and (d) frequency response showing a cutoff (-3dB) at 697Hz.
70
Figure 35. (a) Photovoltaic temporal response of the device under maximum available
illumination conditions of the device under various wavelengths. The device shows a
photovoltaic response between 275nm and 1064nm, with peak on-of ratio of 10 ⁵ . (b)
responsivity and detectivity of the device at various investigated wavelengths. (c) I _{SC} -PD _{in} for
various wavelengths of investigation. (d) evolution of power law exponent (α), at various
wavelengths72
Figure 36. (a) Optical micrograph image (b) AFM image and height profile (c) KPFM image
and height profile (d) I _d -V _d characteristics (e) double log plot of I _{SC} vs PD _{in} and (f)
Optoelectronic power conversion characteristics of device-2 (All optoelectronic features were
obtained at 405nm illumination wavelength) 74

Figure 37. (a) Optical micrograph image (b) AFM image and height profile (c) KPFM image
and height profile (d) I _d -V _d characteristics (e) double log plot of I _{SC} vs PD _{in} and (f)
Optoelectronic power conversion characteristics of device-3. (All optoelectronic features were
obtained at 405nm illumination wavelength)
Figure 38. (a) Optical micrograph image (b) AFM image and height profile (c) KPFM image
and height profile (d) I _d -V _d characteristics (e) double log plot of I _{SC} vs PD _{in} and (f)
Optoelectronic power conversion characteristics of device-4
Figure 39. (a) Dark current trace of at V _{ds} =0 V. and (b) Noise Power Density plot of the device-
3. (c) Dark current trace of at V_{ds} =0 V. and (d) Noise Power Density plot of the device-477
Figure 40. (a) Evolution of PCE of the fabricated a-vdW devices, suggesting the need for
synergistic thickness engineering for efficient light harvesting characteristics, with a maximum
PCE for synergistically optimized dev-1 and minimum for dev-2 having a thicker GaS and
WSe ₂ regions, with intermediate performance from dev-3, constructed from ultra-thin WSe ₂ ,
similar to dev-1 and slightly thicker GaS than dev-1. (b)Comparison of responsivity and
detectivity for the fabricated devices under similar illumination conditions. (c) Comparison of
rise/fall time and power exponent of all the fabricated devices
Figure 41. (a) Gate-tunable dark current characteristics at various V _{ds} , showing strong
ambipolar response. (b) Gate tunable photoresponse of the device under various illumination
intensities. (c) Evolution of V_{OC} and I_{SC} under gate tunable conditions, for optoelectronic logic
applications79
Figure 42. (a) Schematic illustration of a single-pixel imaging system. Reconstructed image of
the pattern "P O L Y U" (b) using 405nm illumination and (c) using 810nm illumination80
Figure 43. a) Variation of V_{OC} , with tuned V_{g} , under illumination at 405nm. A state of High
(V_{OC} >0.35 V) and Low (V_{OC} <0.15 V) could be outlined in the sky blue and pink region,
respectively. (b) Schematic Illustration of the Optoelectronic logic AND gate (top) and its'

corresponding state table (bottom). (c) State trace and corresponding logic function
demonstration of the optoelectronic AND operation
Figure 44. (a) Schematic Illustration of the self-powered Gr-GaS-Au a-vdW Photodetector. (b)
Microscope image of the fabricated device. (c) Raman spectrum of multilayered GaS depicting
the in plane and out of plane vibration modes. (d) Atomic Force Microscopy image of Gr-GaS
heterojunction and (e) & (f) height profiles of few layer Gallium Sulfide (~14nm) and few
layers of graphene contact (~10nm), respectively
Figure 45. (a) I_d - V_d characteristics of the device under dark conditions. (b) I_d - V_d characteristics
of the device under illumination conditions. (c) log I _d -V _d characteristics of the device under
variant power densities at 406nm illumination. (d) I_{SC} vs power density with α value of 0.86,
suggesting trapping and recombination in the semiconductor. (e) Temporal response of the
device under 375nm illumination, showing pyro-electric features
Figure 46. Recorded spiking photo-current effect in Gr-GaS-Au a-vdW device under 375nm,
405nm and 450nm illumination90
Figure 47. (a) Temporal response of the device under 375nm illumination. (b) Rise time of the
device (b) Fall time of the device91
Figure 48. (a) Dark current trace of Gr-GaS-Au photodiode (b) Corresponding Noise Power
Density plot92
Figure 49. (a) Schematic illustration of the Gr-GaS-WSe ₂ a-vdW heterojunction photodetector.
(b) Optical micrograph image of the device
Figure 50. (a) Raman characteristics of bare FL-Gr, bare GaS and bare WSe2 and the constituent
heterojunction region, showing all the characteristics Raman peaks, highlighting a robust
heterojunction. (b) Raman mapping of (i) FL-Gr G band (1580cm ⁻¹) (ii) GaS A ² _{1g} band
(361.5cm ⁻¹) and (iii) WSe ₂ A1g band (256.5cm ⁻¹). Intense "Raman quenching" is evident for
all the bands mentioned, in the Gr-GaS-WSe ₂ region suggesting robust coupling

Figure 51. (a) AFM image of the heterojunction device. Height profile of (a) WSe ₂ , (b) GaS
and (c) FL-Gr, showing their corresponding thickness
Figure 52. (a) I _d -V _d characteristics of the diode under dark conditions (b) I _d -V _d characteristics
of the device under illumination conditions99
Figure 2. Exciton dissociation and charge transfer in the Gr-GaS-WSe ₂ heterojunction 100
Figure 54. (a) I_d - V_d characteristics of the device showing I_{SC} and V_{OC} cross-overs at respective
axis. (b) Input light Power density vs V _{OC} and I _{SC} of the device101
Figure 55. (a) PCE of the Gr-GaS-WSe ₂ devices. (b) Responsivity and detectivity of the device.
(c) Fill factor and EQE of the device
Figure 56. (a) I _d -V _d plot (b) Double log plot of I _{SC} vs PD _{in} showing power exponent (α) (c)
Optoelectronic power conversion characteristics and (d) Responsivity and Detectivity of
device-1 at 405nm illumination
Figure 57.(a) I _d -V _d plot (b) Double log plot of I _{SC} vs PD _{in} showing power exponent (α) (c)
Optoelectronic power conversion characteristics and (d) Responsivity and Detectivity of
device-1 at 532nm illumination
Figure 58. (a) I _d -V _d plot (b) Double log plot of I _{SC} vs PD _{in} showing power exponent (α) (c)
Optoelectronic power conversion characteristics and (d) Responsivity and Detectivity of
device-1 at 660nm illumination
Figure 59. (a) Temporal response of the device under varied illumination intensity (b) double
\logI_{SC} vs PD_{in} (c) Responsivity and Detectivity vs \logPD_{in} at 325nm. (d) Temporal response
of the device under varied illumination intensity (e) double log I_{SC} vs PD_{in} (f) Responsivity and
Detectivity vs log PD _{in} at 375nm. (g) Temporal response of the device under varied illumination
intensity (h) double log I_{SC} vs PD_{in} (i) Responsivity and Detectivity vs log PD_{in} at 810nm.
(Device-1)

Figure 60. (a) double $\log I_{SC}$ vs PD_{in} at 940nm illumination (b) double $\log I_{SC}$ vs PD_{in}	at 275nm
illumination (Device-1)	110
Figure 61. Noise measurement of Instrument at Open circuit. (a) Dark current tra	ace for 5
seconds (b) Corresponding PSD of the instrument at open circuit.	110

List of Tables:

Table 1. Commonly used figure of merits (FoMs) for characterizing vdW-m based
photodetectors[19]
Table 2. Comparison of device performance parameters of all the fabricated devices under self-
bias conditions at 405 nm wavelength:
Table 3. Multivariate performance comparison of some of the recently reported heterojunction-
based photodetectors with our optimized device.
Table 4. Comparison of reported solar cell figure of merits with synergistically engineered
photodiode85



Chapter 1: Introduction:

1.1. Background and Motivation:

Low-dimensional van der Waals materials (vdW-m) with intrinsically passivated basal planes have been at the forefront of investigation over the last two decades, due to their perceived future dominance in the post-Moore era of optoelectronics. With the ease of access to fabrication of atomically thin vdW heterojunctions having clean interfaces for prototypical demonstration, a substantial amount of research has been ongoing to establish their potential in multifunctional optoelectronics. Their advantageous properties, such as layer-dependent bandgaps, strong absorption in the ultrathin regime, and high in-plane carrier mobility, have made them essential research targets.

Despite the intrinsic passivation of their basal planes, vdW material-based photodiodes, even with optimized approaches, typically exhibit a power exponent α of approximately 0.9. This indicates the presence of recombination and trapping processes; however, the underlying causes have yet to be fully elucidated. The ideal value of α =1 has thus far remained an unrealistic target, with any value approaching 1 considered satisfactory. To achieve a value closer to 1, a well-optimized strategy must be developed, alongside a renewed focus on understanding the bottlenecks that influence α . While many assume that defects within the semiconductor are the primary sources of recombination and trapping, there has been comparatively little attention given to the role of contact regions.

In the context of transistor applications involving vdW materials and their heterojunctions, where charge injection is critical, the contact regions have been identified as significant bottlenecks due to issues such as FLP, large Schottky barriers, and elevated contact resistance. This raises the question of the role that FLP plays in the performance of vdW photodiodes, particularly when metal-induced gap states arise as a consequence of FLP. If an ideally



optimized vdW photodiode is achieved without recombination or trapping occurring in the semiconductor, can we attain α =1? Moreover, if contact induced degradations could be avoided, with ideally pristine interfaces, could we identify novel physical phenomena, that were otherwise so far inaccessible?

Therefore, a multifactorial investigation strategy is essential to understand the interplay of factors associated with photocarrier generation, recombination, separation, transport, and extraction, especially for large bandgap vdW materials like GaS and their heterojunctions, when contact induced degradation is suppressed, paving the way for robust devices, that could be utilized for suppressing dark currents for ultra-low light detection and simultaneously used for broadband photodetection with fast response speeds.

1.2. Rationale:

In vdW material-based devices and heterojunctions, particularly field-effect transistors (FETs), the primary challenge to enhancing device performance has been identified as the large contact resistance caused by Fermi Level Pinning (FLP), which induces a Schottky barrier that limits current injection. However, for photodetectors, the study of contact-induced degradation and FLP remains largely unexplored. FLP directly affects key figures of merit (FoMs), yet no systematic investigations have been conducted to date. The impact of FLP is expected to be more pronounced in moderately wide-bandgap vdW semiconductors and their heterojunctions. Addressing FLP can significantly improve several key FoMs, thereby enhancing overall device performance. A universally applicable method that can be applied to mitigate FLP in vdW heterojunction is to adopt a meticulous strategy of contact integration, that can essentially keep a pristine interface between vdW-m and the integrated contacts. Further enhancements of the device can be achieved through careful structure and thickness optimization of the constituent materials.



Hence, to investigate effects of FLP, a moderately wide-bandgap n-type semiconductor with closely matching band alignment characteristics for vdW metal contact integration was essential. GaS emerged as the ideal choice, although GaS-based photodiodes have not been reported to date. To complete the heterojunction, WSe₂ was selected as the p-type semiconductor, demonstrating a fermi level difference of approximately 200 meV at the appropriate GaS-WSe₂ thickness. This heterojunction features a large valence band offset that restricts minority carrier injection, resulting in ultra-low dark currents. Additionally, WSe₂ exhibits a strong thickness-dependent change in fermi level, making the GaS-WSe₂ heterojunction a suitable candidate for investigating FLP effects and optimizing them alongside thickness-dependent p-n junction adjustments.

1.3. Accomplishments presented in this thesis:

The accomplishments of this thesis can be summarized as follows:

- Successfully fabricated of All van der Waals Photodiodes: GaS-WSe2 and Gr-GaS-Au.
- Achieved type-II band alignment in the GaS-WSe₂ heterointerface, resulting in ultralow dark currents.
- Demonstrated a method to optimize heterojunction thickness (for both GaS and WSe₂) based on the number of layers to create a robust p-n junction.
- Fabricated van der Waals metal contacts on a sacrificial substrate to demonstrate FLP resilient All Van der Waals Devices
- Fabrication and demonstration of several a-vdW GaS-WSe₂ devices with repeatable enhanced characteristics through the integration of contact metals via the vdW technique.



- Comparison of a-vdW devices with traditionally lithography-patterned metal-deposited devices based on multiple figures of merit, confirming superior performance of the avdW technique.
- Demonstration of Multifunctional applications: Implemented the GaS-WSe₂
 photodiode in imaging applications and as a gate-tunable optoelectronic logic AND gate.
- Spiking Photocurrent Photodiode: Demonstrated a Gr-GaS-Au photodiode for ultralow light detection, featuring a novel dual spiking polarity characteristic.

1.4. Thesis outline

The thesis outline could be elaborated as follows:

Chapter 2 provides a comprehensive overview of two-dimensional layered materials (2DLMs), emphasizing key material features that influence their application in optoelectronics, including crystal structure, absorption characteristics, bandgap relationships, and carrier mobility. Subsequently, the chapter introduces the figures of merit for photodetectors, along with a broad classification of 2DLM-based photodetectors and an explanation of their working principles. Following this, a brief literature review contextualizes the topics explored in this thesis, leading to an in-depth discussion on the synergistic optimization of photodetectors and their significance in advancing optoelectronic technologies.

Chapter 3 provides a comprehensive investigation on synergistically engineered all van der Waals GaS-WSe₂ photodiodes with demonstration in multifunctional optoelectronics.

Chapter 4 provides a comprehensive investigation on all van der Waals Gr-GaS-Au photodiodes.



Chapter 5 provides a summary of the investigations presented in this thesis and the ongoing project culminating from this thesis, along with a conclusion to inform how future research should benefit from this thesis.



Chapter 2: van der Waals optoelectronics: Overview and Synergistic Optimization Prospects

2.1. Introduction:

This chapter begins with an overview of two-dimensional layered materials (2DLMs), highlighting key material features that govern their application in optoelectronics, such as crystal structure, absorption characteristics, bandgap relationships, and carrier mobility. Next, we introduce the figures of merit for photodetectors, accompanied by a broad classification of 2DLM-based photodetectors and an explanation of their working principles. Following this, a brief literature review provides context for the topics studied in this thesis, leading into an indepth discussion on the synergistic optimization of photodetectors and their significance in advancing optoelectronic technologies.

2.2. Overview on 2D layered materials:

The advent of mechanically cleaved graphene from graphite has ignited a surge of research into layered low-dimensional materials (2DLMs) [1]. Since then, a diverse array of 2DLMs has been extensively studied, showcasing a wide range of intriguing physical and chemical properties, including semiconducting [2,3], semi-metallic, insulating [4,5], superconducting [6,7], and magnetic [8,9] to name some. Of particular interest is the semiconducting nature of 2DLMs, which can be tuned by varying the number of layers. This tunability positions them as promising candidates for pioneering atomically thin electronics and optoelectronics. Recent advancements in conventional bottom-up synthesis and patterning of large-area vdW 2DLMs [10] have further highlighted their potential as standalone semiconductors, as well as their compatibility with existing silicon technology [11–14].



Among the most widely studied layered semiconductor materials are transition-metal dichalcogenides (TMDCs), characterized by the general formula MX₂, where M represents a transition metal (such as Mo or W) and X denotes a chalcogen (such as S, Se, or Te). Each layer of MX₂ consists of three atomic planes: the transition metal atomic plane (M) is positioned at the center of the crystal structure, flanked by chalcogen atomic planes on the top and bottom. The bonds between the transition metal and chalcogen atoms are covalent, while the layers are held together in the c-axis direction by weak vdW forces. Most semiconducting TMDCs exist in the most thermodynamically stable 2H phase, where each layer exhibits a trigonal prismatic coordination of M atoms by X atoms, with the layers stacked in an ABAB pattern. Air-stable semiconducting TMDCs from group 6 of the periodic table—such as MoS₂, WSe₂, MoSe₂, and WS₂—have been extensively explored [15]. Notably, a single sheet of MoS₂ has been predicted to absorb 5–10% of incident light in the visible spectrum [16,17].

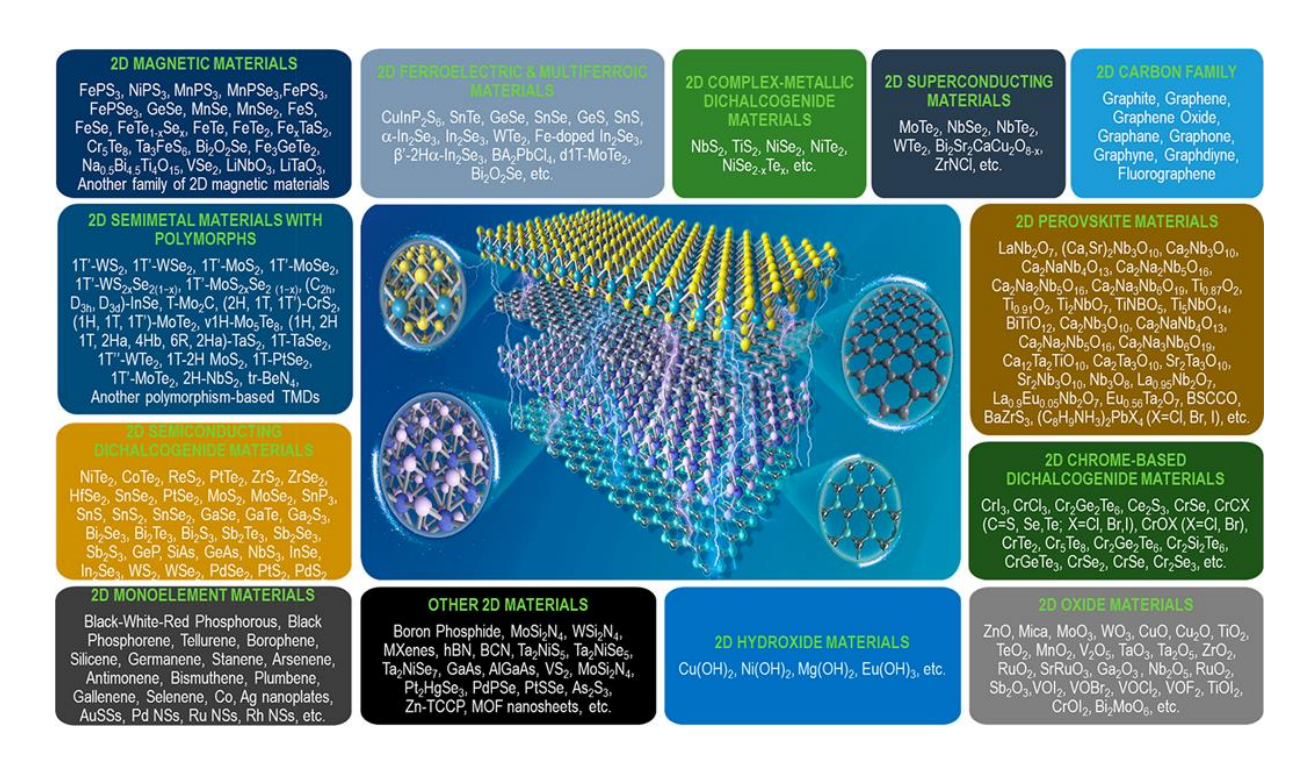


Figure 1. 2DLM Family and their corresponding characteristic classification [18].

Additionally, another widely studied family of layered 2DLMs is the III-VI layered semiconductors, characterized by the general formula NY, where N represents a group-III metal



(such as Ga or In) and Y denotes a chalcogen (S, Se, Te). Each layer of NY consists of four atomic planes, with two N atomic planes at the center of the crystal structure sandwiched between two Y atomic planes at the top and bottom. These atomic planes are held together by strong covalent bonds in the Y-N-N-Y configuration. Depending on the specific type of III-VI 2DLM, various semiconducting phases can exist in multiple polytypes (α , β , or γ), featuring hexagonal layered structures. Notable air-stable semiconducting III-VI 2DLMs include InSe, GaS, GaSe, and GaTe, which have been extensively explored for their promising electronic and optoelectronic properties. Apart from the two families of 2DLM mentioned a vast library of 2DLM is currently being investigated and an overview of the representative larger 2DLM family is presented in figure 1.

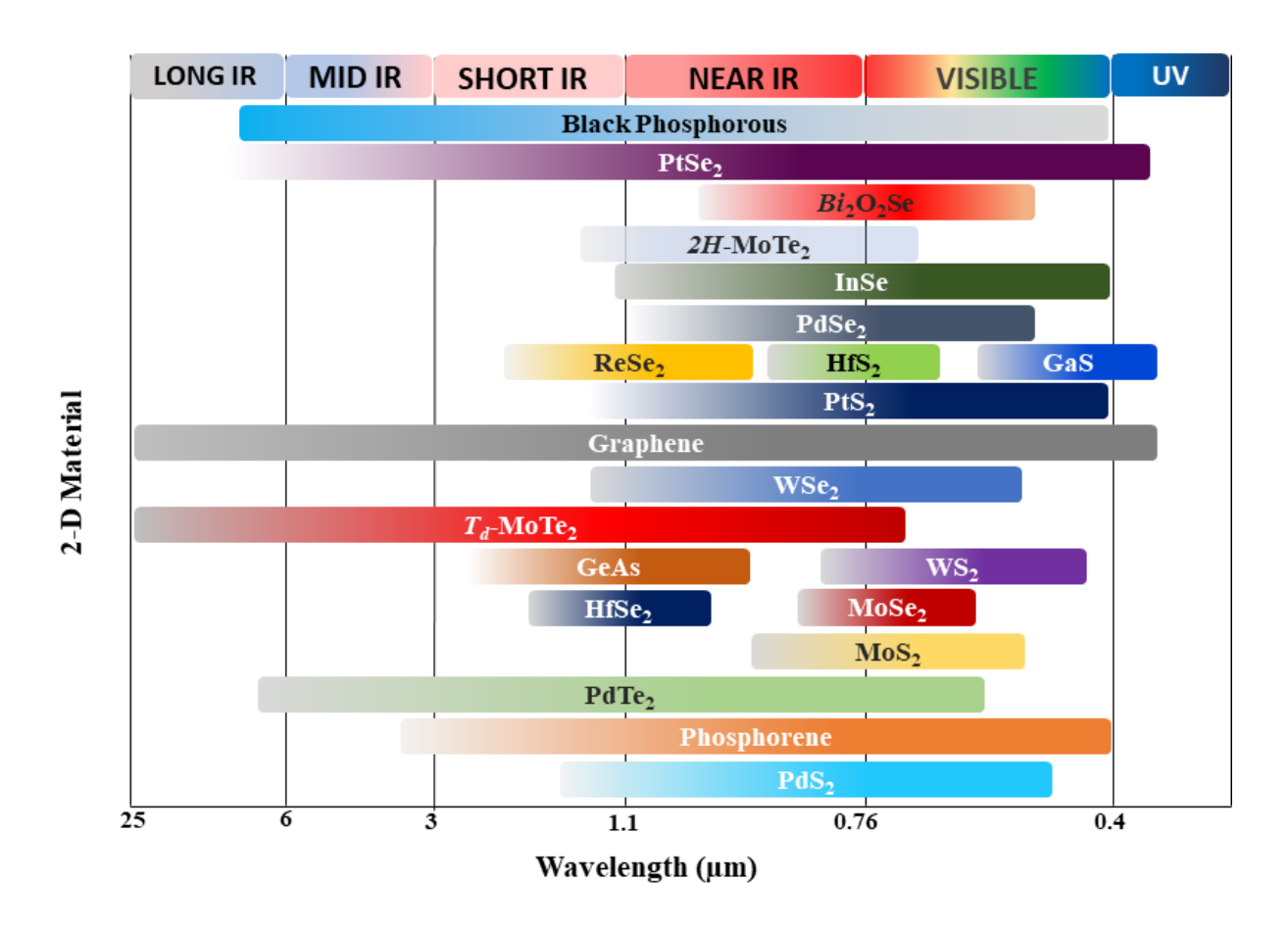


Figure 2. Spectral Response of some 2-D materials used in photodetection [19].



These materials exhibit fascinating layer-dependent behavior, wherein the bandgap increases and transitions from indirect to direct as the number of layers approaches the monolayer limit [20], in the case of TMDC, while for the case of III-VI 2DLM InSe and GaS shows direct and indirect bandgaps, despite reduction in thickness. This layer dependent transition in bandgap is particularly significant for optoelectronics, as the bandgap of the absorber layer directly influences the spectral sensitivity of the optoelectronic device. As illustrated in figure 2, the extensive library of 2DLMs offers a wide range of spectral response possibilities, simply by selecting the appropriate absorber layer material.

For applications in optoelectronics, key features of two-dimensional layered materials (2DLMs) should include substantial absorption, high carrier mobility, and reduced trapping within the semiconductor. Achieving a balance among these characteristics at the atomically thin scale is essential for optimal device performance. Moreover, the combination of different 2DLMs to create heterojunctions can significantly enhance the optoelectronic performance of devices. This mixing and matching introduces new band alignments, which can help suppress dark currents and improve photoelectric conversion efficiency. Such heterojunctions leverage the unique properties of each material, allowing for tailored device functionalities that are crucial for advancing optoelectronic technologies.

2.3. Figure of merits (FoM) for photodetectors:

Photodetector performance is typically assessed using several key figures of merit (FoMs). These standardized FoMs enable both evaluation and comparison between different photodetectors, as well as an assessment of their suitability for specific applications. Table 1 presents the most commonly used FoMs for vdW-m photodetectors, which are particularly relevant for evaluating photosensors. The table includes a brief description of each FoM, its mathematical expression, and the appropriate reporting units.



Table 1. Commonly used figure of merits (FoMs) for characterizing vdW-m based photodetectors[19]

FoM Parameter	Definition	Expression	Unit
Responsivity	Ratio of Photocurrent (I_{photo}) to the incident light power (P_{in}).	$R = \frac{I_{photo}}{P_{in}} = \frac{I_{light} - I_{dark}}{P_{in}}$	A/W
External Quantum Efficiency	Ratio of number of photogenerated electrons per unit time to the number of incident photons. Also referred to as the product of charge transfer efficiency and light absorption efficiency. [h is the Planck constant, e is the electronic charge, c is the light speed, and λ is the incident wavelength of light source]	$EQE = \frac{N_I}{N_P} = \frac{h \cdot c \cdot I_{photo}}{e \cdot \lambda \cdot P_{in}}$	-
Dark Current	Current persistent in the photodetector under dark/no light conditions.	I_{dark}	A
Gain	Ratio of number of photogenerated e-h pairs collected by the contacts to the number of photoexcited e-h pairs. [μ is the carrier mobility, V_{bias} is the applied bias, L is the channel length, τ_{life} is the carrier lifetime, and $\tau_{transit}$ is the carrier transit time.]	$G = \frac{\tau_{life}}{\tau_{transit}} = \frac{\mu \cdot \tau_{life}}{L^2} V_{bias}$ $\left[\tau_{transit} = \frac{L^2}{\mu \cdot V_{bias}}\right]$	-
Linear Dynamic Range	It is the range of illumination log power density for which the log range of photocurrent shows linearity, before reaching saturation.	$LDR = 20log \frac{P_{sat}}{P_{low}}$	dB
Response time	The rise (decay) time is defined as the time for the photocurrent to reach 10–90% (90–10%), after introduction (removal) of incident photon flux.	$ au_{rise}(au_{decay})$	S
3dB bandwidth @ Relative balance	The cut-off frequency f_{3dB} , of modulated incident light when the responsivity of the photodetector decreases by $3dB$ (0.707 of the stable value). At a much lower frequency, the responsivity is independent of the light modulation frequency. [I_{max} and I_{min} are the maximum and minimum photocurrent]	$f_{3dB}@\frac{I_{max}-I_{min}}{I_{max}}\%$	Hz
Noise Current	Unwanted current persistent in the device due to internal physical mechanisms	i_N	$AHz^{-1/2}$
Noise Equivalent Power	The minimum light power that is detectable by a detector is defined as the light power when the signal-to-noise ratio (SNR) is $1. [A \text{ is the effective device area.}]$	$NEP = \frac{i_N}{R} = \frac{\sqrt{A}}{D^*}$	$ m WHz^{-1/2}$
Measured Specific Detectivity	It is a measure of a detector's ability to resolve the weakest of the incident light signal	$D^* = \frac{\sqrt{A}}{NEP} = \frac{\sqrt{A}}{i_N}R$	cmHz ^{1/2} W ⁻¹ (Jones)
Calculated Specific Detectivity	Specific detectivity is calculated, assuming that the major contribution of noise is from dark current shot noise.	$D^* = \sqrt{\frac{A}{2 \cdot q \cdot I_{dark}}} R$	cmHz ^{1/2} W ⁻¹ (Jones)

2.4. Broad Classification of vdW-m based Photodetectors

vdW-m based photodetectors can be broadly classified into four main types based on the literature: photovoltaic, photoconductive, photothermoelectric, and photobolometric, as illustrated in Figure 3. The specific photodetection mechanism in a vdW material-based detector may operate as a standalone phenomenon or as a combination of these effects. This variation depends on several factors, including the internal potential developed or externally



applied potential, the internal light-matter interaction mechanisms within the two-dimensional layered material, and the distribution of the input light flux density.

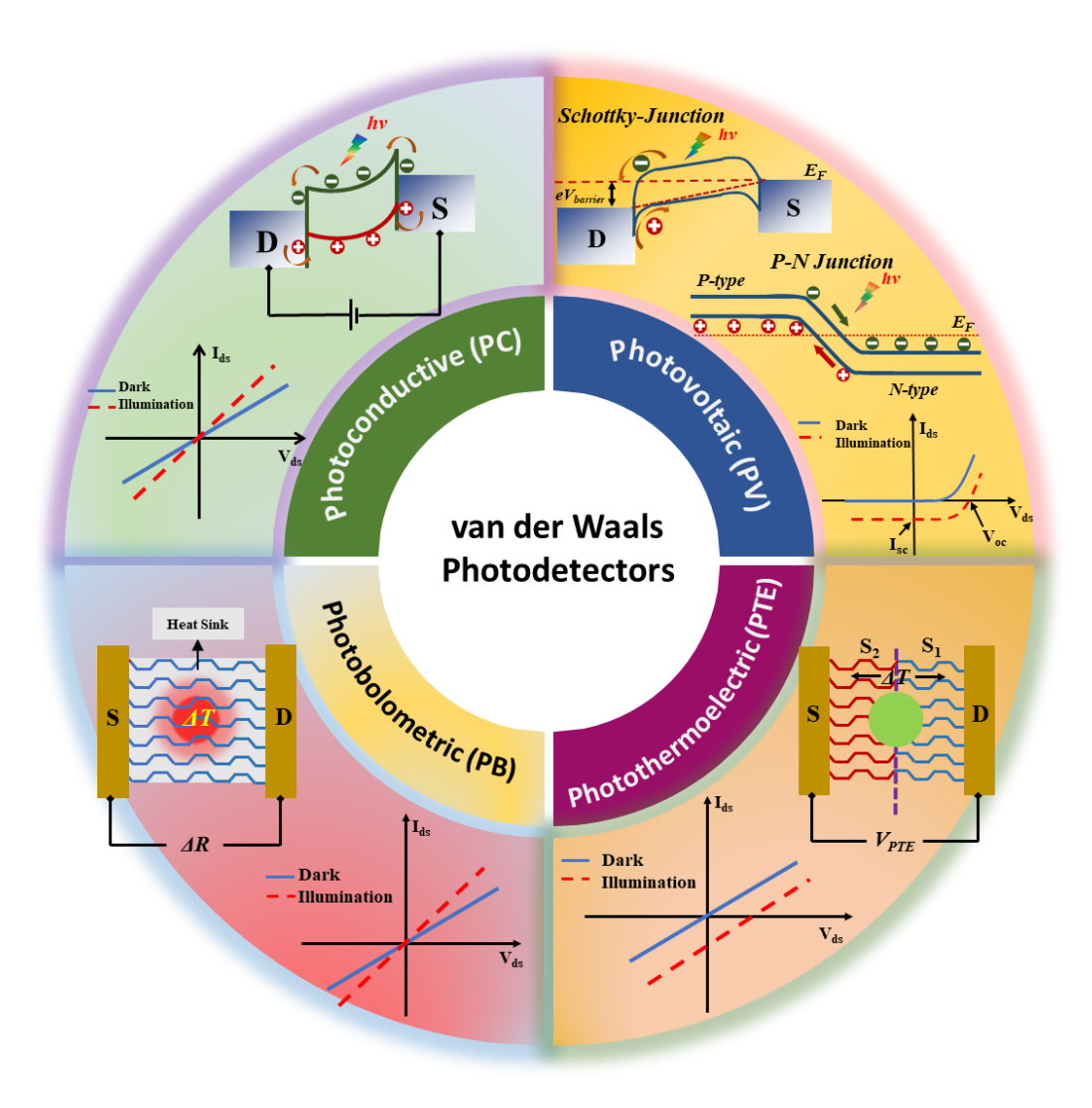


Figure 3. Broad classification of vdW-m photodetectors and their outlying internal mechanisms.

2.4.1. Photovoltaic Type Photodetectors

In a photovoltaic-type photodetector, the built-in electric field that facilitates the photovoltaic effect (PVE) originates from either a p-n junction [21] or a Schottky junction [22] at the semiconductor-metal interface. This internal electric field is critical for separating the photogenerated electron-hole (e-h) pairs, thereby enhancing the efficiency of the photodetection process.



Strategies for developing the necessary built-in electric field in two-dimensional vdW-m based detectors include the following:

- Creating vertical or lateral heterojunctions [23,24]
- Chemical doping [25,26]
- Carefully selecting metals with different work functions [27,28].

When the vdW-m active channel is illuminated with photons that exceed the bandgap energy, the absorbed photons excite electron-hole (e-h) pairs, which are subsequently separated by the internal electric field resulting from band bending at the p-n or Schottky junction (see figure 4 a,b). This separation generates a short-circuit current (I_{SC}) in the device (see figure 4c). The direction of the photocurrent is determined by the built-in potential. If the circuit is left open, the separated e-h pairs instead create an open-circuit voltage (V_{OC}) (see Figure 4c). Photovoltaic photodetectors typically exhibit rectifying current-voltage characteristics and can operate either without any bias or under reverse bias. This capability is very much essential in photodetection as it allows for low dark currents and high quantum efficiencies.

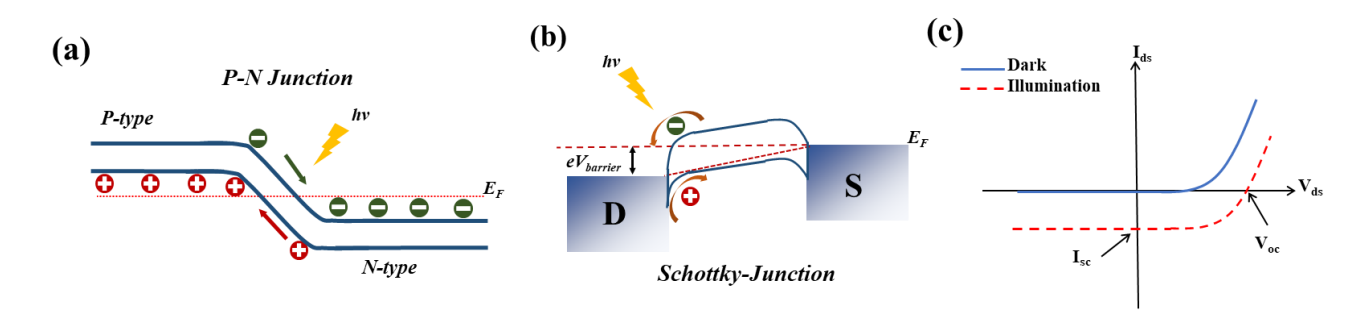


Figure 4. Energy band alignment in a typical (a) p-n junction (b) Schottky junction. (c) Typical I_d - V_d characteristics of a photovoltaic-type photodetector.[19]

2.4.2. Photoconductive and Photo-Gated Photodetectors

Photodetectors that exhibit the photoconductive effect (PCE) show an increase in free charge carriers when illuminated, typically within a semiconductor channel or photoconductor (PC) material. This rise in free carrier concentration leads to a decrease in the channel's resistance.



When a bias voltage (V_{ds}) is applied, these excess charge carriers are swept apart, generating a photocurrent (I_{photo}) (see figure 5a). The photocurrent is defined as the difference between the current under illumination (I_{light}) and the dark current (I_{dark}). When the channel material is illuminated with photons that exceed its bandgap energy, the absorbed photons create electronhole (e-h) pairs. These carriers are then driven by V_{ds} , causing the current to exceed the dark current due to the increased concentration of charge carriers. Unlike photovoltaic-type detectors, photoconductive devices require an applied bias voltage for photocurrent generation. As a result, these detectors do not exhibit an open-circuit voltage (V_{OC}) or short-circuit current (I_{SC}), as illustrated in their typical I_d - V_d characteristics (see Figure 5b).

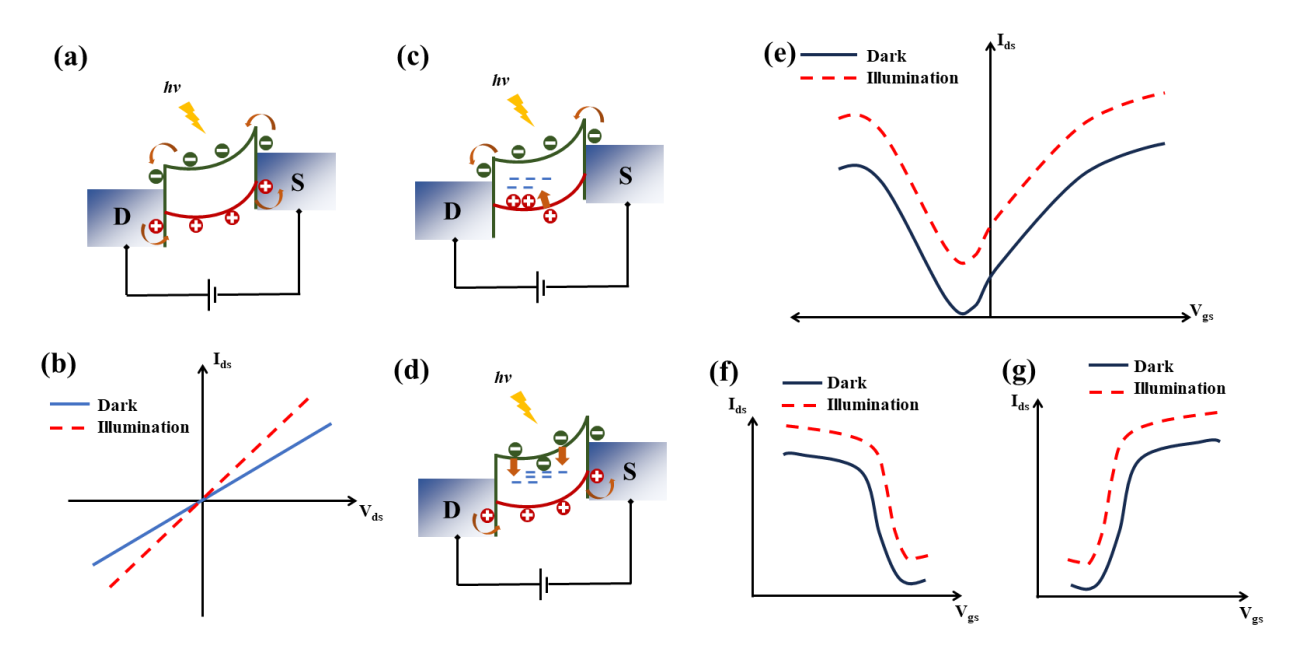


Figure 5.(a) Typical photoconductive effect in a vdW-m based photodetector. The band bending and charge carrier extraction process requires an applied external bias voltage. (b) I_d - V_d characteristics of a typical photoconductive photodetector. Typical photogated photodetector showing (c) n-type characteristics due to p-type charge trapping and (d) p-type characteristics due to n-type charge trapping. I_d - V_g characteristics of a typical (e) ambipolar photoconductive photodetector, (f) n-type carrier dominant photodetector and (g) p-type carrier dominant photodetector.[19]

Photo-gated photodetectors are a specific type of photoconductive device, often likened to phototransistors, that leverage the photogating effect. Under illumination, the typical



generation of electron-hole pairs occurs. However, the application of a gate bias introduces charge-trapping states that function as a localized floating gate, significantly modulating the channel conductance [29,30]. When photogenerated holes are trapped in positively charged hole-trapping sites, the remaining free electrons can move for a longer duration before recombining. This results in high gain and n-type doping characteristics (see figure 5c). Conversely, if electrons are trapped, the device exhibits p-type behavior (see figure 5d). This photogating mechanism enables tuning of the channel conductivity. By carefully designing the device—such as by optimizing the metal work function—photo-gated detectors can display ambipolar transport characteristics (see figure 5e) or be optimized for unipolar operation [31,32] (see figures 5f, g). However, the processes of charge trapping and detrapping can lead to sluggish photoresponse, which is a trade-off for enhanced photoresponsivity and gain [33,34].

2.4.3. Photothermoelectric (PTE) Photodetectors:

Localized light irradiation in a vdW-m can induce a thermal effect known as the photothermoelectric (PTE) effect. This localized illumination generates a temperature gradient (ΔT) across the semiconductor channel, especially when the spot size is smaller than the channel dimensions [27] as illustrated in figure 6a. This temperature differential induces a photothermoelectric potential difference (V_{PTE}) at the ends of the channel, determined by the difference in Seebeck coefficients (S_I and S_2) of the material:

$$V_{PTE} = (S_1 - S_2).\Delta T \tag{1}$$

The units of V_{PTE} are volts per kelvin (V/K). The generation of this photo-induced thermoelectric potential allows PTE-based photodetectors to operate in a self-powered mode, eliminating the need for any external bias voltage, as illustrated in the typical current-voltage characteristics in figure 6b. The electrical conductivity of the channel material is closely associated with the Seebeck coefficients S_I and S_2 through the Mott formula:



$$S = \frac{\pi^2 k_B^2 T_e}{3q} \frac{1}{\sigma} \frac{\partial \sigma}{\partial \varepsilon_F}$$
 (2)

where T_e is the electron temperature, and the derivative of the conductivity σ with respect to energy ε_F must be evaluated at the Fermi energy [35,36]. It is noteworthy that global illumination can also induce the PTE effect in vdW-m, provided there is a strong absorption gradient within the channel to create the necessary temperature differential and form V_{PTE} , typically in the range of a few microvolts to millivolts. The sign of the photogenerated current depends on the difference in Seebeck coefficients of the channel material locations and the polarity of the charge carriers in the channel.

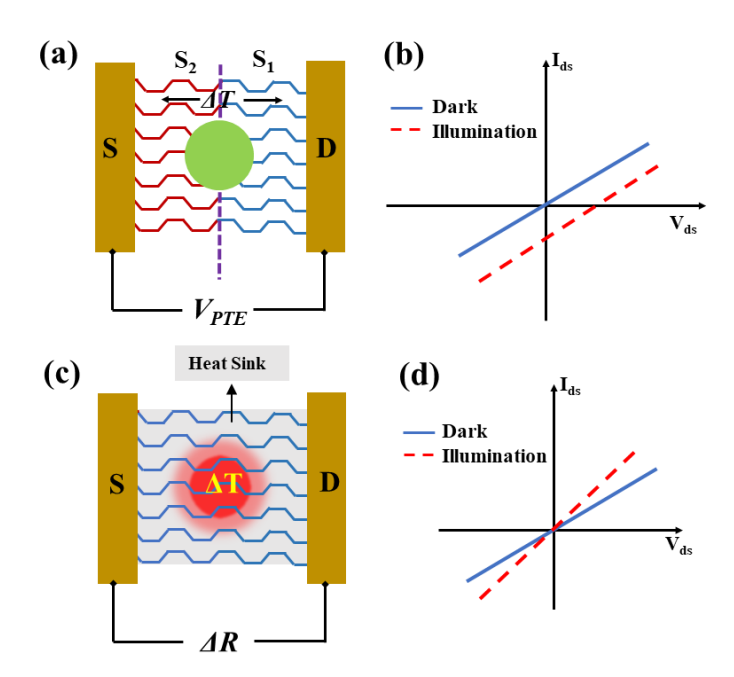


Figure 6. Typical PTE photodetector. Localized light spot (green color) generates a temperature gradient across the entire vdW-m channel material, from the drain to source electrodes, developing a photothermoelectric potential (V_{PTE}). b) I_d - V_d characteristics of a photo thermoelectric type photodetector. (c) Typical vdW-m based PB photodetector. Uniform light illumination results in a temperature-induced resistance change (ΔR) of the channel material. (d) Typical I_d - V_d characteristics of a PB-type detector.[19]



2.4.4. Photobolometric Photodetectors

The Photobolometric Effect (PBE) generates carriers through uniform light-induced heating of a channel material. During the PBE, the heat-sensitive channel material experiences a change in its resistivity due to the increase in temperature as shown in figure 6c. The thermal resistance (R_{tr}) is defined as the rate of change in temperature with respect to the incident power:

$$R_{tr} = \frac{dT}{dP} \qquad (3)$$

Unlike photothermoelectric detectors, bolometric photodetectors are not self-powered and require an external bias voltage. This external bias voltage linearly scales the heat-induced photocurrent generated by the bolometric photodetector, as illustrated in figure 6d. This characteristic enables bolometric detectors to effectively measure changes in temperature due to incident light, providing a useful mechanism for light detection in various applications.

2.5. Synergetic optimized strategies considered in this thesis:

2.5.1. Contact engineering and its influence on optoelectronic device performance:

In this section of the chapter, we explore the norms of contact engineering methods in 2DLM electronics and optoelectronics. A discussion on the associated physical phenomena, a brief background, and a literature review highlighting the progress made in contact engineering for 2DLMs will be provided. Additionally, based on the discussion and findings a pathway toward successful contact integration aimed at optimizing performance in 2DLM-based optoelectronic devices is presented.

To obtain highly efficient electronic and optoelectronic devices, the norm has been to use ohmic type contacts, where the electrical current injection and optical photocarrier extraction



mechanisms face least resistance and unintentional barriers (only specific cases exist where intentional Schottky junctions are created to enhance device performances, for application specific uses). To create high-quality ohmic contacts in bulk three-dimensional (3D) semiconductor-based electronic devices, the most widely adopted method involves heavy doping of the contact region (see figure 8a). This heavy doping reduces the space charge width, facilitating the tunneling of charge carriers into the conduction or valence bands of the semiconductor [37]. This technique enhances the efficiency of charge injection, ensuring better electrical performance and reliability of the device. However, doping atomically thin semiconductors presents significant challenges. The incorporation of heteroatoms into the lattice can distort the native structure of the vdW-m and introduce defects, thereby altering its intrinsic properties [38]. Additionally, the space charge region in 2D semiconductors that are 1 nm thick or less is only weakly dependent on the doping concentration [38]. Consequently, the operating modes of bulk MOSFETs, such as accumulation and depletion modes used to achieve p-type and n-type device operations, cannot be directly applied to electronics based on vdWm. Moreover, due to their atomic thickness, 2D limiting properties at the interface between the metal and 2D semiconductor is critical and any chemical interaction between them should control the charge carrier extraction and injection [39]. The contact resistance quantum limit denoted by Rcmin, is measured using the number of conducting modes in the semiconductor channel that are connected to the 2D charge carrier density (n_{2D}) , results $R_C^{min}=0.026/\sqrt{n_{2D}}=$ $30\Omega\mu m$, when $n_{2D}=10^{13} \text{cm}^{-2}$ [39,40].

When examining the most common type of electronics made from 2D semiconductors i.e. field effect transistors (FETs), it becomes clearer to understand the significance of contact resistance. Low contact resistance in 2D material-based FETs is essential for achieving high on-current, high-frequency operation, and enhanced photoresponse, particularly in the case of photodetectors [39]. However, the large contact resistance created at the interface between the



2D semiconductor and the metal contacts, typically formed through deposition methods such as photolithography or electron beam lithography (EBL), significantly reduces the drain current. The constraint highlights the need for effective strategies to minimize contact resistance to improve the overall performance of 2D semiconductor devices.

There are three elementary interface geometries between 2D materials and bulk metals, which can be broadly categorized as follows:

- 1. **Top Contact Geometry** (see figure 7a): In this configuration, the metal is deposited on top of the 2D material, or a semi-metallic/metallic vdW-m can be laid over on top of the 2D material to define the drain and source regions. To achieve a purely top-contacted geometry, it is essential to avoid contact between the edges of the 2D material and the metal [39].
- 2. **Bottom Contact Geometry** (see figure 7b): For this geometry, the vdW-m must be transferred onto pre-deposited metal contacts on a substrate. To ensure a pure bottom contact, care must be taken to avoid touching the edges of the vdW-m during the transfer process.
- 3. **Edge Contact Geometry** (see figure 7c): In this arrangement, the vdW-m makes contact with the metal along its edges. For a purely edge-contacted configuration, it is important to prevent any contact between the metal and the top surface of the vdW-m during deposition.

Reports exist of edge-contacted devices on graphene (pure edge contact) [41], combinations of graphene and transition metal dichalcogenides (TMDCs) (not completely pure edge contact) [42], and devices incorporating graphene and TMDCs [43]. Each geometry presents unique advantages and challenges in terms of contact resistance and overall device performance.



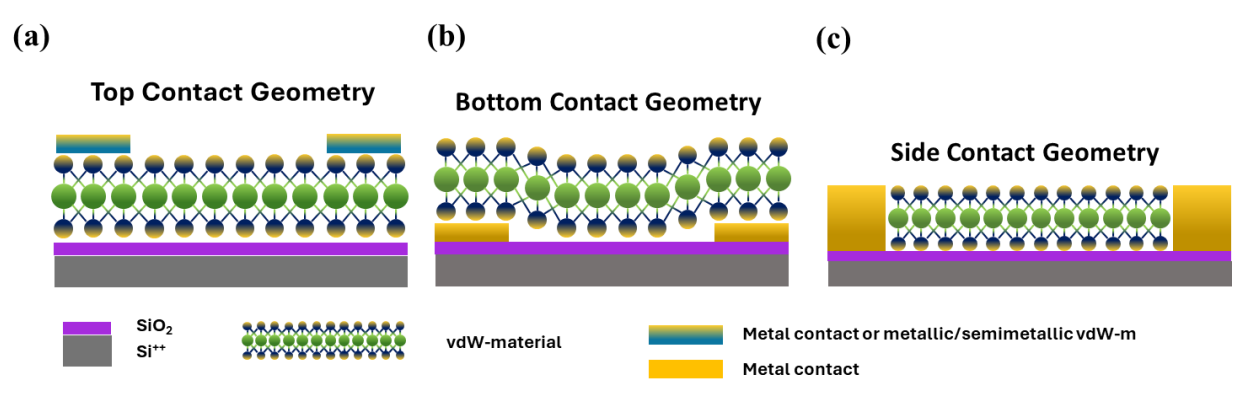


Figure 7. Pure Top Contact Geometry. (b) Pure Bottom Contact Geometry. (c) Pure Side Contact Geometry

Provided that the surface of the 2D material is pristine and defect-free, in a top contact geometry, the metal and the 2D material do not form any covalent bonds. Consequently, the interface between the top-contacted metal and the 2D material is characterized solely by a vdW gap. The same principle applies to bottom contact geometry when a vdW-m is laid over prefabricated metal electrodes. This vdW gap introduces an additional tunneling barrier for charge injection in the case of field effect transistors (FETs) [39], as illustrated in figure 8d, and it also affects the collection of photogenerated charge carriers in photodetectors. This tunneling barrier can influence the overall performance of devices, necessitating careful consideration in the design and fabrication of 2D material-based electronic and optoelectronic systems.

To reduce the tunnel- barrier at the top contact surface, hybridization between the metal and the 2D material can be explored as a method to decrease contact resistance. Density functional theory (DFT) results indicate that certain metals can form covalent bonds with 2D materials, as detailed in [44]. However, it is important to note that strong hybridization between the 2D material and the top contact can distort the properties of the underlying material, potentially negatively impacting the sheet resistance of the 2D material and thereby increasing contact resistance. In some cases, strong hybridization achieved through high-temperature vacuum annealing has been shown to reduce contact resistance. For example, when graphene is



contacted with nickel (Ni) or cobalt (Co), where the carbon atoms can dissolve into the contact metal and form strong covalent bonds, contributing to much smaller contact resistance [45], owing to removal of resist residues and near perfect interfaces. This ability of stronger interactions with the metal may enhance charge injection and improve overall device performance, which was evidence in some cases.

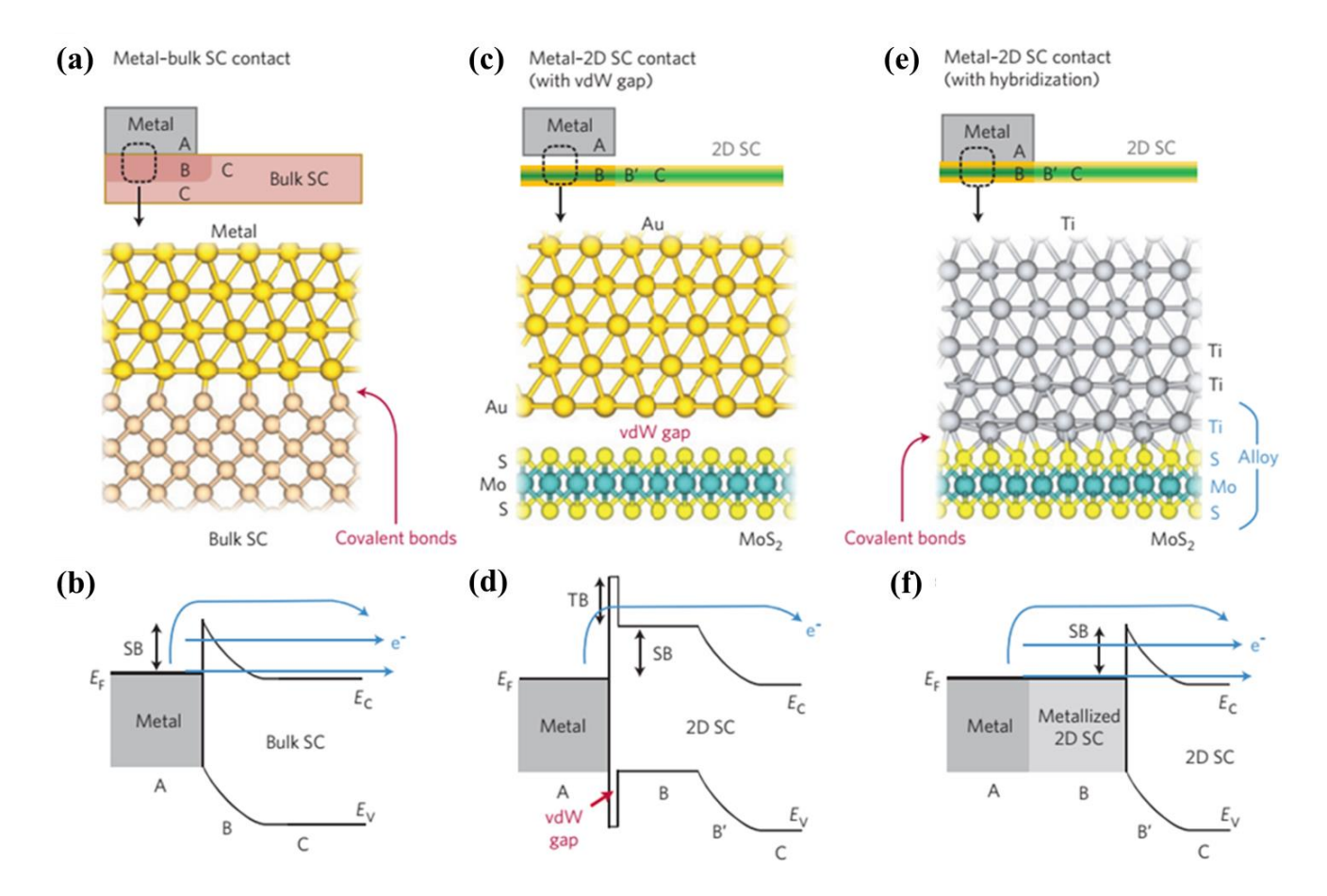


Figure 8. Types of metal—Semiconductor junctions and their respective band diagrams. a,b, Schematic (a) and corresponding band diagram (b) of a typical metal/bulk SC interface. c,d, Metal-2D SC interface with vdW gap (for example, Au- MoS_2 contact). e,f, Metal/2D SC interface with hybridization (for example, Ti- MoS_2 contact, where MoS_2 under the contact is metallized by Ti). E_F , E_C and E_V represent the Fermi level of the metal, and the conduction and valence bands of the 2DSC, respectively. T_B and S_B indicate the tunnel and Schottky barrier heights, respectively. A, B, B' and C represent different regions in the current path from the metal to the SC. The blue arrows in b, d and f represent the different injection mechanisms. From top to bottom: thermionic emission, thermionic field emission and field emission (tunnelling). In d, only thermionic emission is available [39].



In contrast to the argument supporting strong hybridization for contact formation, which can

help suppress the tunnelling barrier, another fundamental issue arises due to Fermi level pinning (FLP). This phenomenon occurs at the metal-2D material interface, where an abrupt change in work function leads to the creation of gap states. These gap states result from weakened intralayer bonding within the 2D material, effectively pinning the metal work function near the Fermi level of the 2D material. This pinning effect creates high Schottky barrier heights for carrier injection, which in turn increases contact

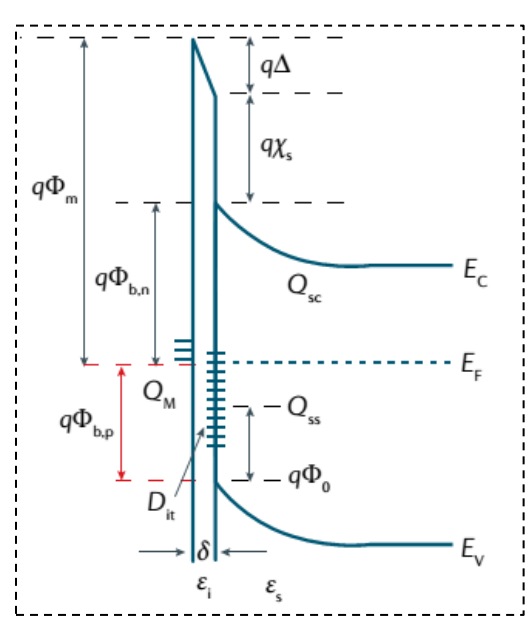


Figure 9. Metal Induced Gap States in a metal-semiconductor interface. [38]

resistance. As a result, while hybridization may offer certain benefits, it can also introduce challenges that negatively affect the performance of 2D material-based devices by impeding efficient charge transport.

Next an in-depth discussion on the origin and role of FLP in 2DLM optoelectronics is presented. The origin of FLP can be explained in 3 ways for 2D semiconductors. [38,46]:

- (i) Formation of metal-induced gap states (MIGS) between 2D semiconductors and 3D metals, which is also present in 3D metal-3D semiconductor junctions. These states serve as a reservoir for electrons or holes and therefore pin the FL and allow little variation of ϕ_B tuning.
- (ii) An interface dipole formed by the charge redistribution at the interface can shift the electronic levels from their original positions, leading to a deviation from the Schottky-Mott limit. The formation of these dipoles could be attributed to metal vacancies, metal like defects and substitutional impurities [47].



(iii) Defects at the interface (created during metal/material/device fabrication) could generate gap states that pin the FL, yet this can be neglected for a high-quality interface.

Further elaborated illustration of FLP can be found in figure 9. The figure illustrates the formation of mid-gap states that partake in the FLP. For most practical experimental cases, the Schottky barrier is found to be independent of the metal work function. This is because of the presence of defects at the metal-semiconductor interfaces as there is a distribution of mid-gap states. As a result of these defects, the Fermi level is consistently pinned at their mid-gap energy level and, therefore, the barrier height is determined by the mid-gap states, which is now independent of the work function of the metals, details of which can be found in [38].

2.5.2. Route to weakened FLP and efficient charge injection and extraction:

In this section we describe some methods reported in the literature to decouple direct interaction of the metal and 2D semiconductor to weaken FLP, which allows a more practical approach to modify the Schottky barrier height (SBH) at the metal—semiconductor contacts by using metals of different work functions. The literature available could be broadly categorized into 4 distinct methods:

- 1. Utilizing ultra-thin insulating tunnel barrier for deposited metal contacts.
- 2. Utilizing vdW metal-2DSC interface from prefabricated contacts.
- 3. Utilizing vdW metal-2DSC interface via decomposable buffer layer for deposited metal contacts.
- 4. Utilizing soft deposition techniques.

The first of the methods described is by utilizing a thin insulating layer between to the metal and 2DLM. Suppression of MIGS in the semiconductor can lead to a weakened FLP as



discussed earlier. This can be achieved by a lot of methods. One of them can be to use a separation layer between the metal and 2D semiconductor. Using a very thin layer of hexagonal boron nitride (h-BN) is one option. Transferring monolayer h-BN on top of the 2D semiconductor and then depositing metal on top of the h-BN, will prevent direct interaction between the metal and 2D semiconductor. This will help in two ways. Firstly, it will prevent damage to the 2D semiconductor and preserve its lattice structure during metal deposition and secondly as the metal is not directly deposited on top of the 2D semiconductor, strong hybridization between the metal and 2D semiconductor is restricted and the chances of MIGS is reduced. h-BN has pristine surfaces with electrically insulating nature and when it is made sufficiently thin, it acts as a tunnel barrier allowing efficient injection of charge carriers into the 2D semiconductor [48–50]. A schematic illustration of the method is provided in figure 10.

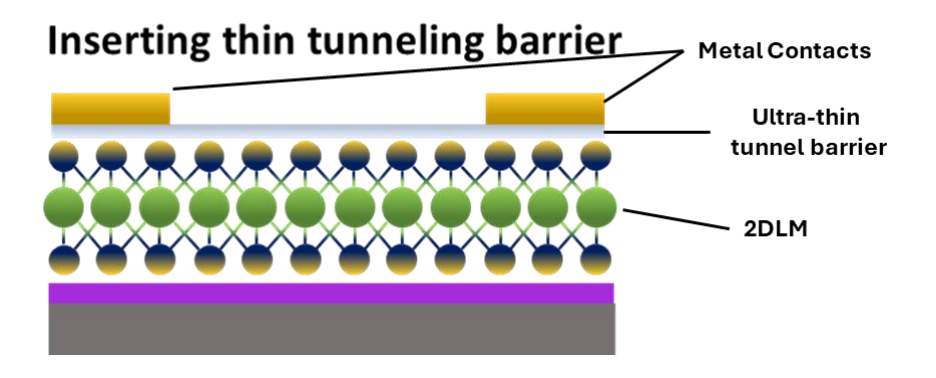


Figure 10. Inserting ultra-thin tunnel barrier for weakening FLP.

Wang et al. [48] demonstrated MoS_2 FET with high carrier mobility by lowering the SBH utilizing 1-2 layers of h-BN. They demonstrated that the SBH can be greatly reduced using very thin layers of h-BN with very low tunneling resistance. Additionally, increasing the thickness of the h-BN did not necessarily alter the SBH but increased the tunnel resistance. Their optimized h-BN thickness resulted in a low contact resistance of 1.8k $\Omega\mu$ m with SBH of 31meV for h-BN-Ni-Au.



With similar approach, Cui et al. [49], achieved low temperature ohmic contacts by inserting a h-BN layer between MoS₂ and Co-Au contacts. They obtained a flat band SB of 16meV, with lowest contact resistance of $3k\Omega\mu m$ for their h-BN-Co-Au contact pads. Li et al. [50] achieved gate controllable, ambipolar MoS₂ FET using a few layers tunnel barrier for Au contact. The device exhibited both p-n junction and n-p junction characteristics for gate voltage V_g of -3V and 0V respectively while from V_g =4V and above, the device displayed asymmetric full pass rectifying characteristics, with subthreshold swing for p-type characteristics of 230mV/decade at V_{ds} =+2V. Similar tunnel barriers can be achieved using other oxide materials such as Titanium dioxide (TiO₂) (for MoS₂ with Co [51], Black Phosphorus (BP) with Co [52], MoS₂ with various metals such as Ti, Ni, Au, and Pd [53] and MoS₂ with Au [54]) and Aluminum oxide (Al₂O₃) (for MoS₂ with Py-Au [55] and for WS₂ with Cr [56]).

Another alternative route to weakened FLP could be by suppressing MIGS with the utilization of a vdW junction between metals and 2D semiconductors. For 2D materials having very pristine surfaces, the FLP can be weakened by allowing Metal Semiconductor Junctions (MSJ) to be formed via vdW interaction. This phenomenon will allow tuning of ϕ_B , by using different metals, provided they maintain a vdW gap between themselves and the 2D material underneath. This potentially results in the concept of creating a metal semiconductor vdW junction, in short we refer hereafter as vdW-MSJ. However this cannot be achieved by direct deposition of metals on top of 2D semiconductors as this will distort the lattice structure of the 2DSC and introduce defects at the metal semiconductor interface [38]. Having the ability to tune ϕ_B will potentially open the door to many improvements in electronic device performance, including reduced contact resistance, having the ability to modulate carrier polarity in the channel materials for transistors, and enhance selectivity of carrier extraction for photovoltaic cells.



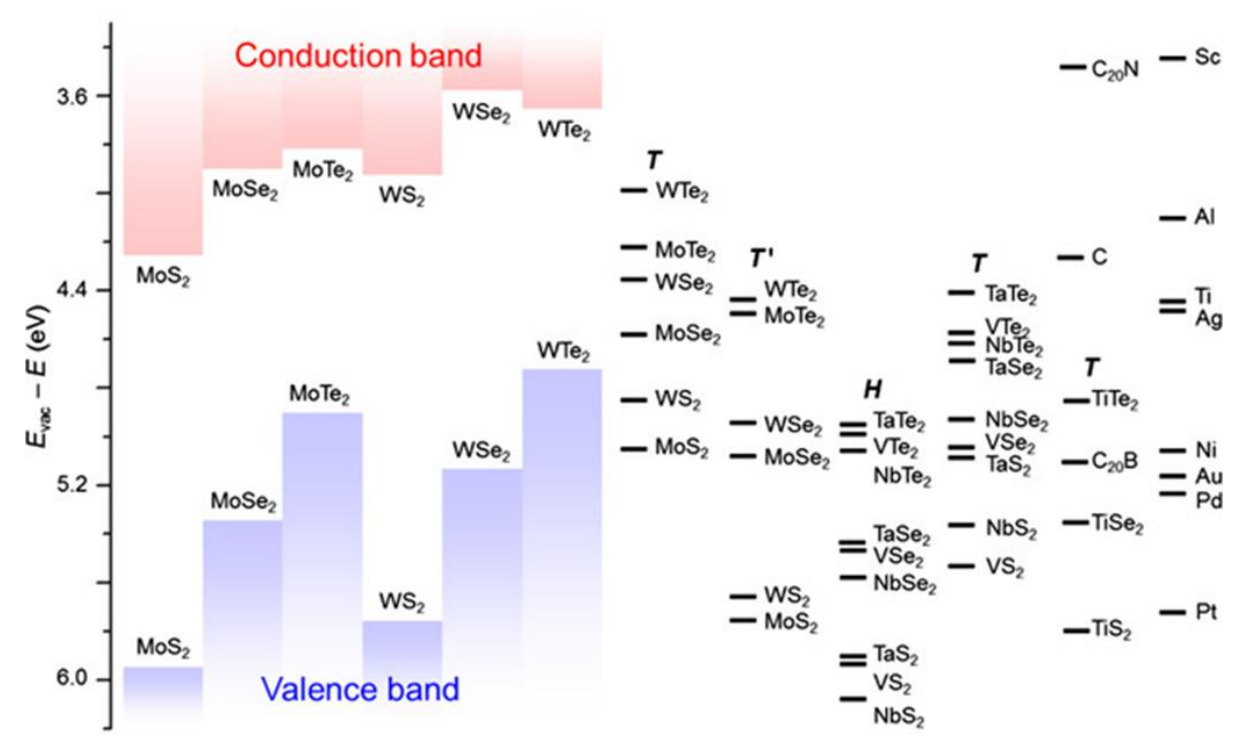


Figure 11. DFT Calculated band alignment between 2D metals and semiconductors and real 3D metals work functions. Columns on left show the electron affinity and ionization potential of semiconductors. Right column shows work function of 3D metals. The phase is labeled in italics [46].

A carefully designed photodetector requires work function matching of the metals to the active material when it comes to efficient carrier collection. When light is shined on a photoactive material, electron hole pairs are generated. The electrons are available in the conduction band while the holes are available in the valence band. For ideal cases of device design, the electrons should be collected using a contact metal, that has low work function, creating negligible Schottky barrier for the electrons in the conduction band, minimizing the contact resistance, while the holes should be collected using a high work function contact metal, that can easily access the valence band, with negligible Schottky barrier for the holes. Ideally, we can speak of a device that is created out of one active channel material, having two different metal contacts of different work function, creating asymmetrical contact geometry that will result in a rectifying Schottky diode and hence provide a built-in potential to create a self-powered



photodetector. Figure 11 illustrates work function for 2D and 3D metals, with respect to some commonly used 2D semiconductors that can be carefully chosen to design contact engineered photodetectors.

For achieving a pristine vdW metal-2DSC interface, the most elegant way is to prefabricate the metal electrodes on a sacrificial substrate and then transfer them from the substrate using PDMS/PMMA/Thermoplastic polymer on top of the desired flake to create a vdW MSJ based electronic device. Liu et al. [57] prefabricated 50nm thick metal electrodes (Au, Ag, Pt, Ti, Cr, Ni, Pd) on sacrificial substrate and then mechanically transferred them on TMDC flakes to realize vdW MSJ based FET. Subsequent electrical characterization revealed that the transferred electrode-based devices exhibited superior performance when compared to evaporated contacts on the same 2DLM, and in some cases presented opposite transfer characteristics to that of evaporated contacted devices. These results further substantiates that the devices using transferred metal contacts have weakened FLP compared to evaporated contacted devices. Zhang et al. [58] utilized a similar approach but used PEDOT:PSS to heal surface defects. As a result of this healing, the effects of FLP were further weakened and demonstrated SB free WSe2 FETs using Au transferred electrodes, with extremely high mobility and on/off ratio at very low biasing voltage. Went et al. [59] created Schottky junction TMDC based solar cell using vdW MSJ using similar transfer method. In their investigation, PDMS/PPC was utilized as the supporting polymer for efficient transfer of Au electrodes on top of WS₂, resting on a silver (Ag) bottom contact, initiating an asymmetric vertical Schottky junction. Furthermore, a comparison between evaporated and transferred contacted devices revealed a stark difference in their device performances, where the transferred metal contacts device displayed superior optoelectronic performance, compared to evaporated metal contacted device, with V_{OC} of 256mV, J_{SC} =4.10mA/cm², FF of 0.44% and PCE of 0.46% under one sun illumination. Liu et al. [60] prepared prefabricated 30nm Ag capped with 20nm Au on



sacrificial substrates, utilizing a similar technique to [57] and then transferred on to 1nm MoS₂ layer to create a-vdW vertical heterostructure FETs, with graphene as bottom electrode. Their study pushes the scaling limits of MoS₂ based devices and provides a general low-energy contact integration approach to vertical junction devices. Kong et al. [61] also prepared vdW MSJ contacted complementary WSe₂ circuit using vdW metal electrodes and evaporated metal electrodes. The vdW metal contacted device exhibited p-type FET characteristics while the evaporated metal contacted device exhibited n-type FET characteristics. Additionally, a probing of the electron and hole mobility of the devices revealed that for evaporated contacts electron mobility was in around $11\text{cm}^2\text{V}^{-1}\text{s}^{-1}$ while a hole mobility of $16\text{ cm}^2\text{V}^{-1}\text{s}^{-1}$ was observed for transferred contacts, realizing a complementary FET on same WSe₂ flake. Jung et al. [62] prepared via contacts that were prefabricated on h-BN with etched holes to create ultimate vdW MSJ, pristine top contacts that could realize almost FLP free devices. The via contacts were then transferred on top of a bilayer WSe₂ to create perfectly ohmic contacts with Au, realizing the first ever ohmic transferred contacts, that did not have edge connections, with 2R_c as low as $8k\Omega\mu m$.

The other alternative route for vdW MSJ interface could be utilizing a decomposable buffer layer. As outlined in figure 12, a buffer layer is first deposited on top of 2D material, followed by metal deposition, and subsequently the buffer layer is decomposed to form vdW MSJ.

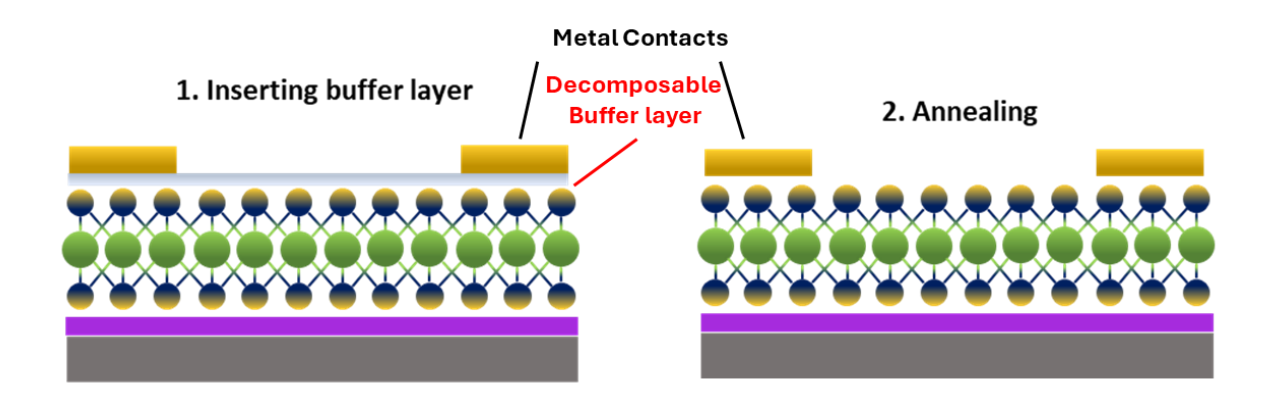


Figure 12. vdW metal-2DSC interface via 2 step decomposable buffer layer strategy.



To create a vdW-MSJ using buffer layer, Kwon et al. [63] utilized 10 nm thick selenium, that was pre-deposited on top of a number of TMDC. Later, metals of various work functions including Au, Ag, Pt, Co was evaporated on top of selenium and finally subsequent annealing at 150°C for 4 hours evaporated the selenium, leaving a vdW-MSJ between the metal and TMDC. They observed that their vdW MSJ WSe₂ FET with Ag exhibited n-type unipolar behavior, whereas Pt and Co contacted FETs exhibited p-type unipolar and p-type dominant ambipolar characteristics respectively, as was expected based upon the work functions and SBH. For MoSe₂, MoS₂ and WS₂, contacted with Au by direct deposition, the authors found that the despite have a large work function, the devices showed n-type behavior, whereas for vdW MSJ created by pre deposition of selenium and post Au deposition annealing for MoSe₂ and WS₂ FETs, the devices showed p-type dominant ambipolar behavior. In case of MoS₂, which is an n-type TMDC, with very high electron affinity, it was not possible to reach p-type operation using vdW Au contact. Kong et al. [64] created vdW-MSJ using a buffer polymer layer. In this approach, the authors utilized a thermally decomposable polymer buffer layerpoly(propylene carbonate) (PPC) on top of CVD grown WSe2, WS2, MoS2, MoTe2 and 2DLMs. The buffer layer was solution processed, and spin coated on top of the wafers to form a 450nm thick layer, followed by heating for solvent evaporation. Later on 50nm metals including Ag, Al, Ti, Cr, Ni, Cu, Co, Au, Pd were evaporated on the PPC coated channel materials, using a steel stencil mask. Subsequent annealing on a hotplate at 250°C in nitrogen environment for 30 minutes in a glovebox would gasify the PPC, leaving the metals on top of the 2D semiconductor, with a vdW gap. The authors extracted the contact resistance (R_c) for a range of vdW contacted metals to WSe₂, to form FET. Their control WSe₂ FET with evaporated contacts exhibited R_c of 33.82 k Ω - μ m, while vdW Au contact showed R_c of 10.2 k Ω - μ m, vdW Pd contact showed R_c of 5.3 k Ω - μ m, and vdW Pt contact with R_c of 1.6 k Ω - μ m, consistent with p-type behaviour of WSe₂ FET and lowered contact resistance due to increasing work function.



For vdW Ag and Ti contacts, R_c was obtained to be 27.5 $M\Omega \cdot \mu m$, and 3.9 $M\Omega \cdot \mu m$, respectively, showing very high SBH and increased R_c . Their findings opened a door for wafer scale fabrication of vdW MSJ and depinning fermi level for conventional bulk semiconductors including Ge GaAs, IGZO etc. While the abovementioned buffer layer method may show a sustainable route, the annealing step may still possess significant effect on hybridization of the metal to the 2DSC, as was previously discussed.

The fourth method widely adopted is the soft deposition technique where, soft metals are directly deposited on 2DSCs at very slow deposition rates, and have been found to weaken FLP. Wang et al. [65] deposited 10nm soft metal indium, capped with 100nm Au on top of WSe₂, MoS₂ and WS2 to realize vdW MSJ. Cross-section HRTEM analysis revealed pristine interface between each of the metals and 2DLMs. Additionally, their reported devices exhibited high mobility values when compared to high deposition rate evaporated contacts. However, the choice of soft metal is limited and cannot be widely utilized for device fabrication.

Alternatively, utilizing graphene as a diffusion barrier for the deposited metal can be a sustainable method. As illustrated in figure 13, patterned monolayer graphene is first transferred to the top of the 2DLM, upon which metal is vacuum deposited.

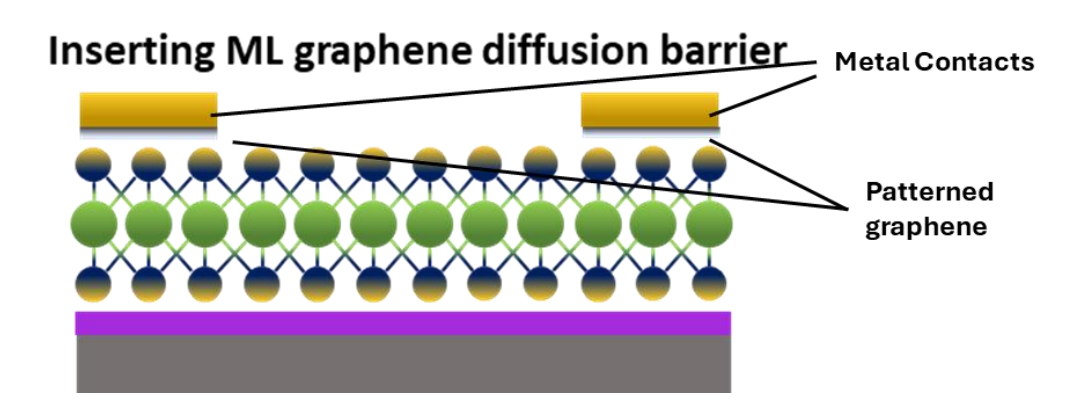


Figure 13. Using patterned graphene as a diffusion barrier for deposited contacts.



Overall, each of the methods mentioned above represents significant benefits at certain applications. However, "one size fit for all" cannot be concluded as all the mentioned methods have their own benefits and drawbacks.

2.5.3. Strategy for obtaining ultra-low dark currents:

Dark Current is an important figure of merit for photodetectors, especially for devices that operate in the infrared regime (IR). The implementation of infrared (IR) photodetectors using gapless semimetals and narrow bandgap semiconductors presents several challenges[66–68]. A primary concern is the high intrinsic carrier concentration resulting from thermal excitation, which is particularly problematic for devices operating in the 4-25 µm regime [(MWIR) and (FWIR)] [67–70]. For devices working at room temperature, the thermal energy of charge carriers can approach the transition energy across the bandgap. Consequently, devices experience significant dark current, a major source of noise. This elevated dark current can obscure weak IR signals, severely undermining the specific detectivity of photoconductive type devices operating under shot noise-dominated conditions. Therefore, outlining strategies for dark current suppression is crucial for optimizing the performance of photo sensors, especially working in the IR regime.

The composition of dark current and its influence is different in different types of photodetectors like photoconductors and photodiodes. In the case of a PC type photodetector, the PCE occurs when incident photons excite additional carriers and enhance the population of free carriers in the semiconductor. This resulting effect increases the available free carrier concentration partaking in the electrical conduction and reduction in the resistance of the channel material and successive modulation of the material's conductivity of channel. By applying external voltage bias across the contact terminals on the PC material, an elevated photo induced current can be generated as these excess carriers are collected through the



contact terminals. However, in the absence of light, the flow of majority carrier can arise from excitation (thermal) within the bandgap or from trap states across the bandgap, generating large dark current [71–73]. Under equilibrium conditions in dark, a photoconductor type device is predominantly influenced by thermalized injection of majority carrier from the conduction band to the valence band. The equation for thermal excitation probability indicates that, in narrow bandgap semiconductors, electrons at the maxima of the valence band have more probability to transition to the minima of the conduction band via band-to-band thermal excitation or background radiation at elevated temperatures, overshadowing the photogenerated carriers by weak light pulses and severely hampering the detectivity of the device [74,75]. Additionally, the shot noise associated with dark current predominates in device noise primarily from the defect induced trap states, particularly as it escalates at higher frequencies, further limiting detector sensitivity. Consequently, the high dark current generated by semiconductors with narrow bandgaps results in a inferior signal-to-noise characteristics, constraining the performance of photodetectors at room temperature specially in the IR regime. The case is different for photodiode type devices. In photodiodes, the flow of majority carrier can be obstructed by the p-n junctions due to its inherently pronounced interfacial barrier in the depletion region. The dark current composition in photodiodes consists of several

- (a) **Diffusion Current**: Arising from the movement of carriers due to concentration gradients [76].
- (b) Generation-Recombination Current [77]: Resulting from the creation and annihilation of electron-hole pairs within the depletion region.
- (c) **Band-to-Band Tunneling Current** [78]: Occurring when carriers tunnel directly from the valence band to the conduction band.

components, including:



- (d) **Trap-Assisted Tunneling Current** [78,79]: Involving carriers tunneling through trap states in the bandgap.
- (e) **Impact Ionization Current** [80,81]: Generated when high-energy carriers create additional electron-hole pairs through collisions.

More recently, several methods have been outlined to reduce dark current in 2D photosensors, including the design of heterostructures, introducing interfacial passivation and electrical modulation. By combining the advantages of different 2D materials and rationally aligning their bandgaps through the formation of heterojunctions or homojunctions, a barrier at the interface can be effectively introduced to oppose dark current. The techniques could be broadly classified into 3 key strategies:

- 1. Utilizing Band Alignment Engineering (Type-II and Type-III)
- 2. Localized field modulation (Gate or Ferroelectricity).
- 3. Repression of trap state induced dark current utilizing interfacial barrier.

2.5.4. <u>Utilizing Band Alignment Engineering for dark current</u> suppression:

Combining the diverse photoelectrical properties of vdW-m with the assembly of homojunctions or heterojunctions is an effective approach to hinder dark current. In this configuration, the built-in potential helps by blocking the unhindered flow of majority carriers, thereby enhancing the performance of the photodetector. As outlined in figure 14, the most prominent strategy for suppression of dark currents is to utilize type-II or type III heterojunctions, by carefully choosing the bandgaps of the materials.



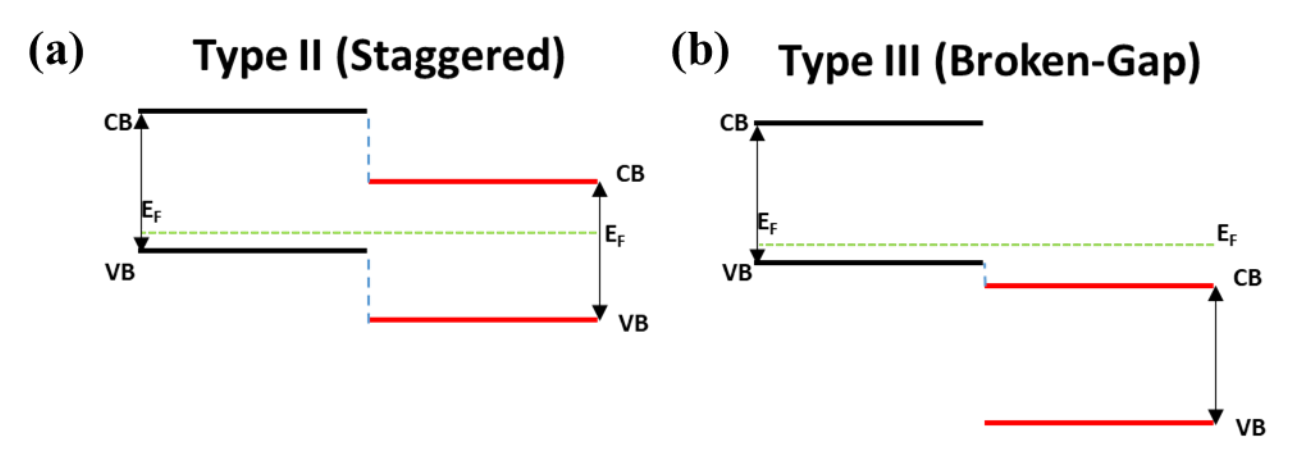


Figure 14. (a) A type-II (Staggered) heterointerface band alignment (b) A type-III (Broken Gap) heterointerface band alignment

As outlined in figure 14a, constructing a vdW heterointerface demonstrating a straddling (type-II) band alignment is a practical method for achieving low dark currents. The electric field at the heterointerface created by the type-II band alignment can effectively split photogenerated carriers, ensuring a rapid photo response speed. Moreover, the heterointerface potential barrier at the interfaces of the vdW heterojunction can efficiently suppress dark current, further enhancing detector performance. Most of the vdW heterointerface photovoltaic type devices are constructed utilizing this method [66,82–84].

Figure 14b illustrates a broken gap type-III heterointerface. Utilizing a prominent band alignment induced hefty band offset and extreme heterointerface potential barrier, a type-III heterointerface promotes suppression of thermally induced dark current, demonstrating excellent photoresponse speed and large on-off ratio. Reports of excellent type-III band alignment induced photodetectors include vdW WSe₂/BiSe₃ [85], SnSe₂-MoTe₂ [86] and mixed dimensional HgCdTe/BP [87].



2.5.5. <u>Utilizing localized field modulation induced suppression of dark</u> currents:

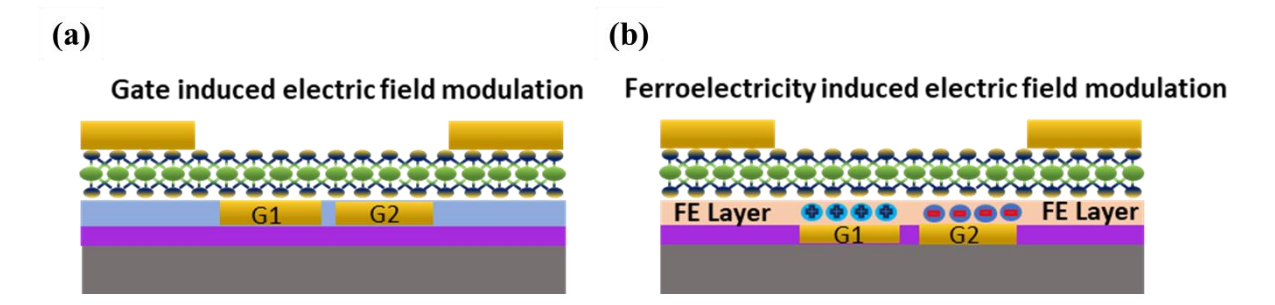


Figure 15. Localized field modulation induced dark current repression (a) Localized Gate-field using split gate(b) Localized Ferroelectric-field

The localized field modulation induced suppression of dark current is another method that is broadly used in generating pseudo type-II or type-III band bending in pristine 2DLM based photo FETs to mimic a p-n homojunction. In this process localized vertical fields are generated utilizing split gate technique to artificially deplete the 2DLM as illustrated in figure 15a. Gate terminals G₁ and G₂ are biased with opposite polarities to generate a local pseudo p-n junction that functions like a type-II or type-III band alignment with depletion regions and potential barriers to suppress thermally generated dark currents, enhancing the performance of the device. Examples of utilizing gated techniques include WSe₂/SnSe₂ [88] and MoTe₂ p-i-n [89] heterojunctions, where band alignments were effectively tuned to achieve type-III and type-II pseudo band alignments, respectively.

A more elegant way to achieve the same outcomes as the split gate technique reported above could be to utilize a thin ferroelectric layer above the split gate to spontaneously polarize the ferroelectric layer, without the need for continuous gate voltage application as illustrated in figure 15b. The opposite polarity of the gate voltages applied can spontaneously polarize the ferroelectric layer with desired out-of-plane dipole induced electric fields and generate robust local pseudo p-n junction that functions like a type-II/type-III band alignment with depletion



regions for suppressing the dark currents. Multiple authors successfully demonstrated spin-coated PVDF-TrFE as the ferroelectric layer and developed homo junctions of MoS₂ [90] and MoTe₂ [91] and heterojunctions of GeSe-MoS₂ [92] while BiFeO₃ was utilized as a ferroelectric layer for a WSe₂ p-i-n homojunction [93].

2.5.6. Repression of trap state induced dark current utilizing interfacial engineering:

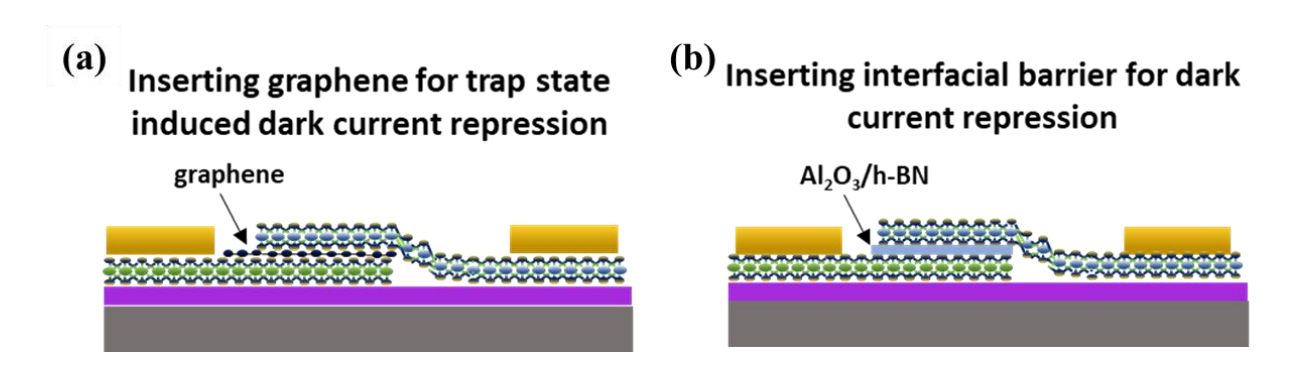


Figure 16. Repression of trap state induced dark currents utilizing (a) graphene as interfacial recombination repressor or (b) interfacial barriers (Al_2O_3/h -BN) as repressor.

Defects within the semiconductor play a crucial role in determining the photoelectric performance of the device. The defects are hot spots for generation and recombination related phenomenon and contribute to the extension of the lifetime of carrier by trapping one type of photogenerated carrier in photogating operation modes [94]. While the abovementioned phenomenon is helpful for specific applications, the defects within the heterojunction result in unwanted trap-related generation-recombination routes affecting figure of merits of photodetectors such as sensitivity [95]. To overcome the issue, engineering of the interface via surface passivation or intercalation n can significantly reduce defects at the heterointerface [96,97]. This improvement helps suppression of heterointerface trap-related dark currents and noise, enhancing the overall performance of the device, including sensitivity to weak light signals. Moreover, the suppression of recombination of photo-carriers in the interface would



reduce the losses of photo-generated electron hole pairs, enhancing the overall photo-to-electric conversion efficiency [98]. As outlined in figure 16a, graphene could be utilized as an interfacial recombination repressor in a heterojunction to combat trap induced losses. Graphene, being a semimetal with zero gap, has large number of free electrons resulting from the overlap of its band structure [98]. Reports indicate that when graphene is assembled onto the surface or at the heterointerface of heterostructures, these free electrons can populate defect and trap related states at the heterointerface. This filling process efficiently suppresses interlayer recombination and minimizes the loss of photogenerated carriers [98–101]. Wang et al. [102] utilized intercalated graphene between the interface of BP-InSe heterojunction to successfully suppress SRH recombination processes, while Seo et.al [100] used graphene passivation for MoS₂-p-Si heterojunction for suppression of dark current with enhanced device performance at 940nm. Another characteristics method is by introducing insulating oxides like Al₂O₃ or h-BN in between the heterojunction as illustrated in figure 16b. Wu et al. [103] demonstrated a WS₂-AlOx-Ge mixed dimensional heterojunction that can effectively detect up to 4.6µm, while Zhu et al. [97] demonstrated PtSe₂/n-Ge heterojunctions with Al₂O₃ as ultrathin interfacial barrier for suppressing dark currents.

2.5.7. Role of underlying substrate on ultra-thin 2DLM:

Properties of 2DLM tend to be modulated by the underlying substrate when they are in the ultrathin regime. Properties such as Schottky barrier, bandgap and fermi-level has been experimentally proven to be affected by the underlying substrate. The origin of this phenomenon could be due to multiple factors, including charge transfer, trapping-recombination of charge carrier and difference in the dielectric constant. For instance, the use of h-BN as substrate has been proven to enhance mobility of the device due to suppression of scattering and screening of charged impurities. Similarly, a difference in the dielectric constant of the underlying substrate could effectively modulate the band structure of a 2DLM, as was



illustrated by Utama et.al [104]. The authors utilized substrates of different dielectric constant (cytop ϵ =2.0 and h-BN=5.0)- to tune the band structure of a MoS₂ flake to achieve a homojunction diode. Alternatively, the dielectric properties of underlying substrate could directly influence the dielectric properties of the overlaying 2DLM, as was noticed for graphene on h-BN [105]. Moreover, bandgap renormalization due to the work function of the substrate could significantly impact the Schottky barrier between metal and 2DLM, as was observed for the case of MoS₂ [106]. A similar report could be found for the case of WS₂-Graphene heterointerface, where exciton interactions were observed to be influenced by h-BN-Gr spacer layers, effectively, modulating the charge carrier densities by 20% [107].

2.5.8. Role of layer thickness on position of fermi-level:

Recently, in-depth investigation utilizing kelvin probe force microscopy (KPFM) on the number of layers of WSe₂ and WS₂ have shown that, altering the number of layers could significantly change position of fermi-level. Liu et. al [17], demonstrated that with increasing thickness of WSe₂, from 4nm to 30nm, a significant change in the fermi-level was observed to lower energy values, where the work function of WSe₂ flake decreased significantly, portraying substantial n-doping. This finding is crucial as WSe₂ has been widely reported as a strong p-type semiconductor. Their systematic investigation substantiated that for device optimization, specially for robust p-n junctions, researchers must consider keeping WSe₂ thicknesses to very thin regime, which would substantially increase the efficiency of photoelectric conversion. Utilizing a similar method, Yu et al. [108] demonstrated a work function tuning, based on layer thickness of WS₂, suggesting more electron dominating transport characteristics as the thickness increased from few layers to 10 layers. The authors also explained the role of optimized thickness of WS₂ played in their type-I heterojunction between WS₂-Te for robust photodetection.



Overall, the literature review of various synergistic optimization strategies for device performance leads to the conclusion that a clear understanding of the 2DLM-metal interface is crucial. This interface often represents a significant bottleneck in charge extraction, primarily due to two factors:

- 1. **Metal-Induced Gap States**: These states can facilitate unwanted recombination mechanisms and the thermal injection of dark currents, which severely undermines photoconversion efficiency and increases noise related to dark current.
- 2. **Fermi Level Pinning (FLP)**: The metal work functions may be pinned to mid-gap states, making it challenging to change the metal work functions to achieve true ohmic contacts.

Furthermore, it is evident from the preceding discussions that stacking 2DLMs without considering the effects of layer thickness can negatively impact device performance due to poorly optimized heterojunctions. Thus, addressing these interface challenges and carefully designing layered structures are essential for enhancing the efficiency and effectiveness of 2DLM-based optoelectronic devices.

2.6. Conclusion:

Overall, for optimizing optoelectronic device performance, a synergistic-approach has been probed from the literature and discussed indepth. This chapter began with a comprehensive overview of two-dimensional layered materials (2DLMs), highlighting key material characteristics that impacted their applications in optoelectronics. These characteristics included crystal structure, absorption properties, bandgap relationships, and carrier mobility.

Following this introduction, we presented the figures of merit for photodetectors, accompanied by a broad classification of 2DLM-based photodetectors and an explanation of their operational



principles. A succinct literature review then provided context for the topics addressed in this thesis, leading to a detailed discussion on the synergistic optimization of photodetectors and their significance in advancing optoelectronic technologies. This thorough examination aimed to underscore the potential of 2DLMs in enhancing device performance and addressing contemporary challenges within the field.



Chapter 3: All van der Waals GaS-WSe₂ photodiodes: Synergistically engineered for Multifunctional Optoelectronics:

3.1. Introduction:

Multivariate optimizable strategy in vdW heterojunction is a crucial aspect of research in the context of vdW heterostructure photodiodes. Among them, transitional metal dichalcogenides (TMDC) and metal monochalcogenides are equally imperative vdW-m for optoelectronic sensing applications, due to enhanced light matter interaction, high charge carrier mobility, layer dependent tunable bandgaps-all in the ultra-thin regime of few atomic layers [109,110]. GaS, a layered post-transition metal monochalcogenide, has demonstrated excellent lightmatter interaction in the ultraviolet-visible regime[111]. Its remarkable structural [112] and phonon dynamics characteristics [113], suggest promising applications in flexible optoelectronics. However, the reported low intrinsic in-plane mobility has hindered its progress in realizing in-plane self-powered photo-sensors, till date. Earlier it was suggested that ultrathin films of gallium monochalcogenides could be suitable active element candidates for ultraviolet photon harvesting in vertical tunneling transistors [114]. Besides, double peak valence band maxima, as theoretically predicted for ultrathin GaS, encourage photo absorption [111], making them suitable for optoelectronic heterojunction devices. Thus far, reported photoconductive type bare GaS [115,116], defect-based GaS devices [115] and heterojunction devices like Gr-GaS-Gr [116] and GaS-WS₂ [117] required large operating voltages and demonstrated sluggish response speeds, necessitating renewed investigation into favorable layer thickness determination, device structure and contact engineering approaches, conducive to self-powered applications and faster response speeds. It is well established that self-powered heterojunction optoelectronics benefits from type-II heterointerface facilitating band bending and enhanced



charge carrier separation [118]. However, shift of the band edges and fermi-level owing to impetuous layer thickness modification and emergence of refractory Schottky barrier at the contact regions due to FLP, could nullify these type-II junction benefits. This is especially critical for large bandgap vdW-m like GaS and its heterojunctions, which have not yet been thoroughly investigated. The selection of number of layers is subjective to the applications of the constituent material and may not be universal for every aspect, however a clear strategy has been already adopted for FLP free application of vdW-m, owing to recent investigation of vdW transfer metal contacts for efficient current injection in FETs [57,119–121] and photocarrier extraction in solar cells [59]. Hence, with meticulous engineering strategy, we report a photovoltaic type-II, "all van der Waals" GaS-WSe₂ heterojunction photodetector, having thickness, structure and contact optimized to achieve broadband detection response between 275 nm and 1064 nm regime, multispectral unity approaching linearity, with a significant linear dynamic range of 106.78 dB. The device also exhibits a large on/off ratio of 10⁵, fast response speeds of 545/471 µs alongside ultra-low light detection capabilities with ~fA dark currents to achieve a peak responsivity of 376.78 mA/W and a detectivity of 4.12 × 10¹¹ Jones with stabilized EQE of 30% and fill factor of ~0.33; all achieved through a single junction and a name coined "all van der Waals" due to the integration of the metal contacts with intimate vdW interaction. Moreover, our systematic investigation on multiple a-vdW devices along with a control device fabricated using traditional electron beam lithography (EBL) pattered contacts for comparison, covering key performance attributes such as junction potentials, electronicoptoelectronic characteristics, further endorse and emphasize the essential role of meticulous approach to thickness-engineered layers in establishing a robust depletion region for GaS-WSe₂ type-II heterojunction and modulating the Schottky barrier height via vdW metal contacts to achieve FLP free, vdW metal-2D material interface, beneficial to recombination resilient high linearity, striking a favorable balance among photocarrier generation-recombination,



separation, transport, and extraction, eventually facilitating a highly sensitive, broadband photodiode.

3.2. Results and Discussion:

3.2.1. Fabrication of heterojunction:

The fabrication process consists of two distinct steps: the fabrication of the heterojunction and the integration of the vdW metal contacts. Traditional scotch-tape/ PDMS based micromechanical cleavage and aligned dry transfer technique has been performed to obtain the vdW heterojunction. In short, scotch-tape was used to exfoliate h-BN, GaS and WSe₂ (HQ Graphene) and transfer to PDMS. The correct thickness of the flakes were identified under microscope using optical contrast and then transferred onto a previously ultrasonically cleaned [Acetone (2mins), IPA (3mins) and DI water (3mins)] and plasma treated [O₂ Plasma, 100W, 5mins] 300nm SiO₂/Si⁺⁺, sequentially by means of a homemade aligned transfer stage. The heterojunction was annealed under 50 sccm Ar flow at 180 °C for 1hr to increase coupling efficiency and ensure efficient charge transfer between the layers. h-BN was chosen as the dielectric material to provide potential screening from charged impurities and adsorbates on the SiO₂ surface [122] which could modulate the carrier transport characteristics [123], and influence the Schottky barrier height between the contacts and the underlying vdW-m [106].

3.2.2. Van der Waals contact fabrication and integration:

In the second step, vdW integration of Ag/Au (38 nm/22 nm) contacts was achieved through a modified transfer method using prefabricated contacts on a sacrificial substrate. The fabrication of vdW contacts can be explained in three primary steps: (i) fabrication of contacts on sacrificial substrates, (ii) pick-up and aligned transfer of the contacts to a previously fabricated



heterojunction using a thermoplastic, and (iii) removal of the thermoplastic to complete the device fabrication.

In brief, a 1 cm x 1 cm silicon substrate was spin-coated with photoresist (PR) (AZ5214E) at 5000 rpm to achieve a photoresist thickness of 1.25 µm. The PR-coated substrate was then baked on a hotplate for 1 minute at 110 °C. Subsequently, a chrome photomask, featuring electrode patterns, was aligned onto the substrate using a mask aligner (SUSS MA-6, Microtek). The PR-coated substrate was exposed to ultraviolet light at a wavelength of 375 nm for 5 seconds. Following exposure, the substrate was immersed in a developer solution (AZ300MIF) for 30 seconds with gentle agitation, then thoroughly rinsed with deionized (DI) water and dried using a nitrogen gun.

Metal deposition was executed through electron beam evaporation (Denton E-beam Explorer) employing a sequential deposition technique. Silver (Ag) was deposited at a rate of 1.2 Å/s at a working pressure of 4.2×10^{-7} torr to a thickness of 38 nm, followed by a gold (Au) capping layer deposited at a rate of 1 Å/s at a working pressure of 6.1×10^{-7} torr to a thickness of 22 nm. The liftoff process was initiated by placing the metal-deposited substrate in an acetone bath, where gentle shaking was applied to facilitate metal liftoff. Finally, the patterned substrate was rinsed sequentially with isopropyl alcohol (IPA) and DI water.

For the integration of patterned electrodes into the heterojunction, polyvinyl alcohol (PVA) thermoplastic was utilized for the pick-up and transfer process. In brief, a PVA-deionized water solution (0.083 g/ml) was prepared and allowed to bake overnight in a clean glass petri dish at 60 °C to facilitate hardening. A 5 mm x 5 mm piece of the hardened PVA was then cut out and placed on polydimethylsiloxane (PDMS).

The PVA/PDMS stack was aligned using a glass slide on an aligned transfer stage, and the PVA film was transferred onto the patterned electrodes at a stage temperature of 50 °C. The



electrodes, now wrapped in the PVA film, were carefully released from the sacrificial substrate using tweezers and subsequently transferred onto the designated heterojunction area. This transfer was executed using the same micrometer-aligned transfer stage, with PDMS serving as the carrier.

Once the electrode/PVA/PDMS structure was accurately positioned on the heterojunction, the substrate was heated to 50 °C and maintained in contact for 3 minutes. Following this, the PDMS was released at an angle to facilitate separation. To complete the formation of the a-vdW photodetector, the PVA support was dissolved in DI water, after which it was dried using a nitrogen gun. This approach minimizes FLP and enhances photocarrier extraction. A schematic illustration of this process is provided in Figure 17.

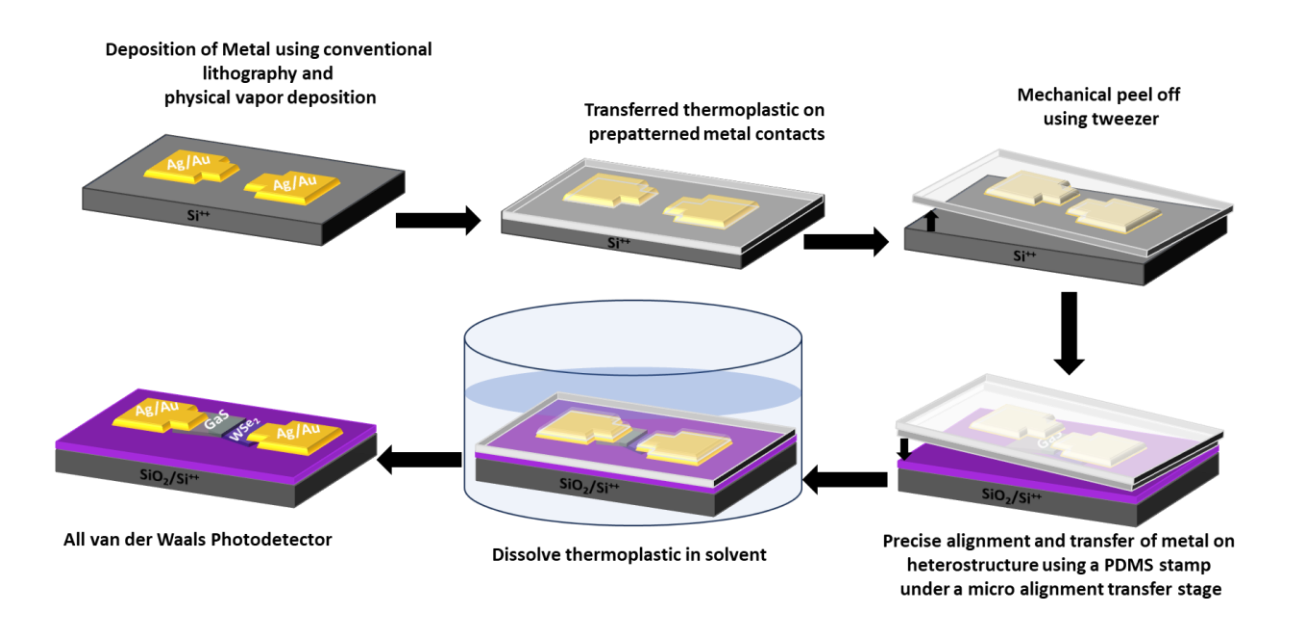


Figure 17. Integration of van der Waals contact to GaS-WSe₂ heterojunction.

The finalized device structure and schematic of the WSe₂-GaS vdW heterostructure and an optical micrograph of an a-vdW photodiode is illustrated in figure 18a and b respectively.



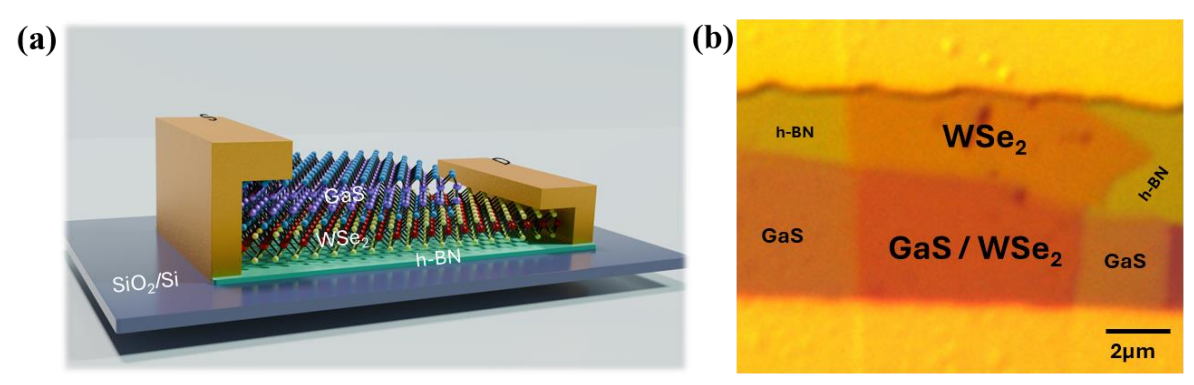


Figure 18. (a) Schematic Illustration of all van der Waals heterojunction photodetector (Purple and red spheres represent gallium and tungsten metal atoms, while blue and yellow spheres represent sulfur and selenium atoms respectively). (b) Optical micrograph image of the device.

3.2.3. Raman and Photoluminescence spectroscopic characterization of the heterojunction:

To better understand the layer coupling properties of the prepared heterostructure photodiode, we employed Raman spectroscopy, as shown in figure 19a. For few-layer GaS, the prominent vibrational modes A^1_{1g} and A^2_{1g} were identified at 188.16 cm⁻¹ and 359.58cm⁻¹, respectively, while the less prominent E^1_{2g} mode appeared at 296.01cm⁻¹, consistent with previous reports [124]. Likewise, few-layer WSe₂ exhibited a prominent in-plane mode E^1_{2g} at 249.58cm⁻¹ and a weak out-of-plane A_{1g} mode at 256.94cm⁻¹ [125,126]. In the overlapped region between WSe₂ and GaS, all peaks corresponding to the individual layers were observed, indicating a high-quality heterojunction. Moreover, to further investigate the charge transfer characteristics and coupling effects, we performed Raman intensity mapping and analyzed the photoluminescence (PL) spectra and mapping. As shown in the Raman intensity mapping for the peaks at 256.94cm⁻¹ and 359.58 cm⁻¹ in figure 19 b and c, we observed a notable reduction in Raman intensity—a phenomenon known as "Raman quench"—which signifies strong interfacial coupling between the GaS and WSe₂ flakes [84,122]. Raman quenching has been reported in many vdW p-n heterojunctions. They are likely attributed to two causes; Shielding effect by the upper layer which reduces the laser intensity and absorption of it and interlayer charge



transfer between the well coupled vdW materials due to their fermi-level difference [17,108]. The PL spectra in figure 19d reveal strong excitonic emission for bare WSe₂, while an obviously quenched PL spectrum is observed in the overlapping region.

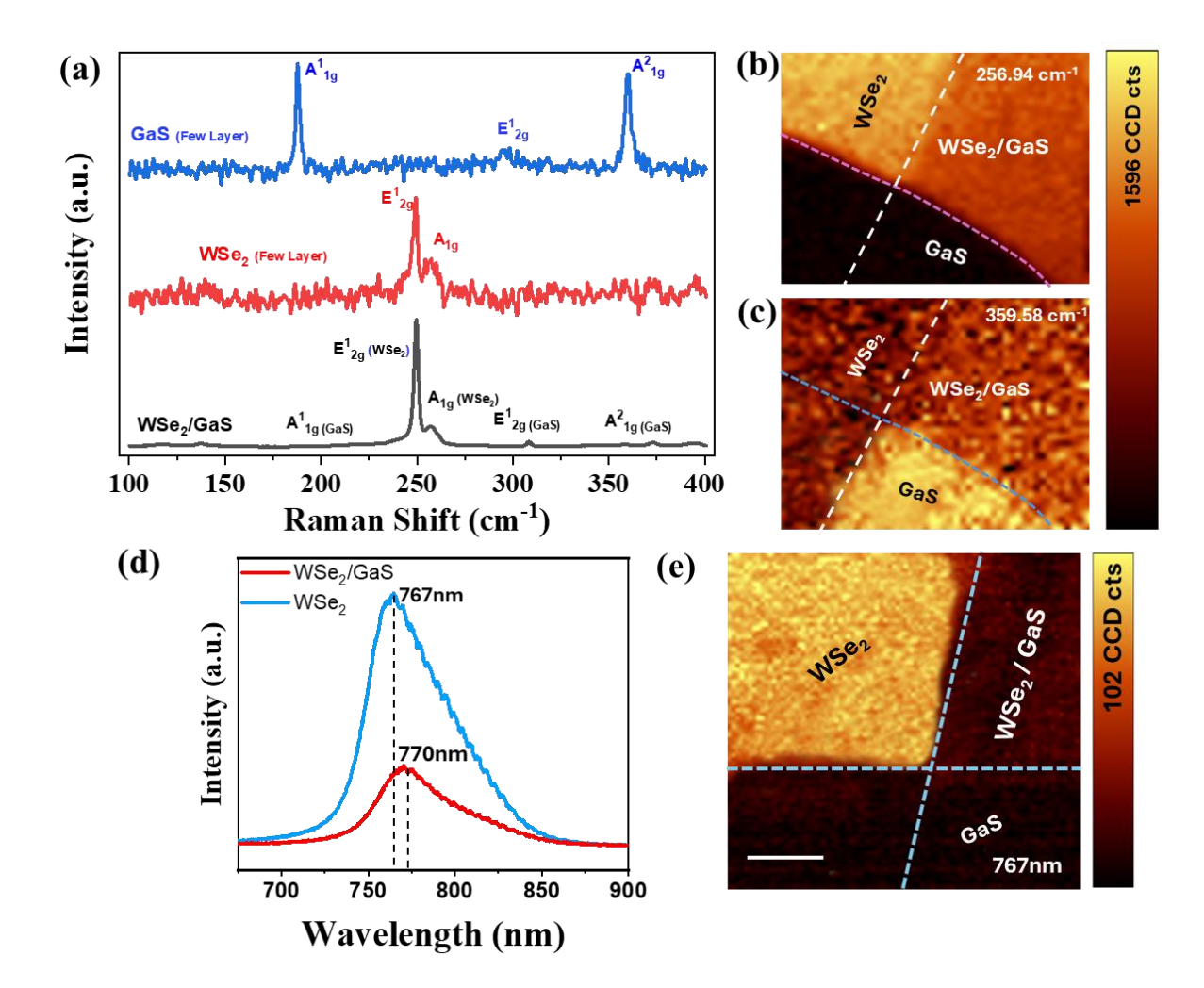


Figure 19. (a) Raman spectroscopy of few layer GaS showing characteristics A^{l}_{lg} , E^{l}_{2g} and A^{2}_{lg} modes, ultrathin WSe₂ showing characteristics E^{l}_{2g} and A_{lg} modes and the heterojunction region showing all the characteristics peaks. Raman mapping of (b) A_{lg} mode (256.94cm⁻¹) of WSe₂ (top) and (c) A^{2}_{lg} (359.58 cm⁻¹) of GaS, showing evident uniform Raman quenching in the overlapped regions for both the modes. (d) Photoluminescence spectroscopy of ultrathin WSe₂ in the bare and overlapped regions of the heterojunction, with the (e) showing the PL mapping. Evident PL quenching is observed from both the spectroscopy and mapping results.

Furthermore, the intensity mapping shown in figure 19e, demonstrates uniform quenching effects of PL intensity in the heterointerface region, indicating non-radiative recombination in the GaS-WSe₂ heterostructure and efficient separation of photogenerated electron-hole pairs



[15]. These results from Raman scattering and PL spectra indicate a well-coupled, pristine heterointerface suitable for photodetection mechanisms.

3.2.4. Estimation of band structure profile using UPS and KPFM and height profile using AFM:

To better understand the charge transport characteristics, ultraviolet photoelectron spectroscopy (UPS) was employed to determine the complete energy level alignment before contact. The work functions (Φ) of GaS and WSe₂ were estimated to be 4.19 eV and 4.38 eV, respectively, calculated from the difference between the second electron cutoff energy and the photon energy of the He I light source (21.21 eV), as outlined in figures 20a and b, from the following calculations.

The work function of a semiconductor could be obtained from the difference between the energy of the illuminating photon and secondary electron cutoff energy as follows:

The valence band edges of GaS and WSe₂ were found to be 2.41 eV and 0.38 eV lower than their respective fermi energies (E_l), as shown in the insets of those figures.

Additionally, we employed Kelvin probe force microscopy (KPFM) to investigate the fermilevel adjustments at the heterojunction after contact (figure 20c), revealing a surface potential difference (SPD) of approximately 200 mV across the heterojunction using the following equations.

$$eSPD_{GaS} = \varphi_{tip} - \varphi_{GaS} \tag{6}$$



$$eSPD_{GaS} = \varphi_{tip} - \varphi_{GaS} \tag{7}$$

Where e, φ_{tip} , φ_{GaS} and φ_{WSe_2} represents the work function of the SKPM tip, GaS and WSe₂, respectively. Consequently, the difference between the fermi level between GaS and WSe₂ could be written as:

$$\Delta E_f = eSPD_{GaS} - eSPD_{WSe_2} = \varphi_{GaS} - \varphi_{WSe_2}$$

$$\Delta E_f(device_1) = eSPD = 200 \text{ meV}$$
(8)

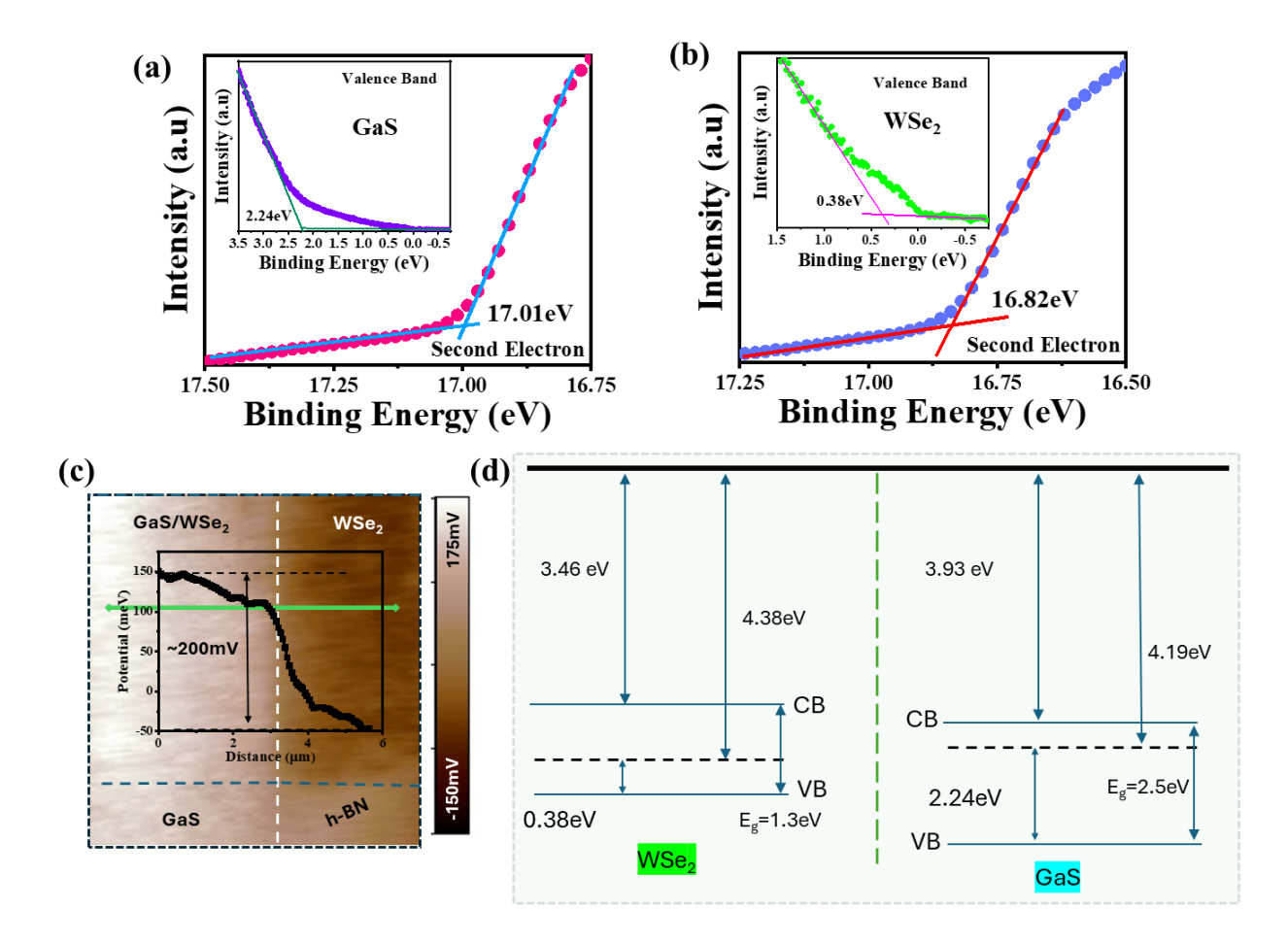


Figure 20. Inference of heterojunction band structure from UPS (a) Secondary Electron cut-off for GaS, with the inset showing the position of valence band edge. (b) Secondary Electron cut-off for WSe₂, with the inset showing the position of valence band edge. (c) KPFM image of the heterojunction region with corresponding SPD profile, showing a SPD of \sim 200 mV. (d) The proposed band alignment before contact, with various energies.

Notably, the fermi level difference between WSe₂ and GaS, measured at around 0.19 eV from UPS measurements, closely matches the results obtained from KPFM. Combining the insights



gained from KPFM and UPS, along with the reported bandgaps of 1.3 eV for few-layer WSe₂ [127,128], and 2.5 eV for GaS [129,130], the proposed type II heterointerface band diagram is illustrated in supporting section figure 20d.

Atomic Force Microscopy (AFM) was employed to obtain the height profile of the prepared heterojunction photodetector, as shown in figure 21a. The height profile analysis revealed the height of the GaS flake was approximately 8.5 nm, (~10 layers) (figure 21b), while the WSe₂ flake had a height of around 3 nm, (~4 layers) (figure 21c), confirming the thicknesses of the layers used in constructing the heterojunction.

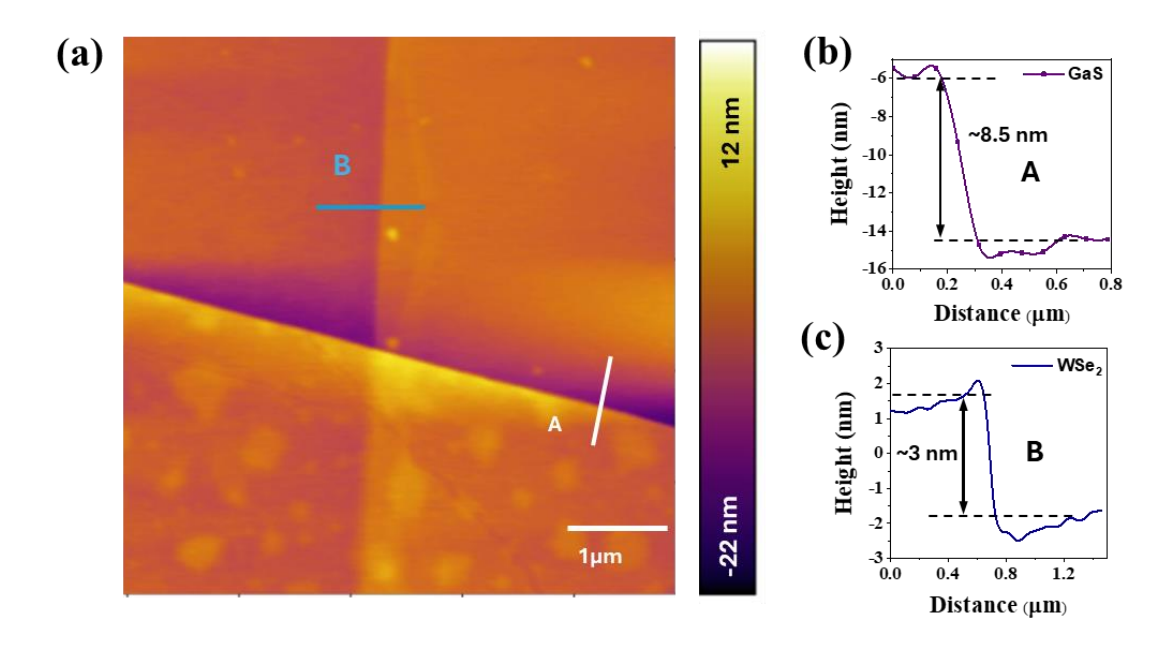


Figure 21. (a) AFM image of the heterojunction region with corresponding height profiles showing a thickness of (b) GaS and (c) WSe₂ layer of 8.5nm (region A) and 3nm (region B), respectively.

3.2.5. <u>HR-STEM and HAADF-STEM EDX analysis at the cross-</u> <u>section of a-vdW heterojunction:</u>

High-resolution scanning transmission electron microscopy (HR-STEM) was employed at the cross section of a device to verify the quality of a-vdW heterojunction region, as illustrated in figure 22. The investigated region consists of few-layer h-BN, ultrathin WSe₂, few layers of



GaS, encapsulated by vdW contact. The images reveal clean interfaces within the 2D-2D heterojunction, free of impurities and the 2D-metal interface shows an undisturbed, column-like structure of the naturally passivated GaS layers, maintaining a vdW gap without any perforation of metal into the GaS layer. This suggests a clean metal-vdWm interface, which is conducive to FLP free operation.

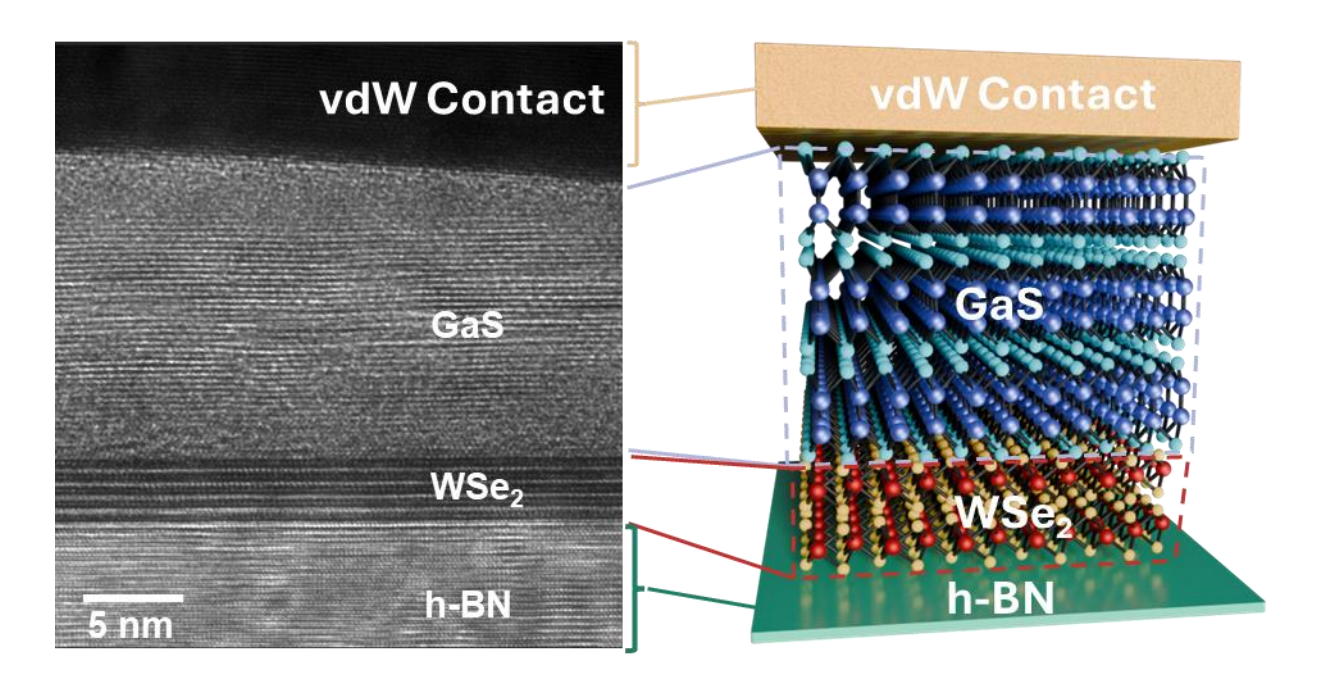
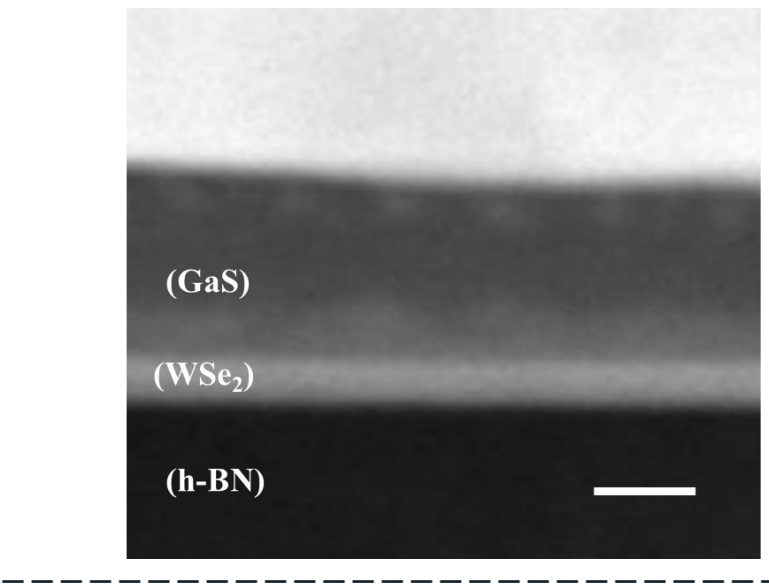


Figure 22. Cross-sectional HR-STEM image of the all vdW region of the heterojunction, showing (from bottom) h-BN, WSe₂, GaS and vdW contact, with pristine interfaces between constituent junctions.

Additionally, we utilized high-angle annular dark field (HAADF) STEM energy-dispersive X-ray spectroscopy (EDS) mapping to determine the elemental composition of the constituent elements at the 2D-2D interface (figure 23). The EDS results further complement the Raman and PL spectroscopic conclusions of a robust and pristine heterojunction, composed of GaS-WSe₂.





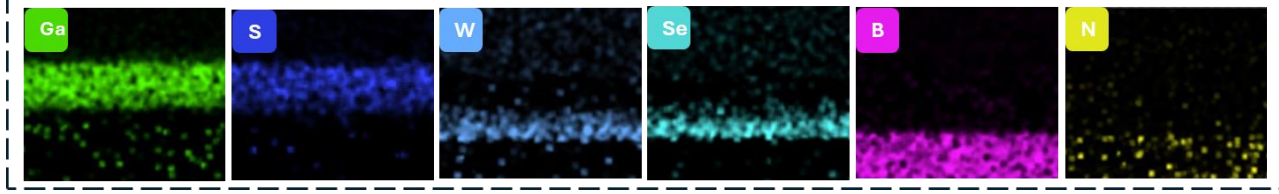


Figure 23. HAADF STEM image of the cross section of the heterojunction and EDX mapping of the elements in the heterojunction region showing presence of Ga, S, W, Se, B and N concentrations at respective vdW material layers.

3.2.6. Electronic transport characteristics of the GaS-WSe₂ a-vdW photodiode under dark conditions:

The charge injection mechanism in a vdW materials' interface has significant impact on numerous performance descriptor figures of merit, including contact resistance, current on/off ratio and response time of the device [131]. For vdW heterostructure devices, general approximation of the transport characteristics is well established within the framework of direct tunneling (DT) under Simmons model at low bias, Fowler–Nordheim (FN) tunneling model at cold field emission regime and space charge limited (SCL) emission regime [132]. To elucidate the electronic transport in the heterojunction, the I_d-V_d characteristics for the device was obtained (figure 24a, b and c). Drain voltage with positive polarity was applied to the WSe₂ side, while the source terminal at the GaS side was connected to ground. A clear rectifying



characteristic of a conventional p-n junction is observed in figure 24a with a rectification ratio of over 10^2 . Interestingly, the log-scale plot of the drain current reveals two distinct linear regions in the forward bias configuration; $0.01V < V_{ds} < 0.19V$, with a diode ideality factor (η) of ~ 1.6 and $0.2 < V_{ds} < 0.6V$, with an ideality factor of ~ 2.96 , in accordance with the Shockley diode equation. To understand the tunneling phenomenon, the forward current I_d - V_d characteristics was replotted as shown in figure 24b with three distinct regions. A low voltage DT regime is observed under low bias configuration (region (I)), and a FN tunneling regime (region (II)) with negative slope which could be expressed by the following expression [133,134].

$$I_{d} \propto \begin{cases} V_{d}e^{\left(-\frac{2d\sqrt{2m^{*}\phi_{T}}}{\hbar}\right)} & (V_{d} < V_{FNT}):DT \\ \left(-\frac{4d\sqrt{2m^{*}\phi_{T}^{3}}}{3\hbar eV}\right) & (V_{d} > V_{FNT}):FNT \end{cases}$$
(9)

where m^* is the electron effective mass, \hbar is the reduced Plank's constant, d is the barrier thickness, Φ_T is the tunneling barrier height. The tunneling threshold voltage, V_{FNT} of ~0.195V, could be obtained from figure 3b and tunneling barrier Φ_T could be estimated from this threshold to be roughly 0.195eV ($V_{FNT} = \Phi_T/e$). Upon further investigation, using a double log plot of the I_d - V_d characteristics as shown in figure 24c, one could notice that the DT region shows a linear regime portraying an approximate ohmic behavior, as expected in the case of DT effect in region (I), due to thermionic emission. The formation of band bending of the device under applied potential is illustrated in figure 24d. The barrier hindering the charge carrier is trapezoidal in this region as illustrated in figure 24d, region (I). Furthermore, the current is found to increase more rapidly in region (II) at a higher applied drain-source potential, the barrier tends to form a triangular shape and becomes narrower leading to FN tunneling (figure 3d region (II)). At much higher voltage (V_d >0.6 V), the current is limited by the space charge limited region (SPLC) [135] (figure 24d region (III)). The device shows a



rectification ratio of \sim 250, which could be further enhanced by forming asymmetric accumulation type contacts at both ends (i.e. a higher work function contact at the WSe₂ end and lower work function contacts at GaS). It is worth noting that the current of the device at V_{ds} = 0 V, is in the \sim fA range. Such ultra-low dark currents could be attributed to the type-II heterojunction, large valence band offset between the GaS and WSe₂ (evident from figure 20c), that suppresses minority carrier injection and the inherent vdW gap between the contacts and vdW-m that promotes MIGS resilient dark current suppression.

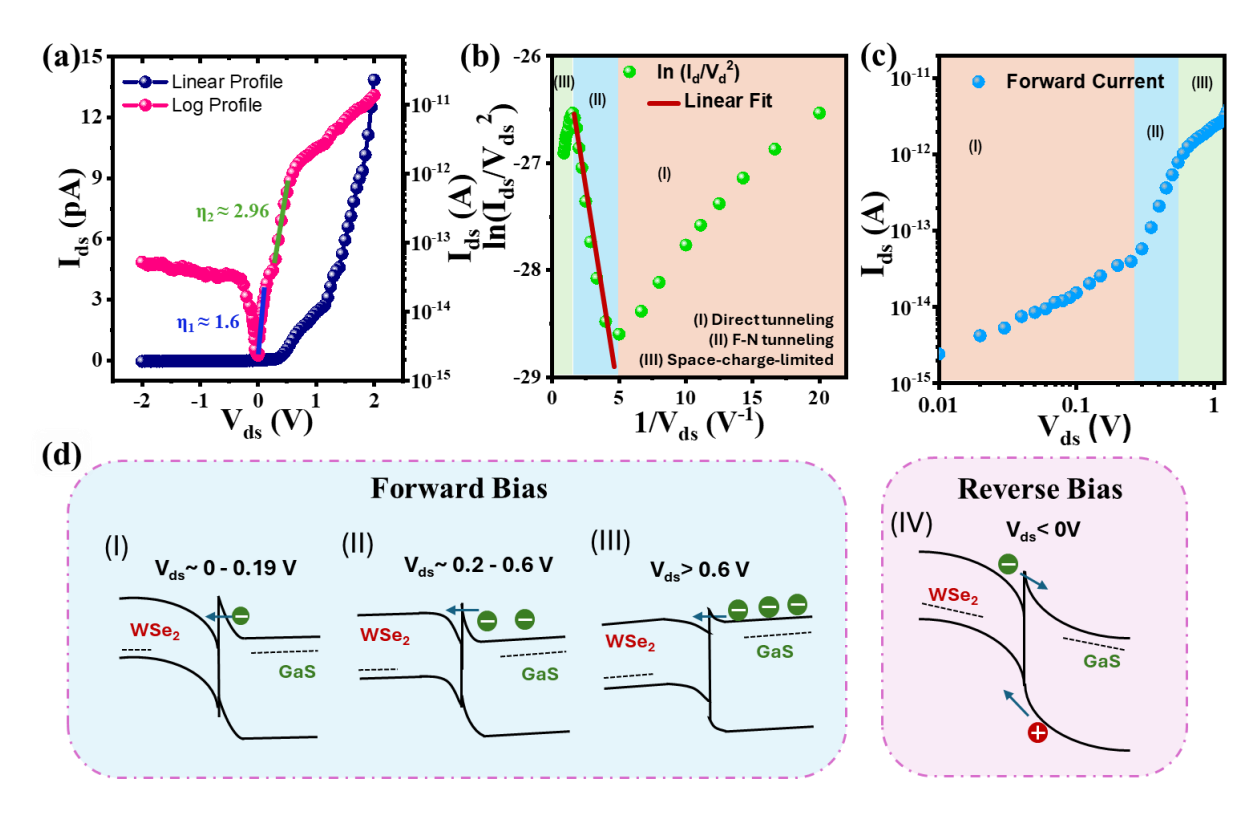


Figure 24.(a) Dark I_d - V_d profile of the photodiode, showing two distinct linear regions with ideality factor η_1 and η_2 of 1.6 and 2.96 respectively. (b) $\ln(I_d/V_d^2)$ vs $1/V_d$ plot of the diode forward current regime, showing 3 distinct operation regions (DT, FN and SPLC). (c) Double $\log I_d$ - V_d plot of the forward current. (d) Schematic illustration of transport characteristics of the photodiode under forward and reverse bias conditions.

3.2.7. Charge Transport of the device under illumination conditions:

We then examine the charge transport and excitonic transfer in our vdW heterojunction as outlined in the pseudo band diagram in figure 25. During quasi-equilibrium state of



illumination, at lower wavelengths (< 450 nm), the intra layer excitation T_2 , dominates the excitonic dissociation in GaS layer producing electron hole-pairs that are separated by the built-in potential in the heterojunction, causing electron and hole transit towards the source and drain contacts respectively. As the excitation wavelength transitions toward higher wavelength, contribution of excitonic transitions from WSe₂ with intralayer excitation T_1 aids to the photocurrent generation with highest responsivity observed at 450 nm and maximum open circuit voltage before saturation (discussed later). At illumination wavelengths below the bandgap of GaS (i.e. $\lambda >$ 490 nm), intra layer excitation T_1 path dominates excitonic transitions and the responsivity of the device starts to decay. As the illumination reaches beyond bandgap of ultra-thinWSe₂, ($\lambda >$ 850 nm), interlayer excitonic transition T_3 contributes mostly to the charge transport and excitonic dissociation, which is also evident from the difference in response between 810 nm, 980 nm and 1064 nm illumination (discussed later).

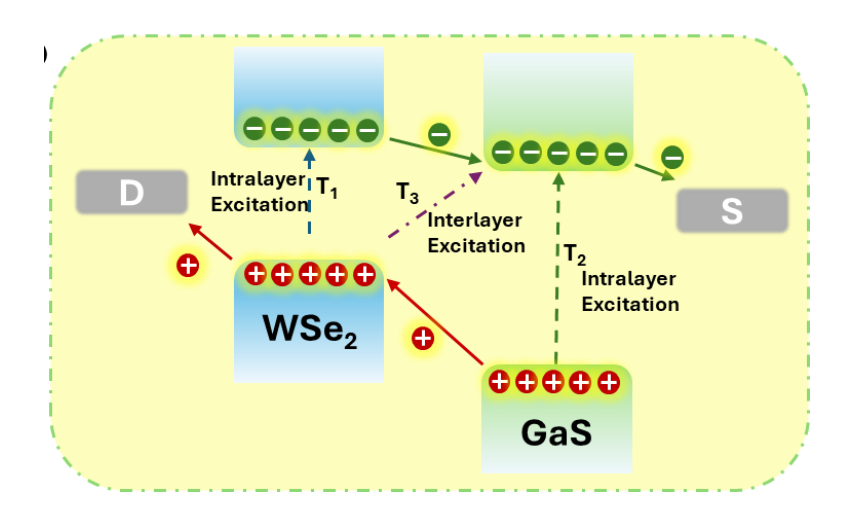


Figure 25. Pseudo band alignment of the heterojunction under quasi-equilibrium state of illumination, illustrating intralayer transitions $(T_1 \text{ and } T_2)$ and interlayer transition (T_3) .

3.2.8. Employment of synergistic device optimization strategies:

Role of the thickness of GaS and WSe2 in synergistic optimization:

We subsequently examine the significance of the optimized thickness of the GaS and WSe₂ layers in our investigated devices. In our investigation of multilayered GaS on h-BN, Ag/Au



vdW contacts demonstrated least deviation from linearity in the low bias regime (±500 mV) for a thickness above 8-10 nm as outlined in figure 26a and 26b. Any thickness lower than the mentioned value would significantly deviate the linearity, signifying the emergence of a Schottky barrier as outlined in figure 26c. A plausible explanation of this trend could be explained as thickness decreases, bandgap starts widening with decrease in free-carrier concentration and available density of states and fermi-level, shifting the conduction band edge to lower energy values, away from the fermi-level of the contact as outlined in figure 26d.

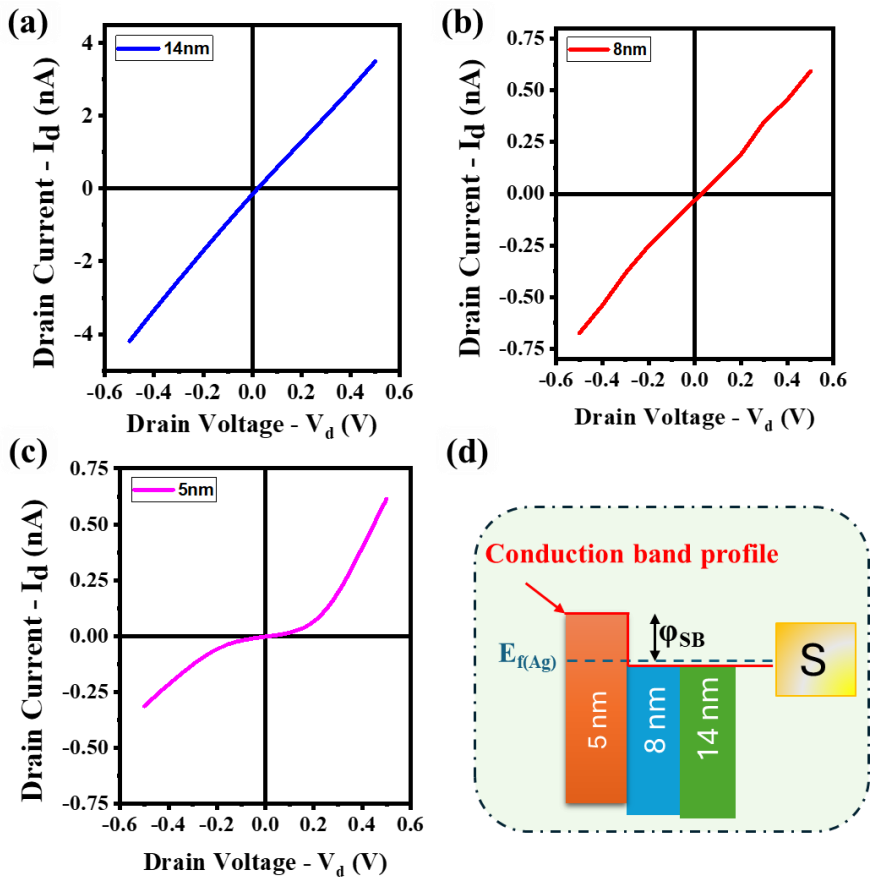


Figure 26. Evolution of layer dependent transition in contact type for GaS-vdW Ag on h-BN. (a) ohmic-14nm (b) ohmic-8nm (c) schottky-5nm. (d) Estimation of shift in Schottky barrier with decreasing thickness, due to shifts in fermi-level and conduction band edges.

Additionally, the thickness of the WSe₂ layer plays a crucial role in determining the robustness of the p-n junction. Earlier, it was reported that a thicker WSe₂ would shift the work function to lower energy levels, promoting an n-type transition [17], supporting our KPFM findings as well. Figure 27 illustrates the changes in the Fermi level of WSe₂ with respect to gold (Au) as



a reference, across varying thicknesses. Specifically, figure 27a presents an optical micrograph, while figures 27b and 27c display corresponding atomic force microscopy (AFM) and Kelvin probe force microscopy (KPFM) images, respectively. As indicated in figure 27d, a variation in the thickness of the WSe₂ flake from approximately 10 nm to 15 nm results in a measured surface potential difference (SPD) of approximately 15 mV. This observation suggests a reduction in the work function of WSe₂, leading to a shift in the Fermi level toward lower energy values, which indicates an emergence of n-type doping as the thickness increases. Therefore, to establish a robust heterojunction with p-type WSe₂, it is essential to optimize the thickness at lower values. Moreover, our abovementioned argument could further explain the reason for reduced performance, in device-2, which comprised of a thicker WSe2 region and the optoelectronic characteristics and KPFM results suggested that the built-in potential developed in junction region may have degraded as the SPD obtained was 125 mV, significantly lower than the SPD of device-1, undermining its optoelectronic performance (more discussion later). This may be one of the probable factors. Additionally, another contributing factor could be that the optimized thickness of WSe₂ layer (3nm) may play an important role in charge carrier separation and extraction. It is well established that monolayer TMDC shows an absorption of only 5% of the incident illumination. With increase in the thickness of WSe₂ to a few layers, the absorption should increase and should promote higher photocarrier generation. However, a scaling limit is reached due to a trade-off between photocarrier generation in multiple layers and its separation and extraction, due to intra layer recombination dominating over the extraction and separation mechanism, which could be another reason for reduced efficiency as outlined in figure 27e.



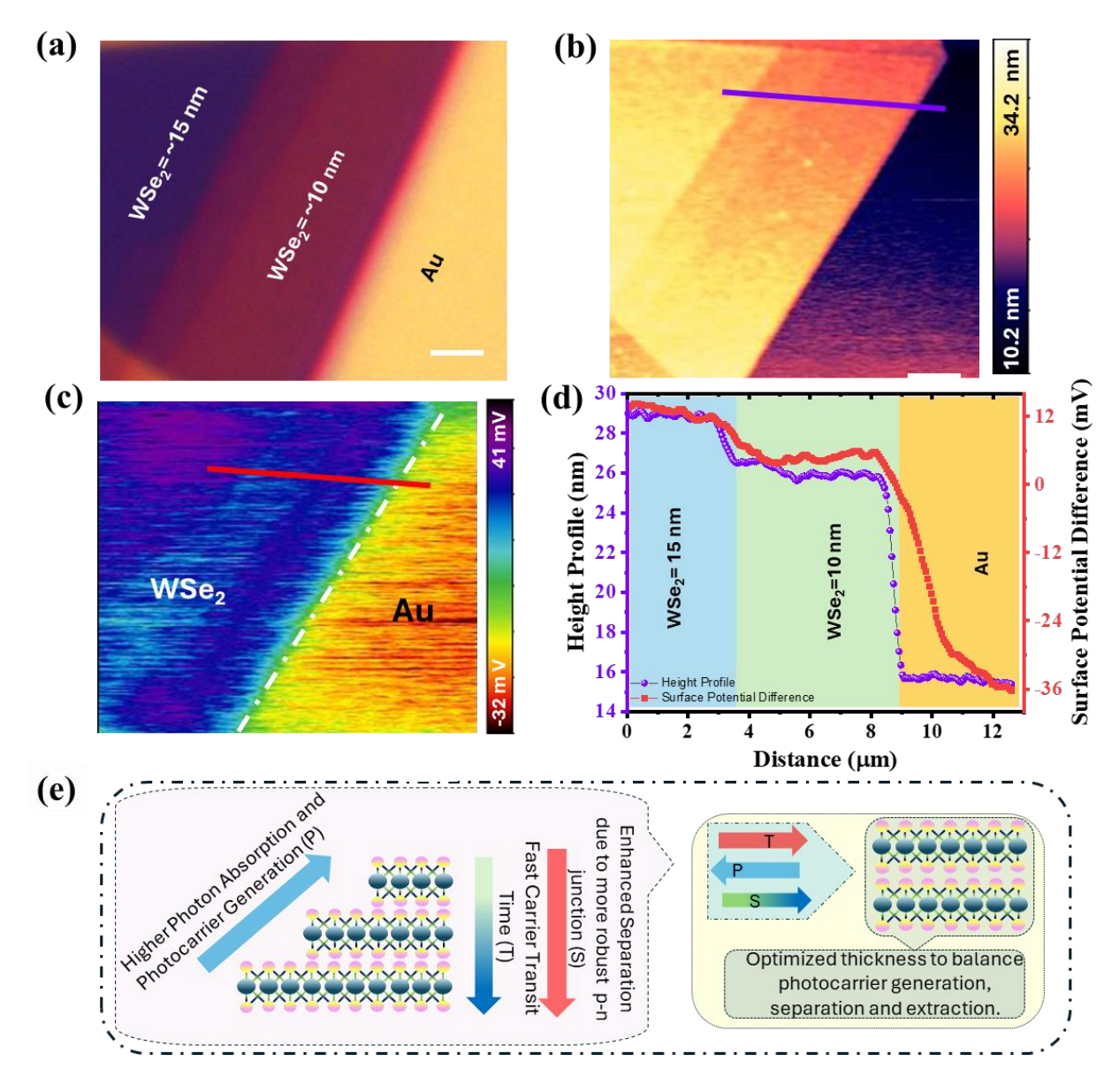


Figure 27. Modulation of WSe₂ fermi-level, with thickness. (a) Optical micrograph of a step height varying WSe₂ flake of 15nm. Corresponding (b) AFM image used for height profile. & (c) KPFM image for surface potential difference. (d) Height profile and surface potential difference variation in the flake. (e) Strategy for optimization of WSe₂ layers for efficient charge generation, separation and extraction.

Furthermore, a device with thicker GaS (~13.2nm) and ultra-thin WSe₂ of 3.8nm (device-3) was also investigated and was found to have lower power conversion efficiency (PCE) than device-1, despite having a larger SPD than device-1 (more comparative discussion presented later), indicating poor charge separation and extraction characteristics as well. The measured



SPD from KPFM was higher (~216 mV) likely due to a thicker GaS region with ultra-thin WSe₂, similar to device-1, suggesting a robust p-n junction. However, observation of lower PCE could be explained using figures 28a and b. As illustrated, when the GaS thickness (t₁) as in device-1 (figure 28a), is lower than that of (t₂) as in device-3 (figure 28b), the contact region for charge carrier extraction is positioned closer to the depletion region of the junction in the vertical direction. Consequently, the carrier transit path (L₁) in device-1 is shorter than the transit path (L₂) in the thicker GaS region of device-3. This configuration significantly reduces the photocarrier recombination likelihood and enhances carrier extraction efficiency in device-1, which demonstrates a PCE of 0.8%, compared to the 0.4% PCE observed in device-3 with the thicker GaS region at 405 nm (more comparative analysis presented later).

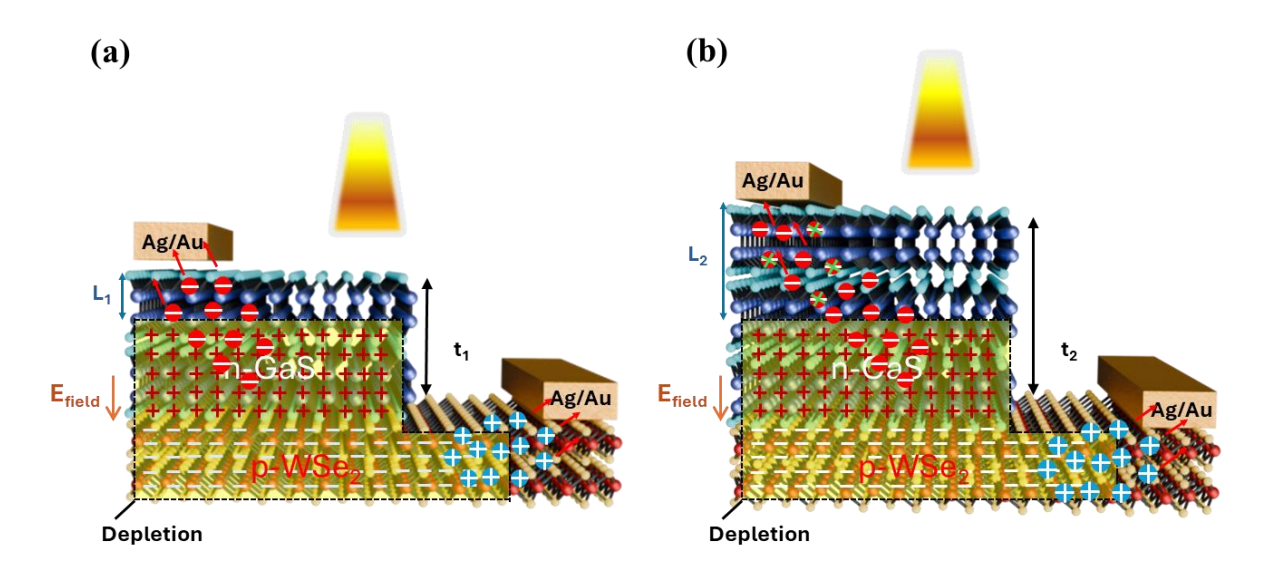


Figure 28. Carrier extraction pathway for GaS layers with thickness (a) t_1 (device-1) and (f) t_2 (device-2), where $t_2 > t_1$.

Role of Fermi-level-pinning and its perceived effects in vdW junction photodiodes:

For high performance device operation of vdW optoelectronics, it is generally expected that metal-vdW-m junction is free of Schottky-barrier and forms ohmic contact, that sponsors ultralow contact resistance. The emergence of Schottky-barrier in metal-vdW-m junction is strongly correlated to the metal-vdW-m interfacial interactions that trigger FPL, similar to the



case observed in metal-3D semiconductor FLP characteristics, despite having near perfect surface states, due to absence of surface dangling bonds. The origin of FLP in metal-vdW-m interface has been thoroughly investigated [57,119,120] and the cause has been identified to be from the formation of large number of defect states that occur when metal is directly deposited on the surface of the vdW-m.

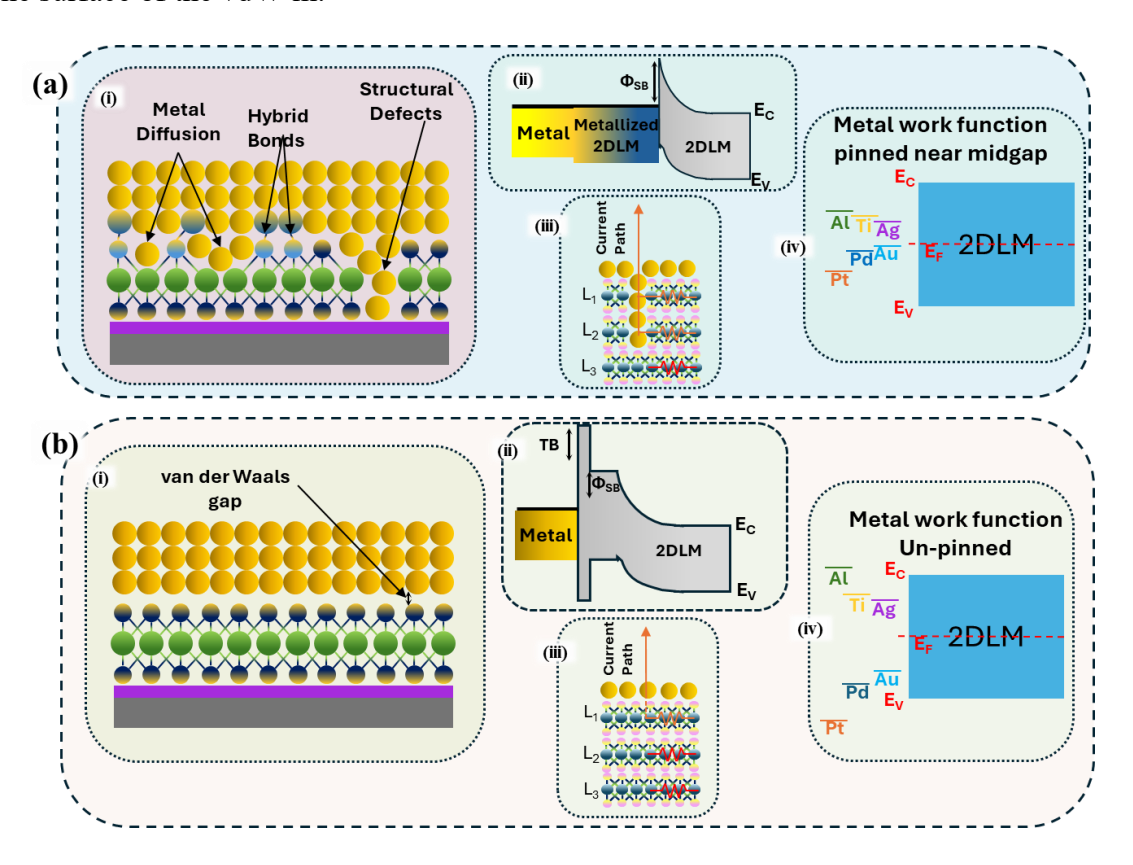


Figure 29. (a) Metalized 2DLM and Fermi level pinning (FLP). (b) Van der Waals contact, free of FLP, metallized 2DLM and efficient contact engineering.

In figure 29 a, a typical scenario involving deposited metal is depicted. It illustrates that metal diffusion into two-dimensional layered materials (2DLM) results in three primary issues: structural defects within the 2DLM, the formation of hybrid bonds between the metal and the 2DLM, and the diffusion of metal into the 2DLM (see figure 29a-i). These phenomena significantly impact the performance of vdW optoelectronic devices. The structural defects act as hotspots for the capture and injection of thermalized carriers, leading to a degradation of both mobility and dark current characteristics. Furthermore, the presence of hybrid bonds and



diffused metals adversely affects dark current performance due to the formation of a metallized region within the 2DLM, effectively eliminating the vdW gap (refer to figure 29a-ii) and a large Schottky barrier is created (Φ_{SB}). Moreover, the dark current of the device is affected in two ways; (i) the dark current is significantly increased due to injection of thermalized carriers from the midgap states and (ii), the formation of hybrid bonds between the metal and vdW-m leads to loss of vdW gap between the metal-vdW-m junction, further escalating the flow of dark current. The effect is more pronounced for few layer vdW-m when the metal pierce through the top layer and create bonds with the subsequent layers underneath as well, reducing the effective resistance for dark current path as shown in figure 29a-iii. Ultimately, it is important to note that the Fermi level of the metal is consistently pinned at the mid-gap states. Consequently, employing metals with varying work functions to adjust the Schottky barrier frequently proves ineffective, and this diminishes the prospect of achieving ohmic contact, despite using metals with matching work functions, as the metal work function is pinned to the mid-gap states of the vdW-m as shown in figure 29a-iv. This is very significant for a vdW-m with a considerably large bandgap like GaS, for which self-powered optoelectronic devices may not have been possible till date. Additionally, the defect-induced gap states are also hotspots for scattering, recombination and trapping of photogenerated carriers. This negatively impacts key FoM of photodetectors, especially reduced efficiency, linear dynamic range, power exponent, sluggish response times, etc. and the overall performance of the photodetector is greatly reduced.

On the contrary, using a vdW transfer metal contact, here after referred to as vdW metal contacts (vdW-MC) significantly reduces FLP [57], can help in efficient alignment of work function-based metal-Schottky barrier engineering for efficient photocarrier extraction, pristine metal-vdW-m interface eliminating the gap state induced scattering, recombination and trapping of photocarriers, enhancing the overall performance of the detectors. As outlined in figure 29b, the scenario of a vdW-MC is illustrated. This configuration preserves the vdW gap



between the metal and the vdW-m, ensuring the absence of structural defects at the metal-vdW-m interface and preventing any penetration into the underlying 2DLM (see figure 29b-i). In this arrangement, a tunable Schottky barrier (Φ_{SB}) is observable, preceded by a tunnel barrier (TB) prior to the metal-vdW-m interface (illustrated in figure 29b-ii). The dark current path resistance is significantly increased due to the presence of the tunnel barrier, with the underlying vdW-m contributing substantially to the overall dark current path resistance (as shown in figure 29b-iii). Furthermore, the alignment of the Schottky barrier can be optimized through the careful selection of metal work functions, allowing for the formation of either Schottky or ohmic contacts (depicted in figure 29b-iv). Overall, the implementation of vdW-MC contacts not only alleviates issues related to dark current but also enhances the photoelectric performance of photodiodes by minimizing trap states and facilitating efficient charge carrier extraction.

Role of the optimized structure in charge carrier extraction:

We looked at the role of the structure of the device in enhancing the device's performance. Previous reports of GaS based photodetector structures [111,115–117] employed a lateral configuration. Since GaS has a large bandgap of \sim 2.5 eV, it is expected to have low charge carrier mobility due to reduced free charge carrier concentration. Hence a lateral heterojunction with an extended GaS layer before the contact, would introduce unnecessary increment in the charge transport path. In the comparison of GaS and WSe₂, it is observed that GaS possesses a bandgap that is almost twice that of WSe₂ [1.3 eV -1.5 eV]. As a result, the resistance of any extended GaS channel, denoted as R₂, is significantly greater than the resistance of an extended WSe₂ channel, R₁, when both channels are of similar length, as illustrated in figures 30a and b. This disparity in resistance leads to reduced charge carrier mobility in GaS compared to WSe₂. Assuming that both devices have the same active area and similar flake thicknesses, any extended GaS channel prior to the contact region is likely to experience enhanced photocarrier



recombination relative to the WSe₂ channel. Consequently, the device structure depicted in figure 30a—which represents a diode D₁ formed at the hetero-interface between GaS and WSe₂ exhibits superior performance compared to the structure shown in figure 30b, which includes the extended GaS channel with an additional resistance R₂.

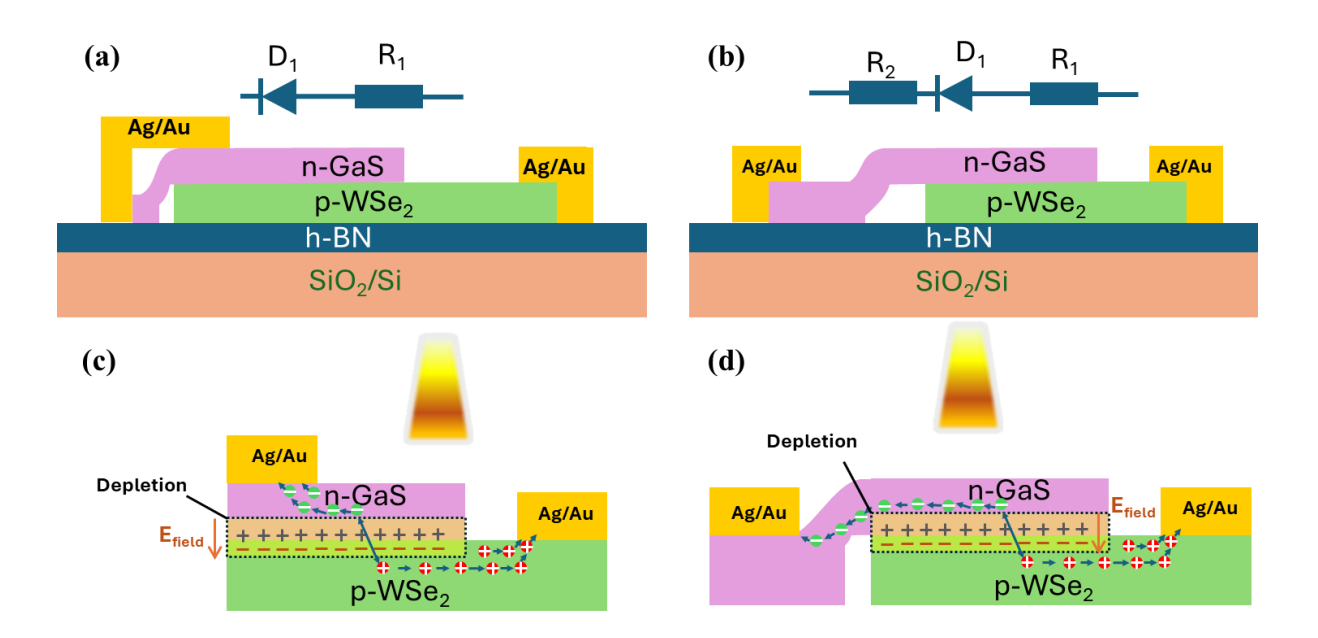


Figure 30. (a) Schematic of a semi-vertical GaS-WSe₂ heterojunction. (b) Schematic of a lateral extended channel GaS-WSe₂ heterojunction. (c) Transport path of photo carrier in a semi-vertical heterojunction (d)Transport path of photo carrier a lateral extended channel GaS-WSe₂ heterojunction.

In the scenario presented in figure 30a, the electron transit length is in the nanometre range, dependent on the number of layers, particularly near the source contact, resulting in significantly reduced transit time, as illustrated in figure 30c. Conversely, in the case depicted in figure 30d, under identical photocarrier generation rates, electrons are required to traverse distances on the order of several micrometres, as opposed to merely nanometres in the device shown in figure 30c. This increased transit distance raises the likelihood of photocarrier recombination prior to collection at the contact terminal, thereby diminishing the overall photoconversion efficiency and sluggish response.



Overall, a synergistically optimized effect of efficient charge carrier generation, separation and extraction takes place in this optimized heterojunction based on the precisely adjusted thickness of GaS-WSe₂, integration of vdW-MC along with the device structure.

3.2.9. Optoelectronic characteristics of the Synergistically engineered a-vdW photodiode:

A robust heterojunction photodiode showing fast response and broadband characteristics should be a synergistically engineered device so that it balances maximum photocarrier generation, enhances the charge separation and provides an efficient route for charge carrier extraction, under illuminated conditions. Figure 31a represents the output curve of the device with increasing light power P_{in} from 0.067pW to 14.44nW at 450 nm illumination. As the light power increases, a significant increase in the short circuit current (I_{SC}) and open circuit voltage (V_{OC}) is observed, which can be further substantiated from the zoomed linear scale plot of I_d - V_d in figure 31b, clearly stating the crossover at the respective axis. The photovoltaic effect of our optimized heterojunction was assessed using the measurements of I_{SC} and V_{OC}, (figure 31c). V_{OC} shows a linear scaling dependence with the log of the input power density (PD_{in}), with gradual evident saturation as PD_{in} reaches ~50mW/cm², with a maximum V_{OC} of 0.36V. The photocurrent (I_{ph}) of the detector is defined as the difference between drain current under illumination and dark condition ($I_{ph}=I_{light}-I_{dark}$). In the case of our a-vdW photovoltaic detectors, where there is absence of source-drain bias, the dark current (I_{dark}) of our investigated devices were in the $\sim fA$ range, which is impressively low and the current under illumination (I_{light}) could be written as $I_{light} \approx I_{SC}$. Interestingly, the double log plot of I_{SC} vs PD_{in} , shows an impressive linearity, with no saturation observed in our investigated maximum PD_{in} (52.7mW/cm²), with an impressive power exponent, α (i.e. $I_{SC} \propto PD_{in}^{\alpha}$) of 0.96. The linear regime of the I_{SC} - PD_{in} , can be quantified by an important figure of merit, the linear dynamic range (LDR) of the photodiode, in dB, and could be obtained using the following equation:



$$LDR = 20log \binom{PD_{in(max)}}{PD_{in(min)}}$$
 (10)

where, $PD_{in(max)}[PD_{in(min)}]$ is the maximum [minimum] PD_{in} of the linear region. Based on the reported results in figure 31c, the LDR of our optimized junction is 106.7dB. It is worth noting that 106.7 dB is still underestimated due to the limited illumination conditions available at our disposal. Our reported Voc of 0.36V, LDR of 106.7dB and ultra-low dark currents of $\sim fA$ in this work is amongst the most impressive ones in single vdW heterojunctions and even exceeds that of more recently investigated double heterojunctions under similar illumination conditions [83]. This suggests GaS-WSe₂ vdW heterojunction for similar applications would be an excellent alternative.

Owing to the impressive power exponent value of 0.96 and a large V_{OC} of 0.36, we further investigate the ongoing photocarrier generation and recombination mechanisms in our synergistically engineered heterojunction photodiode. For vdW interfaces, two primary physical phenomena are involved in the interlayer recombination mechanisms[21][136]:

- Shockley-Read-Hall (SRH) Recombination: This process is driven by the inelastic tunneling of majority carriers into trap states, often referred to as monomolecular recombination.
- 2) Langevin Recombination: This occurs due to Coulomb interactions, where electronhole pairs recombine at the junction shortly after their creation, also known as bimolecular recombination.

In the heterojunction region, one of these mechanisms may dominate, although both can occur simultaneously. To quantitatively elucidate the recombination process, the following equation can be used [137]:

$$\frac{dV_{OC}}{dln(PD_{in})} = \frac{2}{\beta} \cdot \frac{K_B T}{q}$$
 (11)



where, β represents the recombination order (1:-SRH recombination & 2:-Langevin recombination). K_B is Boltzmann's constant, T is the temperature and q is the unit charge. From the fitting of the experimental data, we obtain β to be 1.84, suggesting the synergistic optimized device is dominated by Langevin recombination. This is very significant as upon synergistic engineering, the device tends to suppress/reduce trap mediated recombination, when compared to device-2 and device-3, with more discussion presented later. The reason could be further related to the thickness of the optimized layers of both GaS and WSe₂ for robust p-n junction, shorter carrier transit path for GaS layer to reduce trap assisted recombination, ultimately benefiting the device for efficient charge separation and extraction.

Additionally, we also investigated the electrical power production from the diode (P_{el}/I_{ds} . V_{ds}) with a maximum power produced as 0.162nW (figure 31d). The calculated power conversion efficiency (PCE) using the maximum electrical power $P_{el_{max}}$ using the following equation:

$$PCE = P_{el_{max}}/P_{in} (12)$$

for the same P_{in} , is represented in figure 31d. With increase in P_{in} , the PCE also increases to a maximum value of 1.52%, before slight reduction at maximum investigated P_{in} of 14.44nW, demonstrating a gradual saturation of its capacity of energy conversion and light harvesting at the p-n junction, likely due to the saturation of the photovoltage developed at the junction. Our reported PCE in this work is significantly larger than WSe₂-Bi₂O₂Se heterojunction (0.428%) [84] in the similar thickness regime.



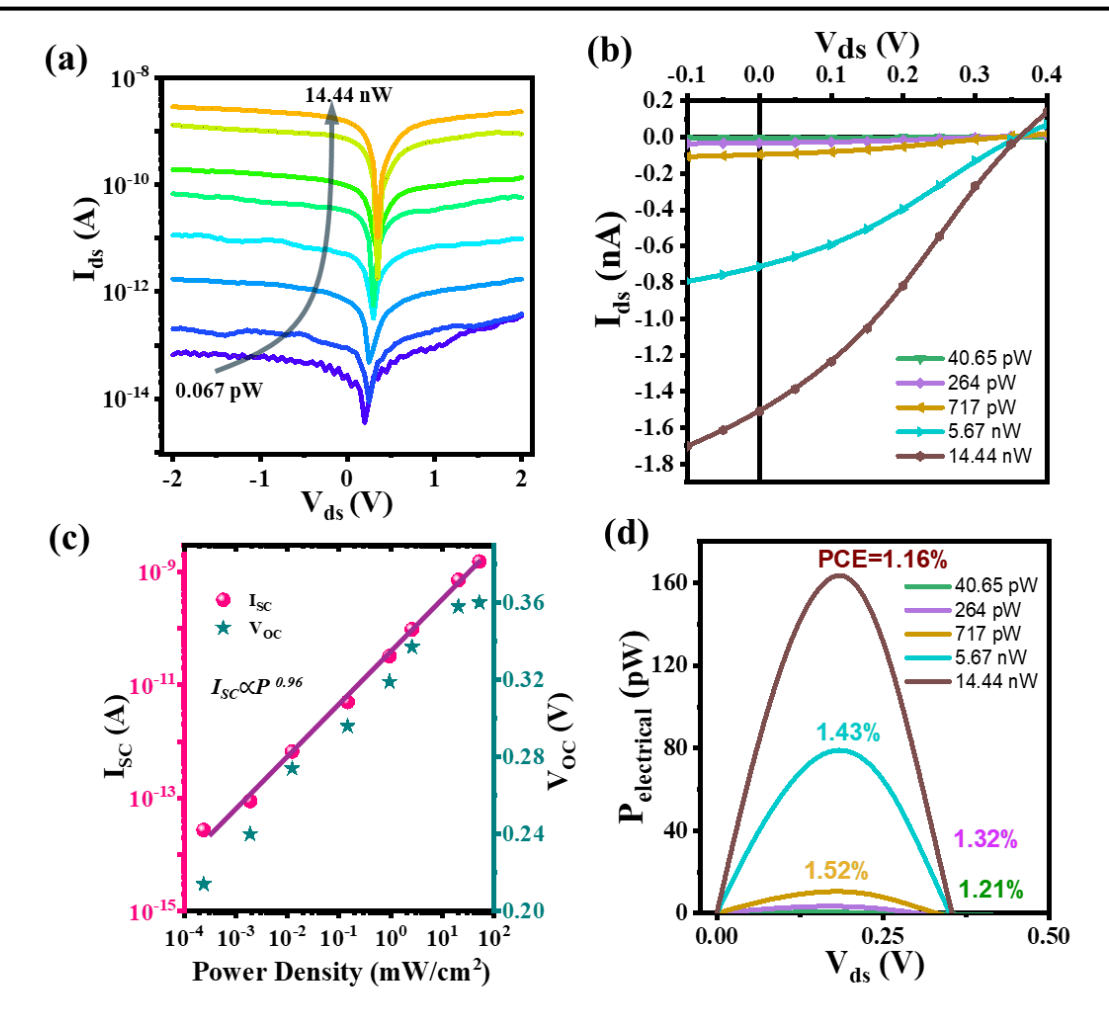


Figure 31. Optoelectronic characteristics of the device under 450nm illumination. (a) Evolution of $log\ I_d$ - V_d characteristics under increased illumination power. (b) Zoomed region of I_d - V_d showing clear I_{SC} and V_{OC} . (c) I_{SC} and V_{OC} vs power density plot showing a linear region for I_{SC} and no saturation with a LDR of 106.7 dB and V_{OC} saturation at 0.36 V. (d) Electrical power characteristics of the photodiode under increased illumination showing various PCE under varied illumination conditions.

The photovoltaic responsivity (R) of the device was obtained using the ratio of the photocurrent to the input optical power (i.e. $R = I_{ph}/P_{in}$). As represented in figure 32a, a maximum photovoltaic responsivity of 376.76mA/W was obtained, comparable to single junction InSe-Gr a-vdW device [138] and larger than recently investigated PdSe₂-MoTe₂ heterojunctions [139]. Along with responsivity, external quantum efficiency (EQE) is an important bench marking parameter for photovoltaic type devices and could be estimated based on the responsivity of the device and illumination wavelength, using the following equation.



$$EQE = R. h. c/e. \lambda \tag{13}$$

where h, c, e and λ represents Planck's constant, speed of light, unit charge and wavelength of illumination respectively. The estimated EQE of the photodiode at various wavelengths under self-biased condition is illustrated in figure 32b. The device shows an excellent EQE evolution, maintaining a value of $\sim 30\%$ at high illumination intensity in the 400-450nm region, suggesting excellent photovoltaic performance for solar cell applications as well [140]. Moreover, for competitive performance comparison, the fill factor (FF) of our device was also obtained. FF is a measure of solar cell quality, indicating how closely the actual maximum output power follows the theoretical maximum value for the device and could be obtained as:

$$FF = P_{el_{max}}/I_{SC}.V_{OC}$$
 (14)

The polychromatic FF of our device has been presented in figure 32c with varied illumination intensity. Our device exhibits an excellent value of FF within 0.28 to 0.35 even at higher power density, suggesting the device is indeed a contender for power harvesting in the solar spectrum region, and potentially contribute to harvesting the 4% UV solar irradiance, which is otherwise overlooked in conventional silicon solar cells.

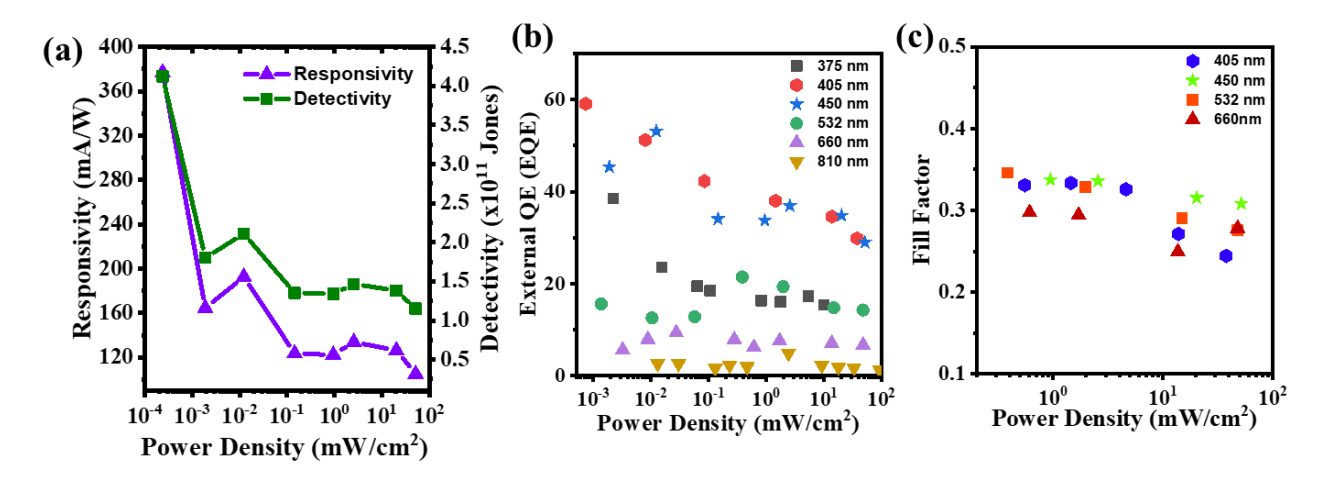


Figure 32. (a) Responsivity and detectivity vs power density of the device at 450nm illumination, showing a peak photovoltaic responsivity of 376.76 mA/W and detectivity of 4.12×10^{11} Jones. (b) EQE at various wavelengths and power densities (c) Fill factor of the device under visible solar spectrum region with varying power density.



Another important figure of merit for photodetectors is the specific detectivity, D* of the device, which can be derived from noise equivalent power (NEP) of the photodetector using the following equation:

$$D^* = \frac{\sqrt{A}}{NEP} \tag{15}$$

where A is the device active area. The inference of noise currents in photodetectors could be made from the summation of Johnson noise, Shot noise and Flicker noise. The shot noise current (i_{SN}) in a photodiode could be estimated from the following equation using the dark current $i_{SN} = \sqrt{2. q. I_{dark}}$, where I_{dark} represents the dark current of the device. Additionally, the flicker noise current could be extracted from the I/f fitting at the low frequency region of the noise power density plot. An estimation of the D^* could be readily obtained from the following equation:

$$D^* = \frac{\left(R_{\lambda}. A^{\frac{1}{2}}\right)}{(2. q. I_{dark})^{\frac{1}{2}}}$$
 (16)

where, R_{λ} is the wavelength specific responsivity and q is the unit electron charge. The maximum estimated detectivity from the abovementioned equation at 450 nm illumination could be obtained as 7.32×10^{12} Jones. However, the above-mentioned estimation is valid when the dominant noise factor in the device is the shot noise and is a crucial aspect at high frequencies and could be overestimated by several orders of magnitude, compared to noise contribution from flicker noise at low frequencies. To further evaluate the discrepancies, we investigate the presence of flicker noise from the noise power density plot of our detector. Figure 33 represents the temporal evolution of dark current and the corresponding noise power density of the synergistic engineered. The dark current traces of the devices were obtained using Agilent B1500 semiconductor parameter analyzer at $V_{ds} = 0$ V at a sampling rate of 50 Hz for 5 seconds. Noise power density was obtained from the Fourier transform of the time



evolution of the dark current. A flicker noise sub log linear fit $(1/f)^{\alpha}$ could be interpreted for the device, suggesting low frequency flicker noise dominant characteristics. The measured noise currents (i_N) was within 10^{-16} AHz^{-1/2}, suggesting they can deliver ultra-low light detection performance. The noise current obtained from linear fitting of the noise density plot could be used for estimating the *NEP* using the equation:

$$NEP = \frac{i_{fN}}{R} \tag{17}$$

where i_{fN} , is the flicker noise current, and R is the responsivity the device. The obtained NEP is 1.28 fWHz^{-1/2}, which could be used to obtain maximum D^* of 4.12×10^{11} Jones as outlined figure 32a. This reveals that indeed estimation of a presence of dominant shot noise would lead to an underestimation of the detectivity of the device. Henceforth, we report the detectivity of our findings based on NEP.

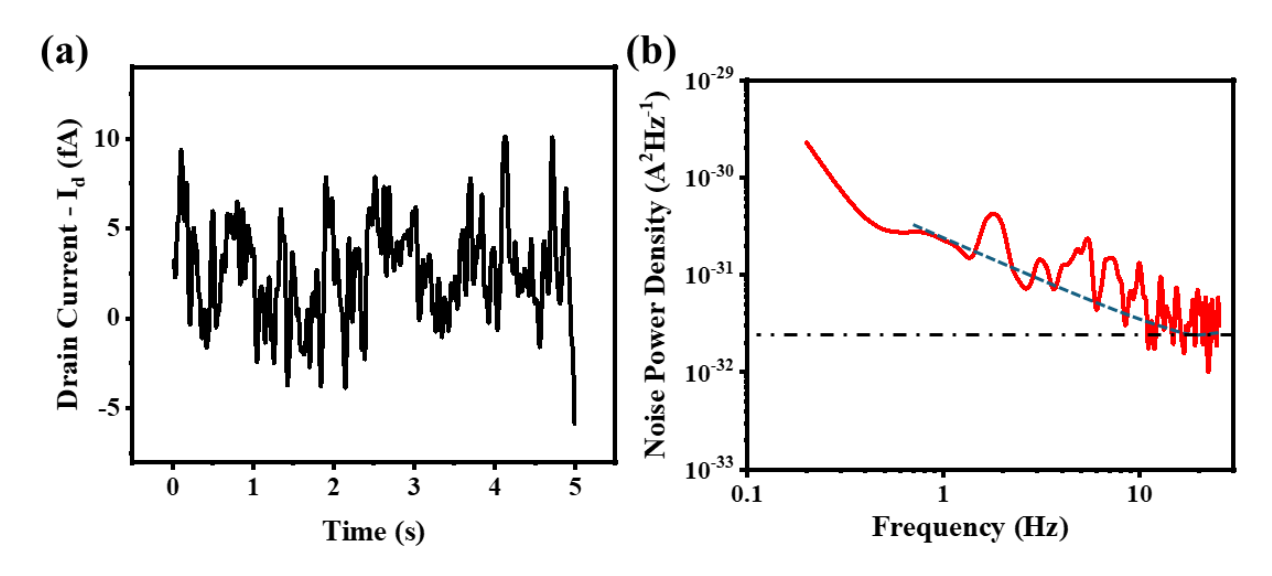


Figure 33. (a) Dark current trace of the synergistic-engineered photodiode at V_{ds} =0 V. (b) Noise Power Density plot of the device.

We next look into the temporal photocurrent response of the device. The photovoltaic response speed is an essential performance parameter for a self-powered photodetector, as it measures how promptly the device responds to rapidly changing incident light. This characteristic is particularly important for applications that demand quick detection and adaptation to



fluctuating light conditions. Owing to the presence of the strong built-in potential from the type-II heterojunction, the device is expected to have a fast response. Figure 34a represents the time resolved photocurrent of the device at 1 Hz - 405nm illumination, with 200 switching cycles. A stable photo-switching is observed over 200 cycles with no evident degradation in the device's photocurrent, suggesting a robust performance. Furthermore, to evaluate the stability of the device under ambient storage, time resolved photocurrent measurements were repeated over a period of 3 months as represented in figure 34b.

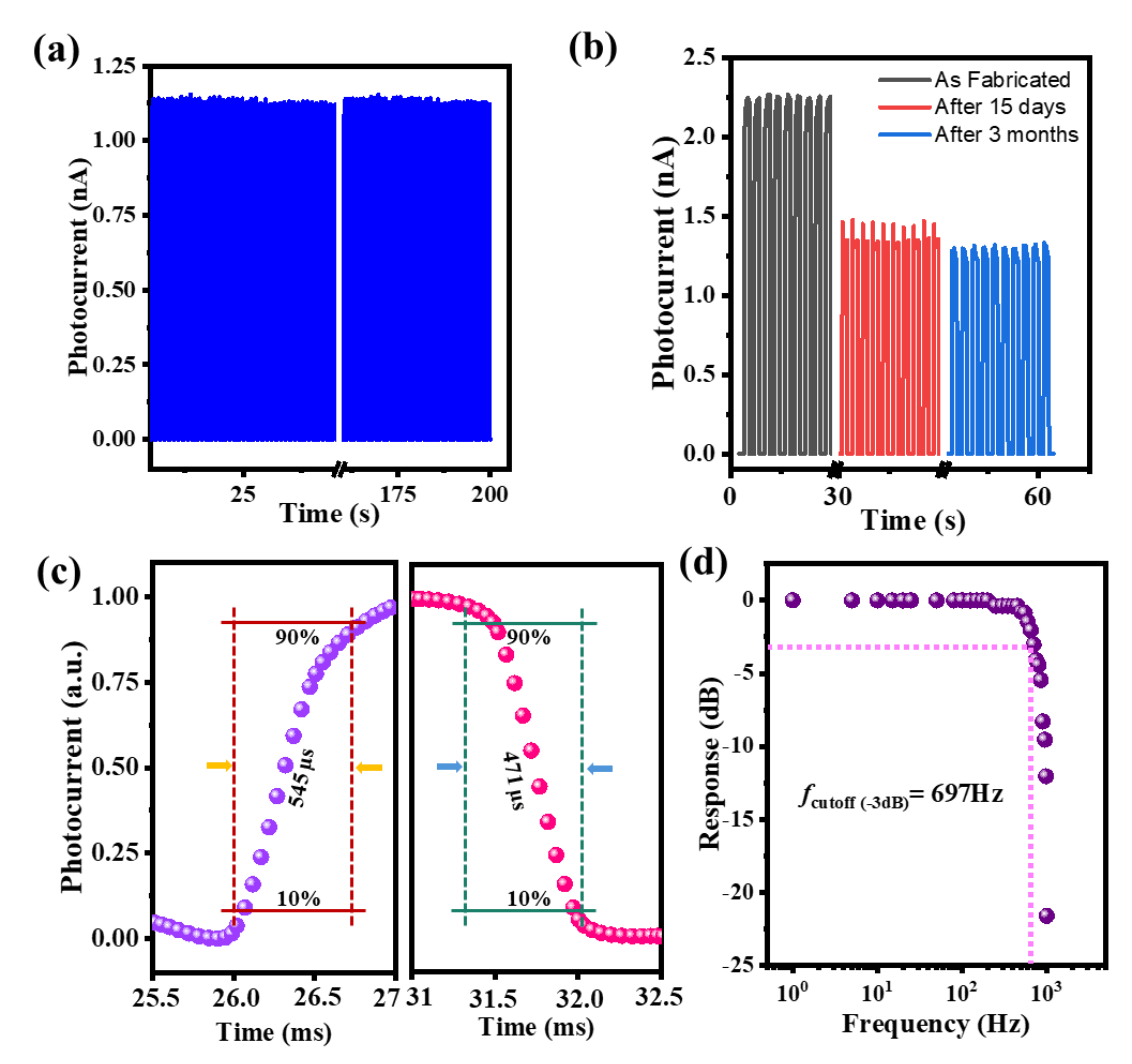


Figure 34. Temporal photocurrent response of the device at 405 nm illumination, showing (a) 200 cycles of switching stability with no degradation, (b) evolution of stability of the device under a course of 90 days observation period, (c) rise and fall time of the device showing 545 µs (rise) and 471 µs (fall) edges and (d) frequency response showing a cutoff (-3dB) at 697Hz.



We observed that the device performance exhibited variations shortly after fabrication and was monitored over the first three months. All optoelectronic characterizations presented here were conducted after a period of 20 days, once fluctuations in device performance had stabilized. Notable differences in performance were recorded between day 1 and day 15 during ambient storage. This variation could be attributed to a stabilization effect occurring in the contact region due to photo induced contact evolution where the metal interacts with the underlying vdW-m, as was reported for the case of Au-InSe contacts [141]. Additionally, diffusion of oxygen into the contact region may have contributed to some expected degradation in performance, akin to phenomena observed in MoS₂ field-effect transistors (FETs) with titanium contacts [142]. However, no significant changes were detected between the tests conducted on day 15 and day 90, suggesting that a saturation limit in performance may have been attained. The consistent and reproducible photo response after 200 switching cycles along with long term stability of the device demonstrates the exceptional reliability of the self-powered photodetector. The rise time and decay time of the device was obtained between 10% and 90% of the maximum I_{ph} , as illustrated in figure 34c, where a rise time (fall time) of 545µs (471µs) was observed, demonstrating superior response speeds compared to MLG/ReSe₂/SnSe₂ (752 μs/ 928 μs) [133] and PdSe₂-MoTe₂ (3.5 ms/3.7 ms) [139] heterojunction-based devices. Additionally, a series of measurements conducted at multiple laser modulation frequencies (figure 34d) display that the 3 dB bandwidth (f_{3dB}) of the optimized photodiode is 697Hz, which is in good agreement with the measured photo response time. These results indicate the proposed device's capacity to monitor rapid optical signals and its great potential for high-speed photodetection.

Furthermore, we also investigated the on/off ratio of the device under various wavelengths at maximum illumination intensity at our disposal, as illustrated in figure 35a, in a self-powered configuration. The device demonstrated an excellent broadband photovoltaic response ranging



from 275 nm to 1064 nm, achieving a peak on/off ratio of ~10⁵ from 405 nm to 660 nm, comparable to WSe₂-Bi₂O₂Se [84] and Bi₂O₂Se/In₂S₃ [134] heterojunctions. Additionally, interlayer transitions were evident from the weaker temporal responses, with an on/off ratio of 10² observed for 940 nm and 1064 nm illumination. The wavelength dependent peak responsivity and detectivity of the device is illustrated in figure 3b, highlighting its exemplary photovoltaic performance. It is important to note that the detection bandwidth was limited by the available light sources during this investigation and may not represent the maximum bandwidth-limited response of the device.

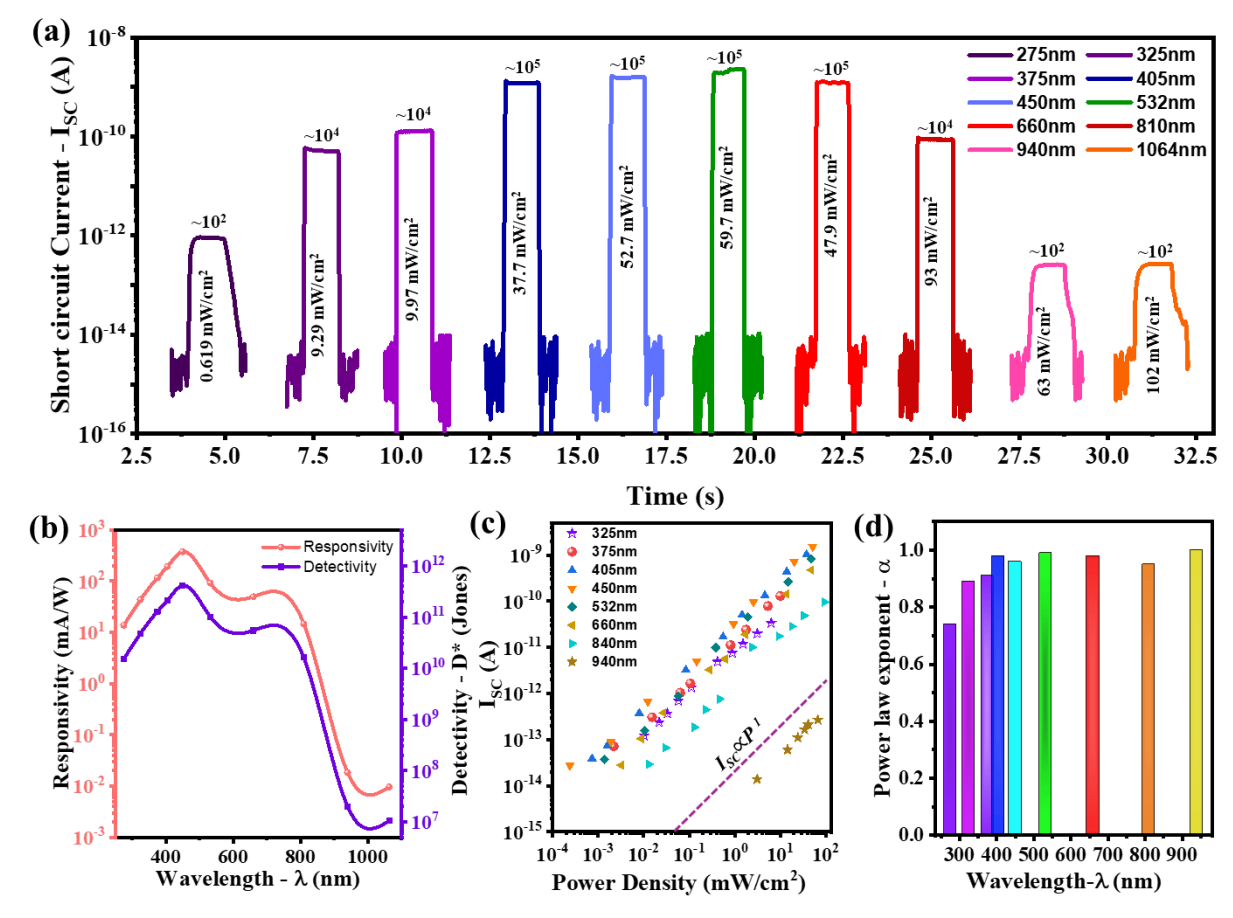


Figure 35. (a) Photovoltaic temporal response of the device under maximum available illumination conditions of the device under various wavelengths. The device shows a photovoltaic response between 275nm and 1064nm, with peak on-of ratio of 10^5 . (b) responsivity and detectivity of the device at various investigated wavelengths. (c) I_{SC} -PD_{in} for various wavelengths of investigation. (d) evolution of power law exponent (a), at various wavelengths.



We also examined the wavelength-dependent transition of the power exponent, α , as depicted in figure 35c. In conventional photodiodes, the power function α , derived from the double logarithmic plot of I_{SC} - PD_{in} serves as a measure of the device's charge extraction performance figure of merit, with a theoretical maximum value of 1. However, in practical applications, the value of α typically falls below 1, indicating the presence of recombination processes occurring in trap states [143]. This reduction in α reflects the inefficiencies in charge extraction due to these recombination pathways, which can adversely affect the overall performance of the photodiode. Notably, at lower wavelengths (<375 nm), α was less than 0.9. As the wavelength is increased to 405 nm, α increases to 0.98, maintaining values above 0.95 between 405 nm and 810 nm, and approaching near unity (0.99) at 940 nm (figure 35c and d). These findings suggest that some trapping and recombination occur at lower wavelengths, likely due to interaction with atmospheric absorbates which serves as charge trapping/detrapping centers under UV illumination [144], while negligible trapping is observed as the wavelength increases, indicating superior trapping/recombination-free performance in the near-infrared (NIR) region. The reported linearity in our device, across a wide range of wavelengths, is among the highest for single-junction photodiodes [136,139] and is comparable to recently reported dual floating junction detectors [82].

3.2.10. <u>Comparative performance analysis of the synergistic-</u> engineered photodiode:

In this section we will present a performance comparison analysis of the 3 a-vdW devices and the route to categorical analysis of the devices, based on power exponent (α), power conversion efficiency (PCE) and recombination order (β), to elect the most synergistically engineered photodiode. Additionally, we will explicitly look at the role of the FLP in an EBL patterned device and how significantly it impacts the device's performance. Figure 36 represents the characteristics of device-2 and figure 37 for device-3 a-vdW devices while figure 38, represents



the characteristics of the device-4 (EBL-patterned device). The performance analysis has been presented based on illumination under similar conditions at 405 nm wavelength. The dark current traces for the devices were also obtained and presented as well for comparative analysis purposes.

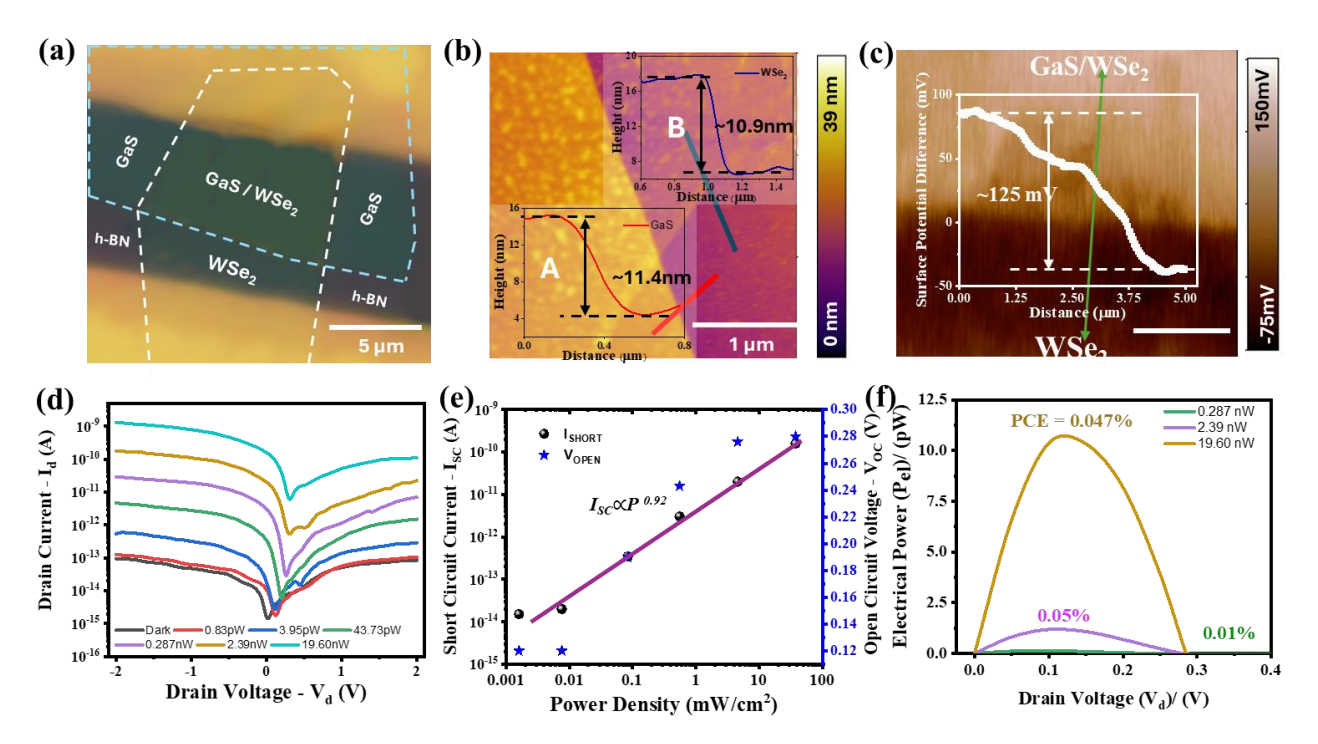


Figure 36. (a) Optical micrograph image (b) AFM image and height profile (c) KPFM image and height profile (d) I_d - V_d characteristics (e) double log plot of I_{SC} vs PD_{in} and (f) Optoelectronic power conversion characteristics of device-2 (All optoelectronic features were obtained at 405nm illumination wavelength).

Interestingly, all the investigated a-vdW devices (device-1, 2, and 3) exhibited a power exponent (α) greater than 0.9, with values of 0.98 for device-1, 0.92 for device-2, and 0.94 for device-3. In contrast, an electron beam lithography (EBL) patterned control device (device-4) demonstrated a significantly lower α of 0.55.



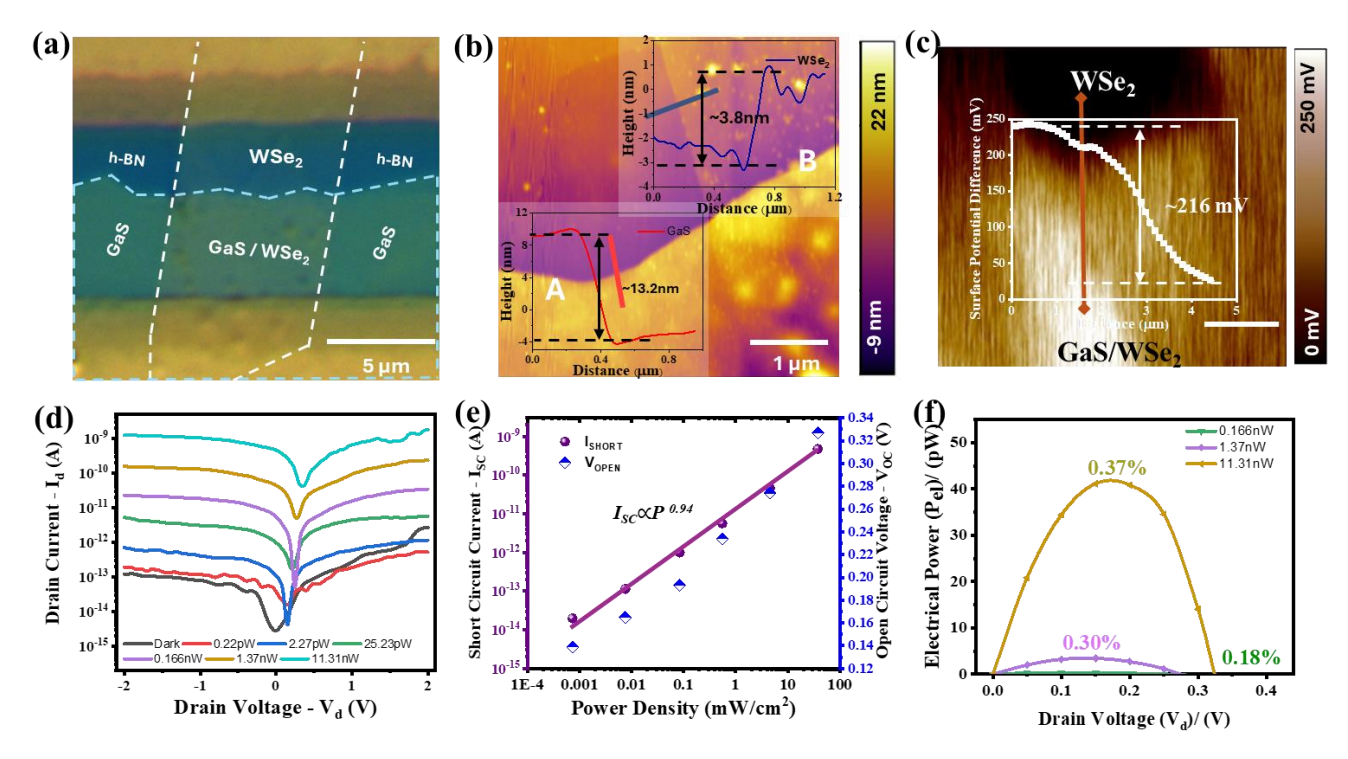


Figure 37. (a) Optical micrograph image (b) AFM image and height profile (c) KPFM image and height profile (d) I_d - V_d characteristics (e) double log plot of I_{SC} vs PD_{in} and (f) Optoelectronic power conversion characteristics of device-3. (All optoelectronic features were obtained at 405nm illumination wavelength).

Given that all devices were fabricated under identical conditions, have similar structure and active area, the inferior performance of device-4, patterned using traditional contact integration methods, suggests EBL patterned devices may have undergone significant interface modifications in the contact region, likely due to e-beam induced damages in the contact region and/or metal impingement induced trap states [121], inevitably making the device susceptible to increased FLP and charge trapping in the contact region. Additionally, device-4 presented no rectification and drain voltage induced conduction characteristics between the applied drain voltage of ± 2 V (figure 38d), under dark conditions, suggesting emergence of large back-to-back Schottky barrier at the contact regions. Additionally, power conversion is extremely poor as shown in figure 38f, likely due to competition between the built-in potential and the Schottky barrier.



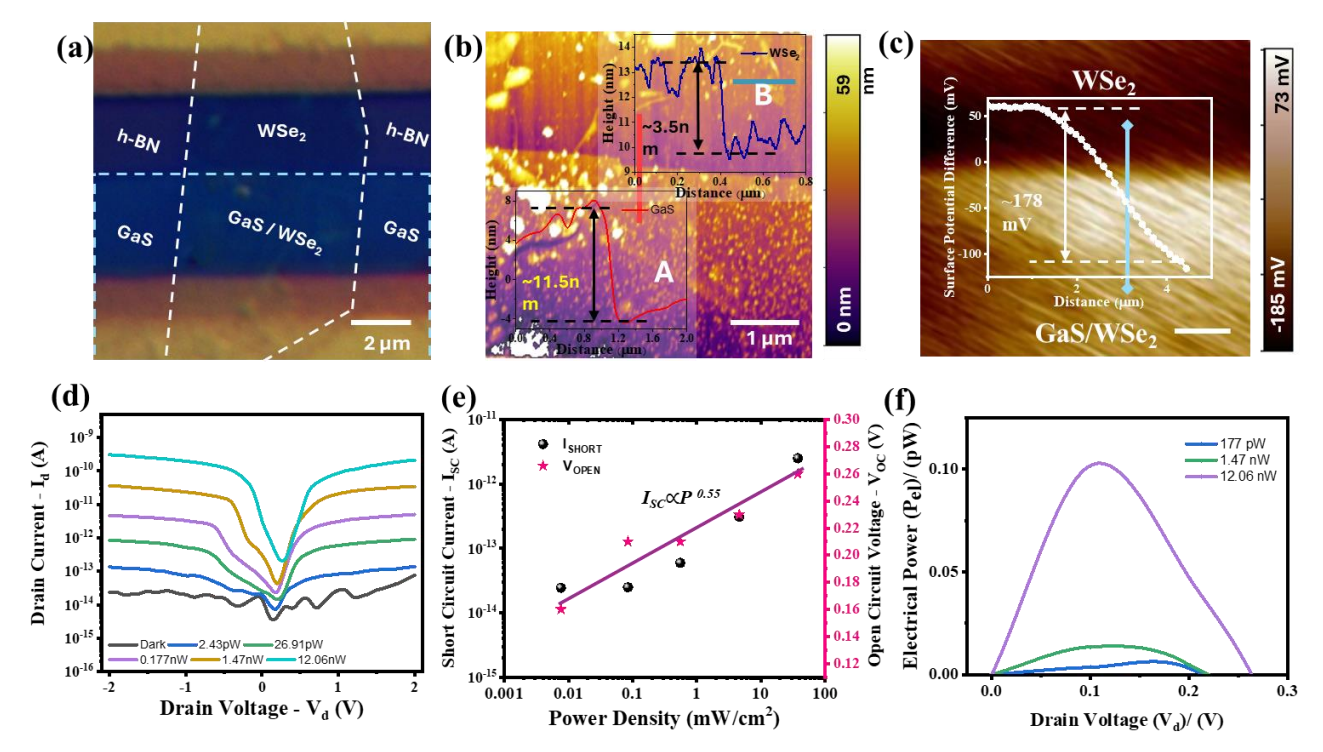


Figure 38. (a) Optical micrograph image (b) AFM image and height profile (c) KPFM image and height profile (d) I_d - V_d characteristics (e) double log plot of I_{SC} vs PD_{in} and (f) Optoelectronic power conversion characteristics of device-4.

The dark current traces and noise spectral density from device-3 and device-4 are presented in figure 39. The noise current traces were obtained using the same technique, under ambient conditions, as presented previously. Device-3 presented noise characteristics similar to device-1, having a noise current i_N of ~10⁻¹⁶ AHz^{-1/2}, with a similar persistent dark current characteristic.

The persistent dark current in the device-4 was an order of magnitude higher than all the avdW devices, suggesting injection of random thermalized carriers from the mid-gap states as stated earlier. Additionally, the noise current, i_N for device-4 was an order of magnitude higher than the a-vdW devices at $\sim 10^{-15}$ AHz^{-1/2}, which supports our claim as well. This finding is particularly relevant for GaS-based heterojunctions due to GaS's larger bandgap and more likeliness of being affected by FLP induced Schottky barrier and degrading performance, as evidenced.



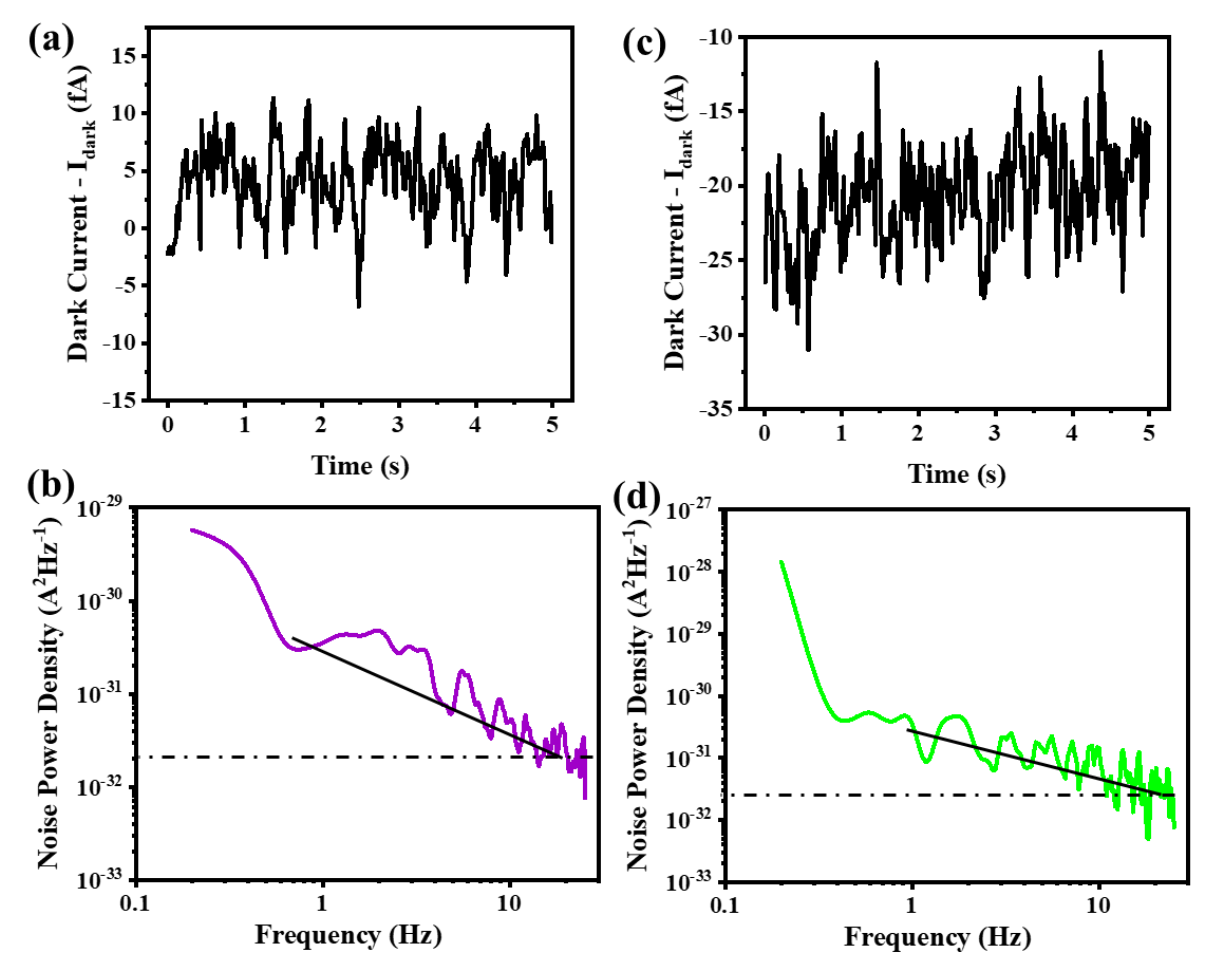


Figure 39. (a) Dark current trace of at $V_{ds}=0$ V. and (b) Noise Power Density plot of the device-3. (c) Dark current trace of at $V_{ds}=0$ V. and (d) Noise Power Density plot of the device-4.

Additionally, the lower values of α for devices-2 and 3 could be attributed to interlayer recombination centers, rather than contact-induced degradation and charge trapping, further emphasizing the need for a synergistic approach to thickness engineering for improved performance, as demonstrated by device-1. To substantiate our claim, we compare the recombination order value (β) for the three a-vdW devices at 405 nm, obtained using the equation 11. The results show that β for device-1 is 1.62, indicating dominant Langevin recombination. In contrast, device-2 and device-3 exhibited a β of 1.2, and 1.3 respectively, both suggesting dominant Shockley-Read-Hall (SRH) recombination occurring in trap states due to defects in the semiconductor. Moreover, analysis of the EQE of the devices presented in



table 2 further demonstrates that photocarrier extraction is best in device-1, while intermediary in device-3 and poor in device-2 among the a-vdW devices, while device-4 demonstrates the poorest among all 4 devices. This analysis reinforces our assertion regarding the necessity of a robust p-n heterojunction and thickness-optimized layers. Such optimization ensures that when photocarriers are generated, they are swept apart by the strong built-in potential before being trapped in defect states. Furthermore, our findings suggest that through meticulous optimization in vdW devices, we can achieve a scenario where dominant Langevin recombination persists. This may represent the ultimate performance limit in the proposed device structure due to low charge carrier mobility [145] of GaS, highlighting the performance limit of efficient charge extraction mechanisms observed in device-1.

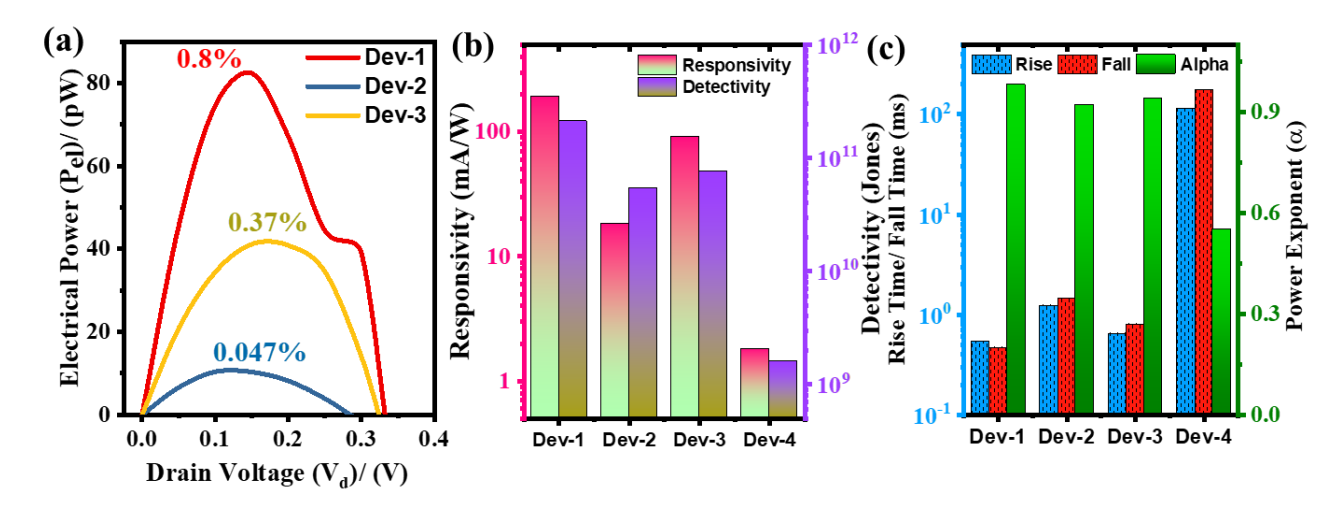


Figure 40. (a) Evolution of PCE of the fabricated a-vdW devices, suggesting the need for synergistic thickness engineering for efficient light harvesting characteristics, with a maximum PCE for synergistically optimized dev-1 and minimum for dev-2 having a thicker GaS and WSe₂ regions, with intermediate performance from dev-3, constructed from ultra-thin WSe₂, similar to dev-1 and slightly thicker GaS than dev-1. (b) Comparison of responsivity and detectivity for the fabricated devices under similar illumination conditions. (c) Comparison of rise/fall time and power exponent of all the fabricated devices.

A comparison of the *PCE* of the a-vdW devices at 405 nm further supports this claim, as shown in figure 40a. Device-1 achieved the highest *PCE* of 0.8%, while device-3 exhibited half the *PCE* of device-1 at 0.37%, despite having a slightly higher SPD, and device-2 illustrated a *PCE*



that was one order of magnitude lower than device-3, at just 0.047%, under similar illumination conditions. Additionally, a stark difference is observed between other figure of merits such as responsivity, specific detectivity and rise/fall time as illustrated in figure 40b and 40c, for a-vdW devices and EBL patterned device as well, with device-1 outperforming the other 3 devices, with device-3 displaying the second-best performance. These findings further indicate that device-1 possesses the most synergistically optimized conditions in terms of thickness and structure for a robust rectifying p-n heterojunction, capable of efficient photocarrier generation, separation, and extraction, while the vdW-MC ensures a pristine interface, free of FLP further aiding to efficient charge carrier extraction and superior photodetection.

3.2.11. Gate tunable optoelectronic response of the device:

To further explore the device's versatility for multifunctional applications, we investigated its gate tunable characteristics. As illustrated in figure 41a, the device exhibits a strong ambipolar gate tunable characteristics under various applied $V_{\rm ds}$.

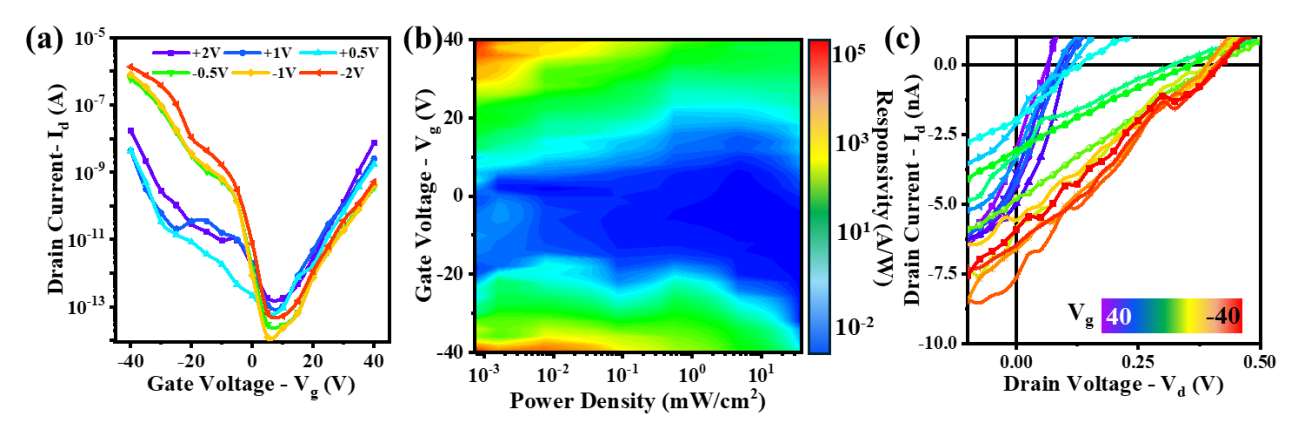


Figure 41. (a) Gate-tunable dark current characteristics at various V_{ds} , showing strong ambipolar response. (b) Gate tunable photoresponse of the device under various illumination intensities. (c) Evolution of V_{OC} and I_{SC} under gate tunable conditions, for optoelectronic logic applications.

We also assessed the device's responsivity under gate tunable conditions (figure 41b), demonstrating a gate tunable ambipolar responsivity of greater than 10^5 A/W at a back gate voltage (V_g) of ± 40 V. This implies that the device can be tuned for high photoresponsivity



applications as well. Additionally, we looked at the possibility of gate tunable I_{SC} and V_{OC} of the device as illustrated in figure 41c. The device shows excellent V_{OC} and I_{SC} tunability as well for possible optoelectronic logic operations.

3.2.12. Potential application in multi-functional optoelectronics:

Multispectral imaging:

To evaluate the device's potential as an image sensor, device-1 was incorporated into a single-pixel imaging system, as depicted in figure 42a.

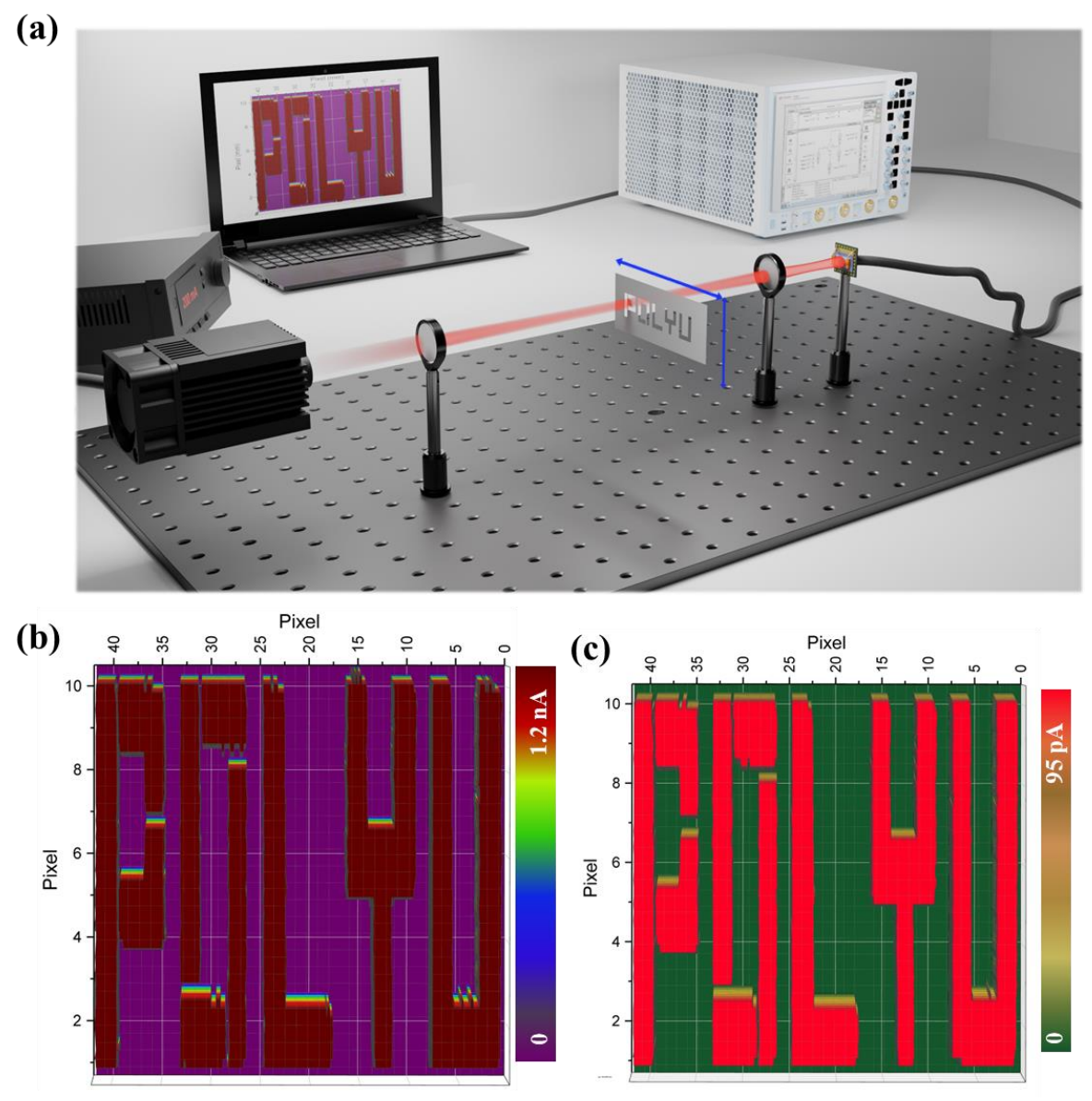


Figure 42. (a) Schematic illustration of a single-pixel imaging system. Reconstructed image of the pattern "P O L Y U" (b) using 405nm illumination and (c) using 810nm illumination.



In practical applications, image sensing is typically conducted using sensor arrays integrated with readout circuitry and amplifiers. The quality of the acquired images is influenced by the pixel size, which is determined by the dimensions of the detector array. In contrast, single-pixel imaging systems mimic the functionality of array detectors by utilizing a single device. Such systems are often employed in scientific demonstrations to illustrate the capabilities of fabricated devices for imaging applications. For our demonstration, a patterned aluminum mask displaying the letters "P O L Y U" was positioned between the light source and the detector. The mask was programmed to move stepwise in the x-y direction using a motorized 2D stage. Light passing through the mask was focused onto the detector via a lens, generating photocurrent signals. The recorded photocurrent data, along with corresponding positional information were reconstituted into a 3D plot using computer software, thereby representing the image acquired by the sensor. Figure 42b displays the image captured using a 405 nm light source, while figure 42c illustrates the imaging capabilities with an 810 nm light source. Notably, the excellent polychromatic imaging capabilities of the demonstrated photodiode can be attributed to its remarkable linearity and synergistic engineering, further supporting its suitability for high-resolution imaging applications at various wavelengths.

Demonstration of Optoelectronic Logic AND gate:

We investigated the device's capability to function in gate-tunable optoelectronic logic applications. As previously mentioned, the device exhibits excellent gate tunability, allowing us to evaluate the variation of V_{OC} in response to varying V_g . This relationship is depicted in figure 43a, where a maximum V_{OC} of 0.41 V is observed at a gate voltage of -40 V. As V_g is increased, V_{OC} demonstrates a pronounced change between gate voltages -10 V and 10 V, stabilizing below 0.15 V, with further increment of V_g to +40 V. Consequently, a high state of V_{OC} is defined as values greater than 0.35 V, while a low state corresponds to values below 0.15 V (as shown in figure 43a). The device schematic for the optoelectronic AND gate is



illustrated in figure 43b, accompanied by a state table that outlines the input conditions (light and V_g) and the corresponding output conditions (V_{OC}).

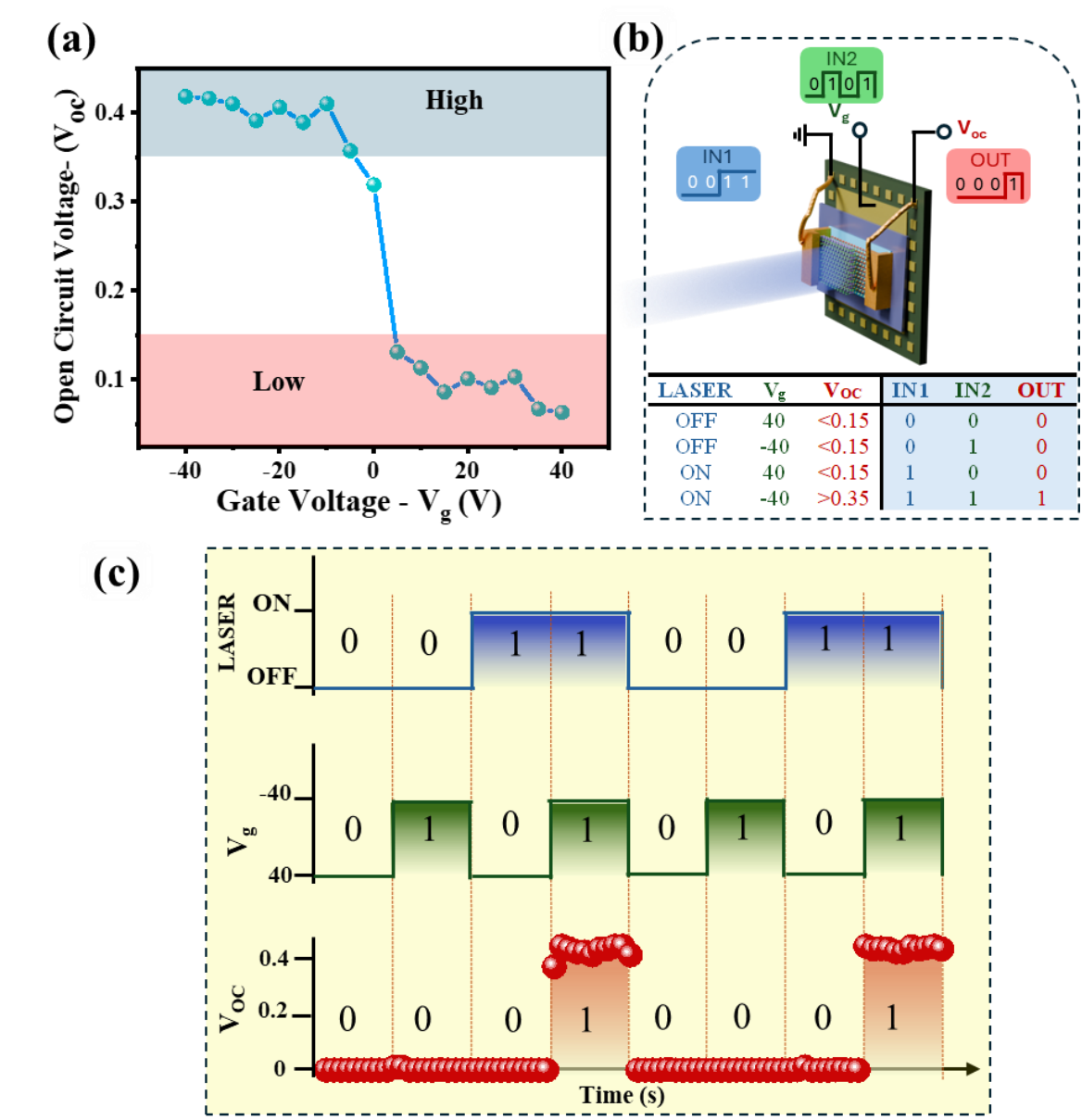


Figure 43. a) Variation of V_{OC} , with tuned V_g , under illumination at 405nm. A state of High $(V_{OC}>0.35\ V)$ and Low $(V_{OC}<0.15\ V)$ could be outlined in the sky blue and pink region, respectively. (b) Schematic Illustration of the Optoelectronic logic AND gate (top) and its' corresponding state table (bottom). (c) State trace and corresponding logic function demonstration of the optoelectronic AND operation.



The device exhibits a clear input-output relationship characteristic of an AND gate, as depicted in figure 43c. This demonstrates its potential functionality in optoelectronic logic operations, reinforcing the viability of the device for advanced multifunctional optoelectronics.

3.2.13. <u>Summary Comparison of Key Performance parameters</u> for all fabricated devices:

A summary of all key performance metrics of all the fabricated devices, investigated under 405nm illumination could be found in table 2.

Table 2. Comparison of device performance parameters of all the fabricated devices under self-bias conditions at 405 nm wavelength:

Parameters	Device-1	Device-2	Device-3	Device-	
$\Delta E_f \text{ (meV)}$	200	125	216	178	
Active Area (µm²)	~28	~52	~30	~32	
Thickness [GaS/WSe ₂] (nm)	8.5/3	11.4/10.9	13.2/3.8	11.5/3.5	
Responsivity (mA/W)	192.87	18.22	90.73	1.79	
Specific Detectivity- D* (Jones)	2.11×10 ¹¹	5.42×10 ¹⁰	7.612×10 ¹⁰	1.59×10 ⁹	
Rise Time /Fall Time (ms)	0.545/0.471	1.24/1.45	0.651/0.807	115/178	
On-off ratio	105	104	105	5×10 ²	
$i_N(AHz^{-1/2})$	~10 ⁻¹⁶	~10-16	~10-16	~10-15	
Power Law Exponent- α	0.98	0.92	0.94	0.55	
Recombination Order - β	1.62	1.2	1.3	-	
Recombination Order - p	Dominant-LV	Dominant-SRH	Dominant-SRH		
Linear Dynamic Range – LDR (dB)	~94.6	~88	~94.2	~73.9	
Photoconversion Efficiency (PCE)	0.8%	0.047%	0.37%	-	
External Quantum Efficiency (EQE)	29.86	2.47	12	0.08	



3.2.14. Comparison of synergistically engineered photodiode to reported high performance photodetector devices:

A performance comparison between our synergistically optimized a-vdW device and other photodetector devices reported with outstanding performance, is presented in table 3

Table 3. Multivariate performance comparison of some of the recently reported heterojunction-based photodetectors with our optimized device.

Device	Contact Type/method [material]	Bandwidth (nm)	Bias (V)	On/Off Ratio	LDR (dB)	α	Response speed	R (AW-1)	D* (Jones)	EQE	Ref
GaS _{0.87} - WS ₂	Top/EBL [Au]	395-622	5	-	73	0.7	10s	13	-	-	[117]
MoTe ₂ - BP	Top/EBL [Cr/Au]	520-2000	0	-	-	0.95	78/176µs	0.290	-	70	[146]
MoS ₂ - WSe ₂ - PbS-QD	Bottom/ vdW [Au]	405-1064	0	1	66	0.91	48/43μs	0.75	5.15×10 ¹¹		[147]
Bi ₂ O ₂ Se- In ₂ S ₃	Top/UVL [Ti/Au]	532	1	105	-	0.69	170/296μs	144	1.2× 10 ¹⁴	-	[134]
PdSe ₂ - MoTe ₂	Top/EBL [Ti/Au]	375-1550	0	-	ı	ı	3.5/3.7ms	0.243	6.46× 10 ¹⁰	56.73	[139]
MLG - ReSe ₂ - SnSe ₂	Top/UVL [Cr/Au]	638	0	10 ⁵	103	0.84	752/928µs	0.144	2.4× 10 ¹⁰	-	[133]
WSe ₂ - Bi ₂ O ₂ Se	Top/EBL [Cr/Au]	532	0	10 ⁵	-	-	20/20μs	0.284	-	66.27	[84]
MoTe ₂ - MoS ₂	Top/EBL [Cr/Au & Pd/Au]	500-1200	0	10 ⁵	-	0.701	60µs	0.046	1.06× 10 ⁸	-	[136]
WSe ₂ - MoS ₂ - WSe ₂	Top [Au]	405-808	0	10^{4}	-	-	45µs	0.715	1.59×10 ¹³	-	[83]
MoS ₂ - MoTe ₂ - MoS ₂ - MoTe ₂	Top/vdW [Au]	405-1600	0	10 ⁵	100	1	30μs	1.57	4.28× 10 ¹¹	365.8	[82]
GaS- WSe ₂	Top/vdW [Ag/Au]	275-1064	0	10 ⁵	106.78	0.99	545/ 471μs	0.376	4.12 × 10 ¹¹	30	This work



3.2.15. Comparison of synergistically engineered photodiode to reported high performance vdW solar cell devices:

Table 4 represents a comparison of our device's performance with some high performance 2D solar cells.

Table 4. Comparison of reported solar cell figure of merits with synergistically engineered photodiode.

Device [Structure]	V _{OC} (V)	J _{SC} (mA/cm ²)	FF	PCE (%)	Illumination Conditions	Area (cm²)	Ref
WSe ₂ /MoS ₂ [Lateral]	0.22	0.02	0.39	0.2	White light source [1 mW/cm ²]	3.2 × 10 ⁻⁷	[148]
WSe ₂ /MoS ₂ [Lateral]	0.39	17.75	0.37	2.56	AM 1.5 G $[100 \text{mW/cm}^2]$	4 × 10 ⁻⁸	[149]
WSe ₂ -MoS ₂ [Vertical]	0.56	0.58	0.5	0.2	White light source [640 mW/cm ²]	8.57 × 10 ⁻⁸	[137]
Gr-WSe ₂ -MoS ₂ -Au [Vertical]	0.35	1111.1	0.45	3.4	LASER (633-nm) [7.4×10 ⁵ mW/cm ²]	9 × 10 ⁻⁶	[110]
WSe ₂ -Gr-MoS ₂ [Vertical]	0.23	24.38	-	-	LASER (488-nm) [25μW]	3.3 × 10 ⁻⁶	[150]
GaS-WSe ₂ [Semi-Vertical]	0.36	5.42	0.32	1.18	LASER (450-nm) [51.5mW/cm ²]	2.8 × 10 ⁻⁷	This Work

3.3. Conclusion:

In summary, we have synergistically engineered a-vdW type-II heterostructure photodiode, leveraging a GaS-WSe₂ heterojunction, meticulously engineered to achieve favorable balance among photocarrier generation-recombination, separation, transport, and extraction, eventually facilitating a highly sensitive, broadband photodetector. The device exhibits ultralow light detection capabilities with polychromatic unity approaching linearity, photovoltaic responsivity and detectivity of 376.78 mA/W and 4.12×10^{11} Jones respectively. The device also demonstrates a large on/off ratio of 10^5 , substantial LDR of 106.78dB, stabilized large EQE of 30%, FF and V_{OC} of 0.33 and 0.36 respectively, with response speeds of $545/471~\mu s$, showing excellent prospects in imaging and solar cell applications. Moreover, demonstration



of gate tunable ambipolar responsivity of the photodiode, further expanded its applicability in gate tunable optoelectronic logic gate. Our systematic investigation on key performance indicators like power exponent and PCE for multiple devices reinstates the need for meticulous engineering of vdW heterointerfaces, particularly the effects of vdW-m thickness and contact integration strategies that severely influence characteristics performance of the devices. Our results presented in this work open an exciting route for future investigations that can be universally adopted to achieve photovoltaic heterojunctions with near unity linearity in other vdW-m with moderately large bandgaps.



Chapter 4: Graphene contacted GaS all van der Waals photodiodes

4.1. Introduction:

In this chapter a Graphene-GaS-Au all van der Waals photodiode is presented. The device demonstrates a detection bandwidth of 275 nm - 455 nm, self-powered responsivity of 150 mA/W and a rise/fall time of 15.98/35.99 ms. Additionally, the device shows dual axis spiking features in its temporal response under ultra-low light illumination. Utilizing the spiking features of the pulsed, response, the device shows an extra-ordinary enhancement in its self-powered spiking responsivity of 0.7 A/W with a corresponding detectivity of 7.67×10^{11} Jones.

4.2. Gr-GaS-Au a-vdW heterojunction diode:

4.2.1. <u>Fabrication and Characterization of the a-vdW Gr-GaS-Au</u> photodetector:

Few layer Graphene (Gr) (NGS GmbH) was exfoliated on a 285nm oxidized silicon substrate that was previously cleaned in acetone, IPA and DI water using ultrasonication. Few layer Gallium Sulfide (GaS) (HQ Graphene) was exfoliated on PDMS and after observation under optical microscope, a flake of appropriate thickness was identified and transferred to the few layer graphene flake using a home built micro precision and alignment transfer stage to form Gr-GaS heterojunction. The heterojunction was annealed under 50 SCCM argon flow for 2 hours at 200 °C to enhance the coupling between the layers. Contact electrodes were integrated utilizing a similar method reported in chapter-3, fabrication section. Briefly, 50nm gold (Au) electrodes were deposited on photolithographically patterned silicon substrate, which was then spin coated with thermoplastic Poly vinyl alcohol (PVA) solution at 3000rpm and then



hardened using hotplate heating. PVA film with the 50nm Au wrapped underneath was mechanically peeled off from the sacrificial substrate and with the help of PDMS stamp and transfer stage, the PVA film with the 50nm Au electrodes was precisely stamped on to the previously prepared Gr-GaS heterojunction and finally dissolved in warm DI water to form Gr-GaS-Au a-vdW photodetector. A schematic illustration of the as prepared Gr-GaS-Au photodetector can be found in figure 44a. The optical microscope image in figure 44b reveals the device structure of the as prepared photodetector with an active area of 72µm². Raman spectroscopy of the few layer GaS, as outlined in figure 44c illustrates the well-known strong out of plane vibration modes A¹1g and A²1g at 185cm⁻¹ and 361cm⁻¹, respectively while E¹2g mode relates to the well-known in plane vibration mode at 291cm⁻¹, in line with previous reports for Raman spectroscopy of ultra-thin GaS nanosheets [111,126,129].

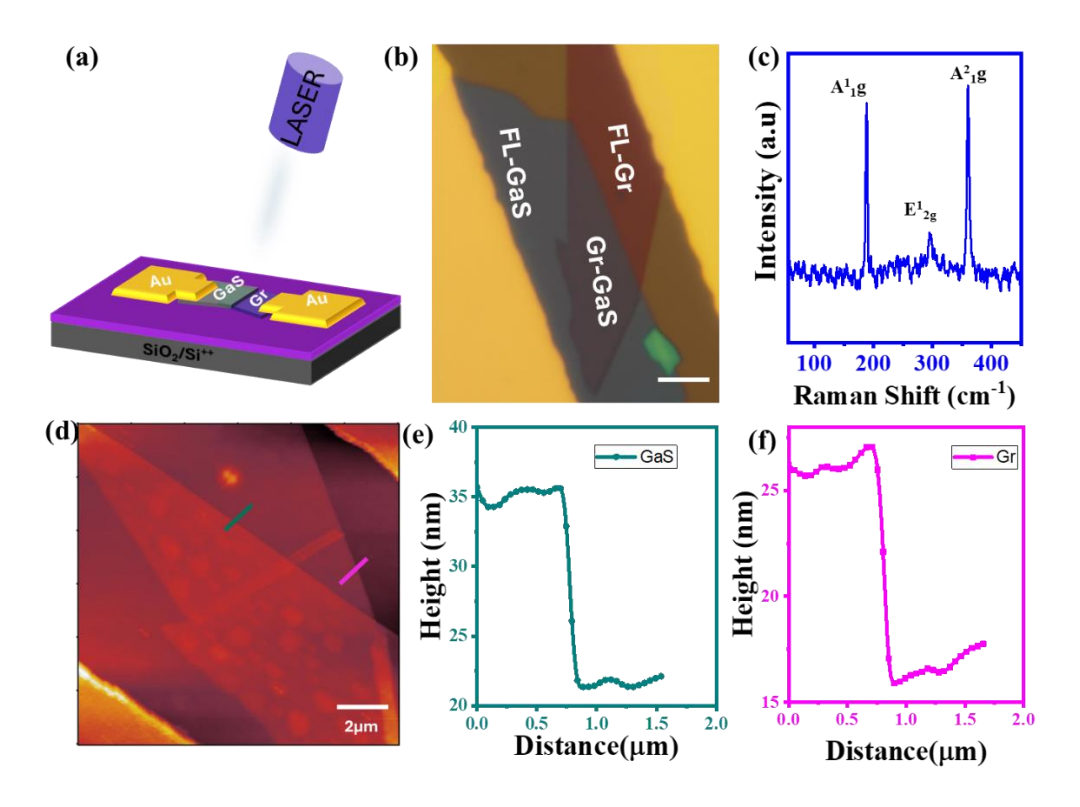


Figure 44. (a) Schematic Illustration of the self-powered Gr-GaS-Au a-vdW Photodetector. (b) Microscope image of the fabricated device. (c) Raman spectrum of multilayered GaS depicting the in plane and out of plane vibration modes. (d) Atomic Force Microscopy image of Gr-GaS heterojunction and (e) & (f) height profiles of few layer Gallium Sulfide (~14nm) and few layers of graphene contact (~10nm), respectively.



Atomic force microscopy was employed to identify the height profile of the device as illustrated in figure 44d. The height profiles revealed a GaS flake of 14nm thickness (figure 44e) and Gr contact with a thickness of 10nm (figure 44f)).

4.2.2. Optoelectronic Characterization of the device:

We next probed the optoelectronic performance of the a-vdW device for photodetection characteristics. Figure 45a illustrates the I-V characteristics of the device under dark conditions. A clear rectifying characteristic is observed denoting diode features with a rectification ratio of ~105. Additionally, under illumination conditions, the device also exhibits common rectification characteristics with excellent response in the 375nm regime, with response of the device recorded within 275nm to 455nm as illustrated in figure 50b.

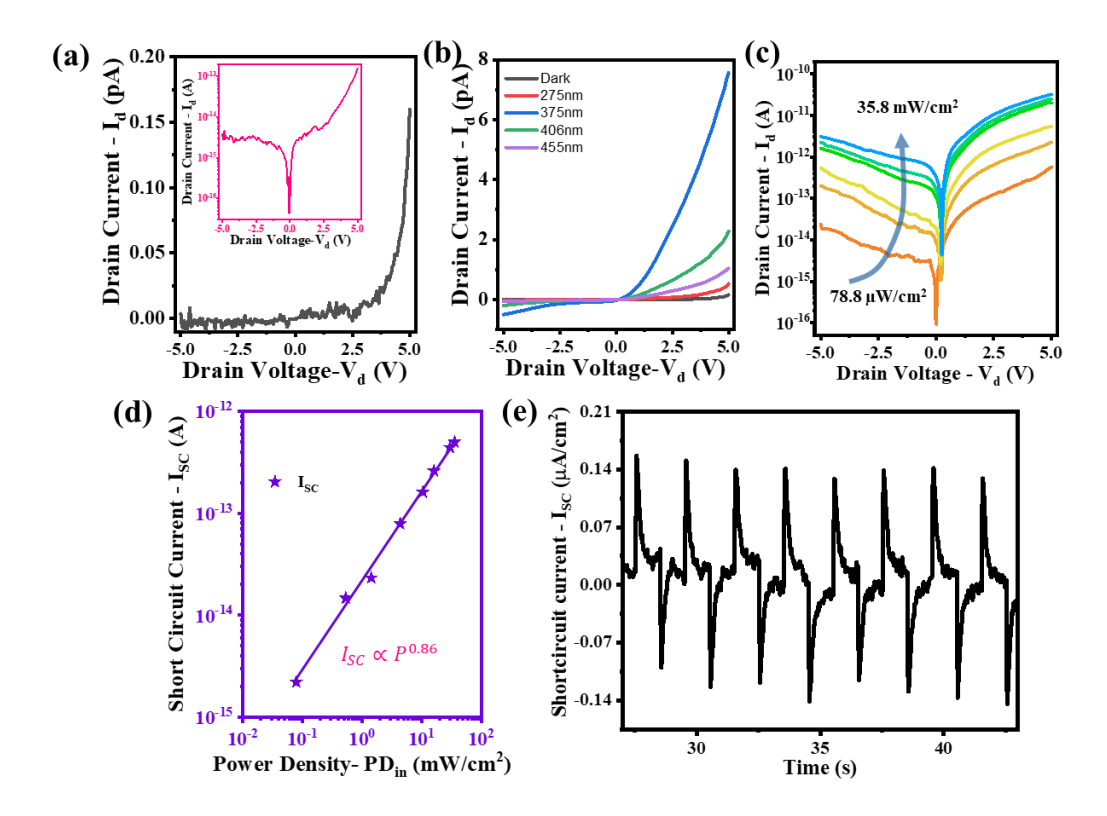


Figure 45. (a) I_d - V_d characteristics of the device under dark conditions. (b) I_d - V_d characteristics of the device under illumination conditions. (c) $\log I_d$ - V_d characteristics of the device under variant power densities at 406nm illumination. (d) I_{SC} vs power density with α value of 0.86, suggesting trapping and recombination in the semiconductor. (e) Temporal response of the device under 375nm illumination, showing pyro-electric features.



We further explored the device's response under 406nm illumination, with intensities ranging between $78.8 \,\mu\text{W/cm}^2$ to $35.8 \,\text{mW/cm}^2$. As illustrated in figure 45c, the device maintains sharp diode like I_d - V_d features, with clear built-in potential developed as light power density is increased. However the developed built-in potential and the short-circuit current extracted were inferior to the device presented in chapter-3, likely due to presence of large back to back Schottky barrier between GaS-Au and GaS-Gr junctions.

The dependence of photocurrent on light intensity can be fitted well by the power law of $I_{SC} \propto P^{\alpha}$, where the power law exponent α has a value of 0.86 as illustrated in figure 45d, suggesting the heterojunction device shows enhanced trapping induced recombination, inside the semiconductor and needs further improvements in the contact region for extraction of photocarrier.

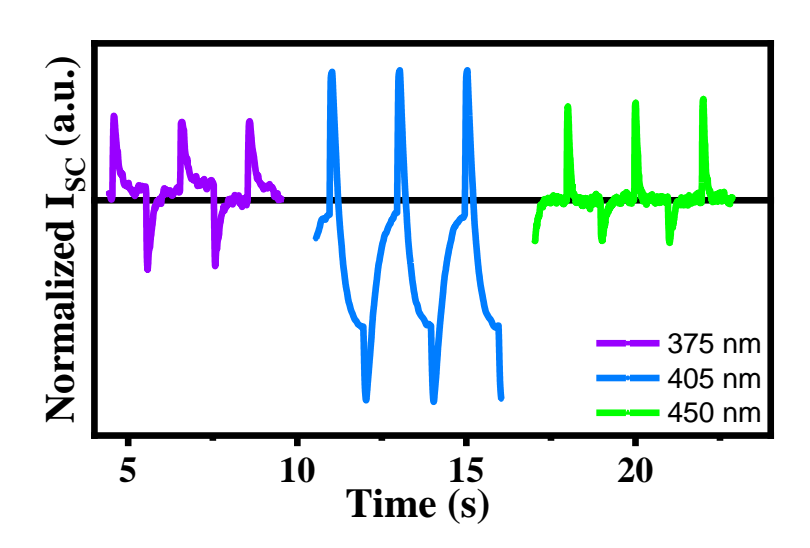


Figure 46. Recorded spiking photo-current effect in Gr-GaS-Au a-vdW device under 375nm, 405nm and 450nm illumination.

To further probe the devices performance under pulsed light condition, the device was probed under the lowest detection capabilities at our disposal at a light power density of $0.2\mu\text{W/cm}^2$. The device shows a temporal response of a typical pyroelectric detector with temporal spikes in both positive and negative photocurrent axis as illustrated in figure 45e. The spiking responsivity of the device under this illumination condition is 0.7A/W, which much larger than



previously reported spiking like pyroelectric detectors under UV-Vis illumination [151–153]. Additionally, investigation under multiple wavelengths as outlined in figure 46, the device indeed demonstrates broadband spiking response under multiple wavelengths at ultra-low light intensities of $\sim \mu \text{W/cm}^2$, paving the way for vdW heterojunction based pulsing photodetectors.

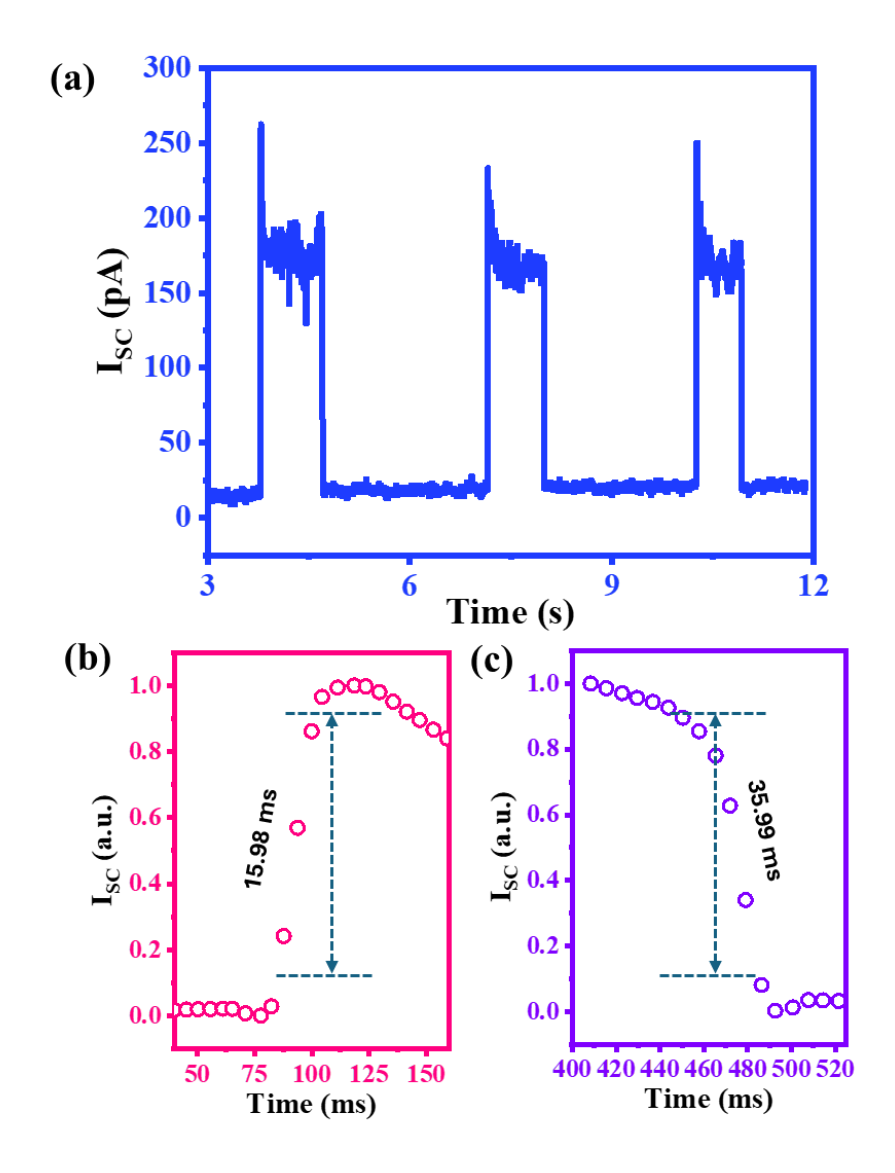


Figure 47. (a) Temporal response of the device under 375nm illumination. (b) Rise time of the device (b) Fall time of the device.

The temporal response of the device under elevated pulsed light condition is presented in figure 47a for 3 on-off cycles. The device shows a maximum on-off ratio of 10⁴ under pulsing conditions, with increasing the illumination intensity of the light source 375nm, and illustrates



a steady state persistent short circuit photocurrent, with an initial spike like feature presented in figure 46. Additionally, the risetime and fall time of the device was obtained from the temporal response as presented in figure 47b and c and it was found to be around 15.98 ms and 35.99 ms respectively. The risetime and fall time reported for our Au-GaS-Gr device is much faster than previously reported any of the GaS based devices that were under voltage biased conditions [111,129]. This clearly suggests a-vdW approach for device fabrications using vdW metal integration technique is the best method to avoid FLP induced device performance degradation.

The noise characteristics of the device was analyzed next. As illustrated in figure 48a, the dark trace for 5 second shows a dark current characteristic similar to the a-vdW GaS-WSe₂ heterojunction presented in chapter-3.

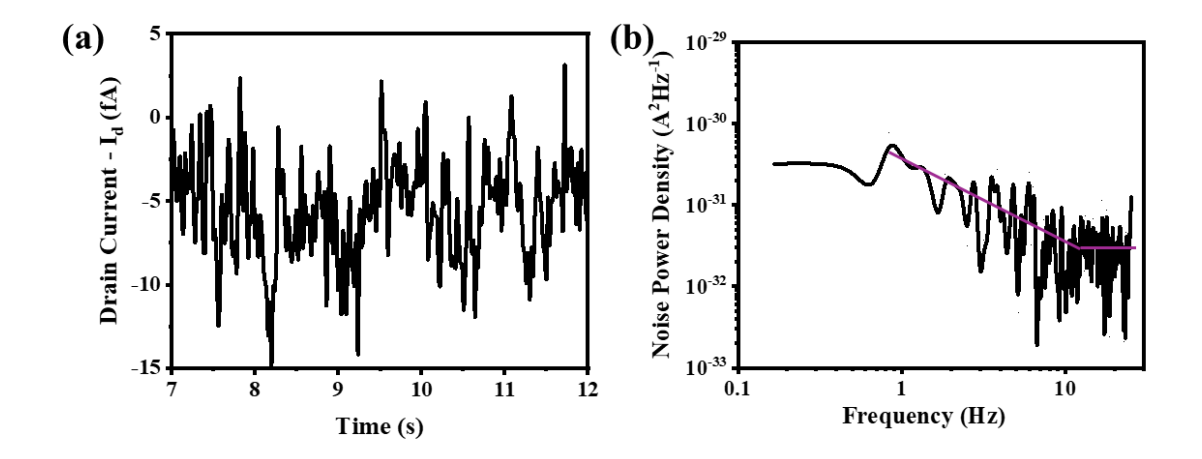


Figure 48. (a) Dark current trace of Gr-GaS-Au photodiode (b) Corresponding Noise Power Density plot.

The dark current traces of the device was obtained using Agilent B1500 semiconductor parameter analyzer at $V_{ds} = 0$ V at a sampling rate of 50 Hz for 5 seconds. Noise power density was obtained from the Fourier transform of the time evolution of the dark current is presented in figure 48b. A flicker noise linear fit $(1/f)^{\alpha}$ could be interpreted for the device, suggesting low frequency flicker noise dominant characteristics. The measured noise currents was 7.74×10^{-1}



 16 AHz^{-1/2}, suggesting the device can also deliver ultra-low light detection performance. The noise current obtained from linear fitting of the noise density plot could be used for estimating the NEP using equation 17. The obtained *NEP* is 1.1 fWHz⁻¹, which could be used to obtain maximum self-powered spiking D^* of 7.67×10^{11} Jones at 375nm.

4.3. Conclusion:

A Graphene-GaS-Au a-vdW photodiode was presented in this chapter. The device exhibited a detection bandwidth of 275 nm to 455 nm, a self-powered responsivity of 150 mA/W, and rise/fall times of 15.98 ms and 35.99 ms, respectively. Additionally, it showcased dual-axis spiking features in its temporal response under ultra-low light illumination. By leveraging these spiking characteristics, the device achieves an extraordinary enhancement in its self-powered spiking responsivity of 0.7 A/W, with a corresponding detectivity of 7.67×10¹¹ Jones.



Chapter 5: Conclusion and Future work:

This chapter summarizes the work presented in this thesis and continued future work. At the beginning, a brief summary of the a-vdW GaS-WSe₂ synergistically engineered photodiode is presented. Afterwards, a brief summary of Gr-GaS-Au all van der Waals photodiode is presented. Finally, future work on Gr-GaS-WSe₂ based photodiode is presented.

5.1. Summary of investigation presented in this thesis:

The multivariate optimizable strategy in vdW heterojunctions is a crucial aspect of research related to vdW heterostructure photodiodes. Transitional metal dichalcogenides and metal monochalcogenides are particularly important for optoelectronic sensing applications due to their enhanced light-matter interaction, high charge carrier mobility, and layer-dependent tunable bandgaps—all achievable within the ultra-thin regime of a few atomic layers.

Through a meticulous engineering strategy, we report on a photovoltaic type-II, "all van der Waals" GaS-WSe₂ heterojunction photodetector. This device features optimized thickness, structure, and contacts to achieve a broadband detection response spanning from 275 nm to 1064 nm, with multispectral unity approaching linearity and a significant linear dynamic range of 106.78 dB. The device also demonstrates a large on/off ratio of 10⁵, fast response times of 545 μs and 471 μs, and ultra-low light detection capabilities, achieving dark currents around ~fA. This results in a peak responsivity of 376.78 mA/W and a detectivity of 4.12×10¹¹ Jones, along with a stabilized external quantum efficiency (EQE) of 30% and a fill factor of approximately 0.33—all accomplished through a single junction. The term "all van der Waals" is used to describe this device due to the integration of metal contacts with intimate vdW interactions.

Furthermore, our systematic investigation of multiple a-vdW devices, alongside a control device fabricated using traditional electron beam lithography (EBL)-patterned contacts for



comparison, covers key performance attributes such as junction potentials and electronic-optoelectronic characteristics. This work underscores the essential role of a meticulous approach to thickness-engineered layers in establishing a robust depletion region for the GaS-WSe2_22 type-II heterojunction. It also highlights the modulation of Schottky barrier height via vdW-MC, achieving a FLP-free vdW metal-vdW-m interface. This optimization is beneficial for promoting recombination resilience and high linearity, striking a favorable balance among photocarrier generation, recombination, separation, transport, and extraction, ultimately facilitating a highly sensitive, broadband photodiode.

Additionally, a Graphene-GaS-Au all van der Waals photodiode was fabricated to investigate the impact of Schottky junctions within the all van der Waals strategy. The device demonstrated a bandwidth ranging from 275 nm to 455 nm, with a self-powered responsivity of 150 mA/W and rise/fall times of 15.98 ms and 35.99 ms, respectively. Additionally, it exhibited dual-axis spiking features in its temporal response under ultra-low light illumination. By leveraging these spiking characteristics, the device achieved an extraordinary enhancement in self-powered spiking responsivity of 0.7 A/W, along with a corresponding detectivity of 7.67×10^{11} Jones.

5.2. Future Work: Gr-GaS-WSe₂ based ultra-efficient photodiodes

In this section we look into a Gr-GaS-WSe₂ based photo detector. As stated in chapter-3 WSe₂-GaS provides a robust p-n junction for photodetection and utilizing graphene as bottom contact to the GaS is expected to enhance the carrier collection efficiency, as demonstrated in previous reports [67]. To compensate the lower in-plane mobility in GaS, utilizing graphene for charge carrier extraction could be and excellent choice and hence we investigate the possibilities of a Gr-GaS-WSe₂ heterojunction, integrated to a vdW transferred Au contacts.



5.2.1. Fabrication of a-vdW Gr-GaS-WSe₂ heterojunction:

Few layer Graphene (FL-Gr) (NGS GmbH) was exfoliated on a 285nm oxidized silicon substrate that was previously cleaned in acetone, IPA and DI water using ultrasonication. Few layer Gallium Sulfide (GaS) (HQ Graphene) and WSe₂ (HQ Graphene) were exfoliated on PDMS and after observation under optical microscope, flakes of appropriate thickness were identified and transferred to the few layer graphene flake, sequentially, using a home built micro precision and alignment transfer stage to form Gr-GaS-WSe₂ heterojunction. The heterojunction was annealed under 50 SCCM argon flow for 2 hours at 200 °C to enhance the coupling between the layers. Contact electrodes were integrated utilizing the method reported in section 4.2.2. Figure 49a illustrates the schematic of the device while figure 49b illustrates the optical micrograph image of the device.

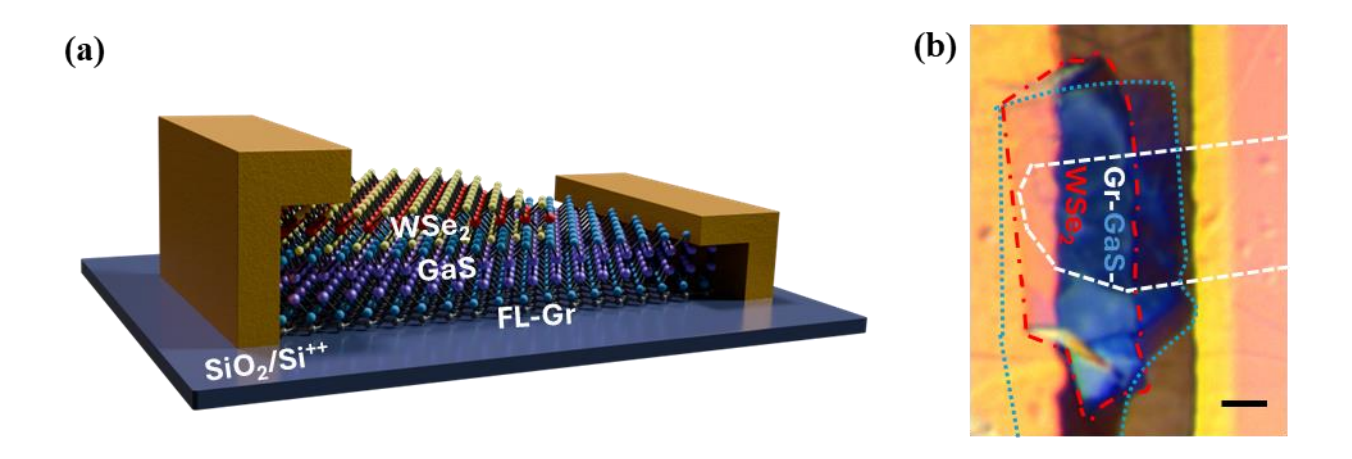


Figure 49. (a) Schematic illustration of the Gr-GaS-WSe₂ a-vdW heterojunction photodetector. (b) Optical micrograph image of the device.



5.2.2. Characterization of the heterojunction:

Raman characteristics of the prepared heterojunction as illustrated in figure 49a.

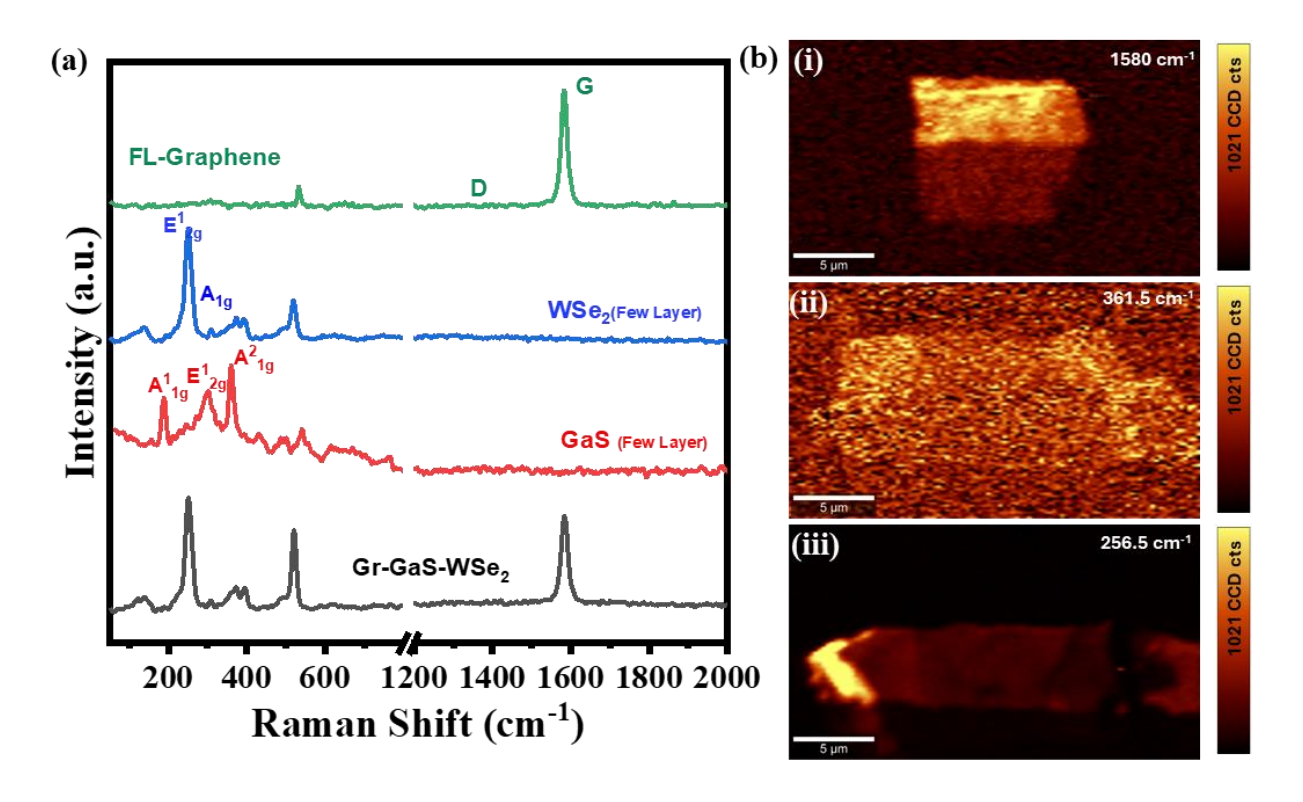


Figure 50. (a) Raman characteristics of bare FL-Gr, bare GaS and bare WSe₂ and the constituent heterojunction region, showing all the characteristics Raman peaks, highlighting a robust heterojunction. (b) Raman mapping of (i) FL-Gr G band (1580cm⁻¹) (ii) GaS A²_{1g} band (361.5cm⁻¹) and (iii) WSe₂ A1g band (256.5cm⁻¹). Intense "Raman quenching" is evident for all the bands mentioned, in the Gr-GaS-WSe₂ region suggesting robust coupling.

Few layer graphene in the bare regions illustrated its prominent characteristics G band peak at 1580cm⁻¹ while almost diminished D and 2D peaks at 1337 cm⁻¹ and 2684cm⁻¹ respectively, For few-layer GaS, the prominent vibrational modes A¹_{1g} and A²_{1g} were identified at 188.16 cm⁻¹ and 361.5cm⁻¹, respectively, while the less prominent E¹_{2g} mode appeared at 296.01cm⁻¹, consistent with previous reports [124]. Likewise, few-layer WSe₂ exhibited a prominent inplane mode E¹_{2g} at 249.58cm⁻¹ and a weak out-of-plane A_{1g} mode at 256.5cm⁻¹ [125,126]. In the overlapped region between WSe₂ and GaS, all peaks corresponding to the individual layers were observed, indicating a high-quality heterojunction. Moreover, to further investigate the



charge transfer characteristics and coupling effects, we performed Raman intensity mapping, illustrated in figure 50b. As shown in the Raman intensity mapping in figure 50b(i), no considerable quenching was observed for FL-Gr G band intensity in the overlapping region between Gr-GaS region. However, for all the peaks (256.94cm⁻¹, 361.58 cm⁻¹ and 1850cm⁻¹) we observed a notable reduction in Raman intensity in the Gr-GaS-WSe₂ heterojunction region—a phenomenon known as "Raman quench"—which signifies strong interfacial coupling between the Gr, GaS and WSe₂ flakes [84,122]. Hence we can conclude that most of the charge transfer in the heterojunction would occur in this region, during illumination, due to strong built-in potential in the GaS-WSe₂ region, that facilitates direct tunneling thorough the Schottky barrier.

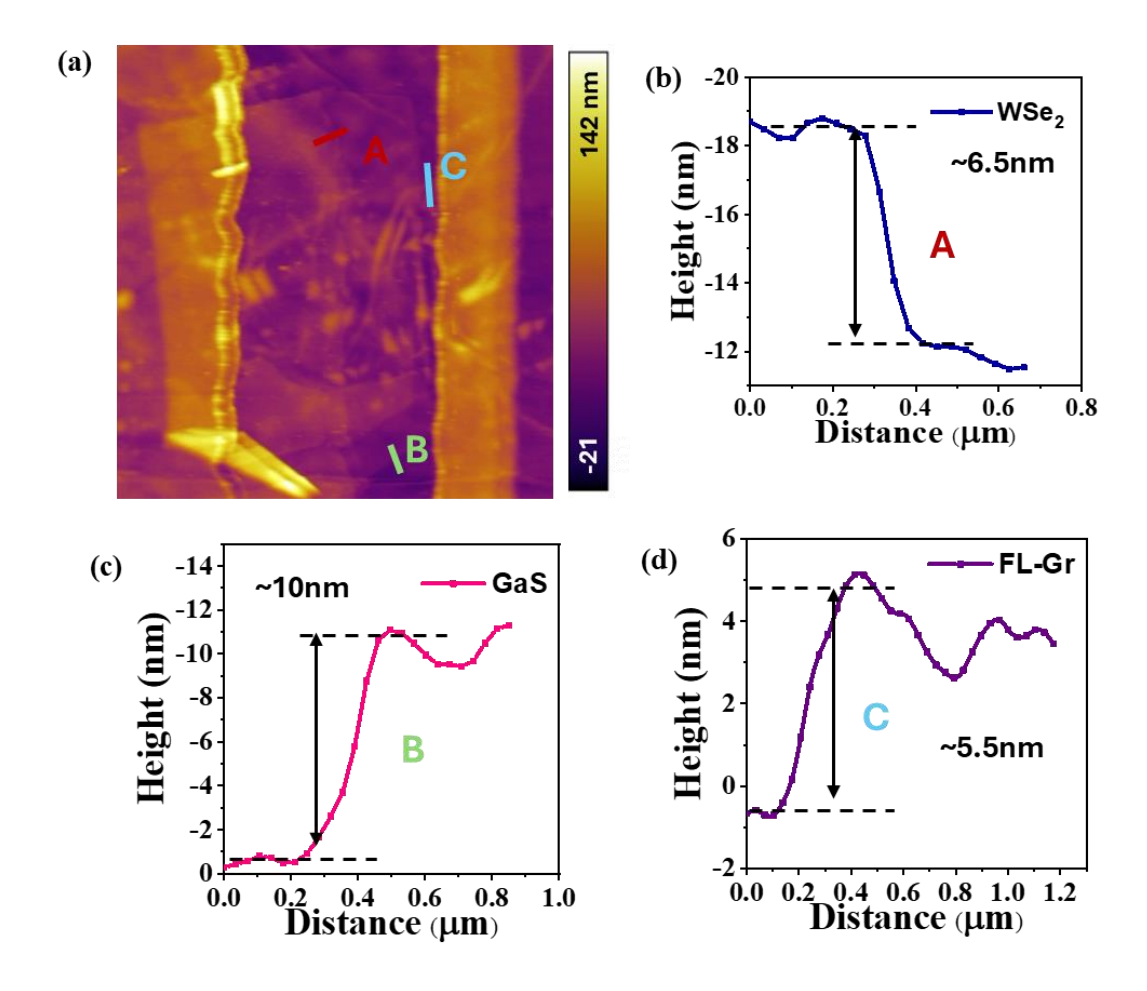


Figure 51. (a) AFM image of the heterojunction device. Height profile of (a) WSe₂, (b) GaS and (c) FL-Gr, showing their corresponding thickness.



We next look at the height profile of the prepared heterojunction detector. Figure 51a illustrates AFM image of the heterojunction device. The measured height profiles reveal a WSe₂ thickness of \sim 6.5 nm (figure 51b), GaS thickness of \sim 10nm (figure 51c) and FL-Gr thickness of 5.5nm (figure 51d). The total thickness of the device would be around 22nm, with an active area of \sim 32 μ m².

5.2.3. Optoelectronic characteristics of the a-vdW Gr-GaS-WSe₂ heterojunction:

We next look at the optoelectronic characteristics of the a-vdW Gr-GaS-WSe₂ heterojunction.

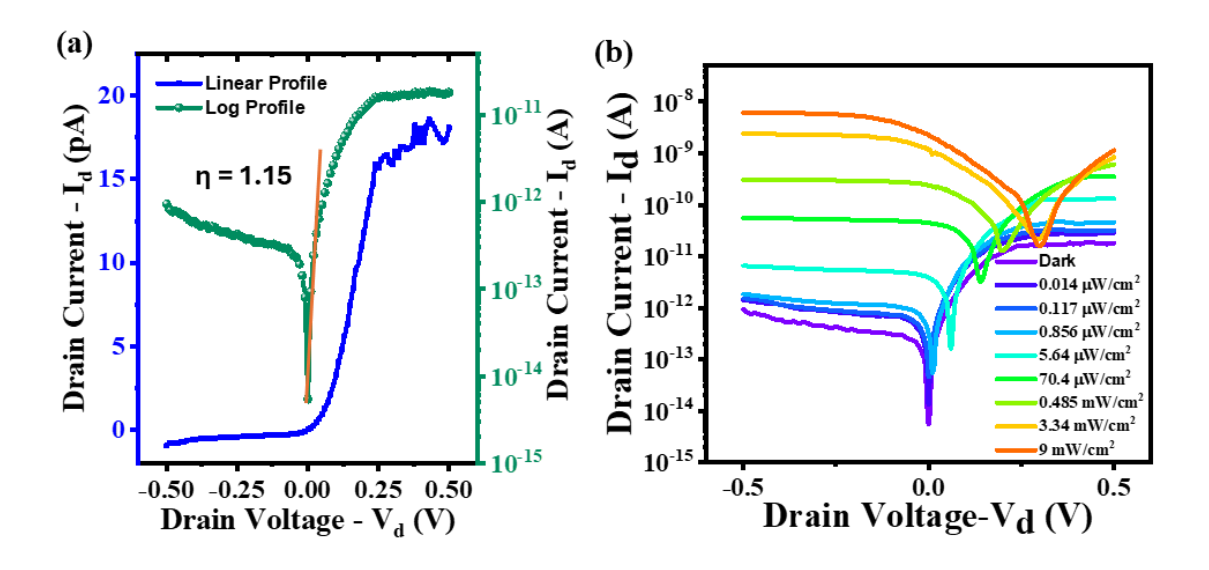


Figure 52. (a) I_d - V_d characteristics of the diode under dark conditions (b) I_d - V_d characteristics of the device under illumination conditions.

Figure 52a represents the I-V characteristics of the device under dark conditions. The Gr-GaS-WSe₂ heterojunction shows an excellent diode like characteristics with a rectification ratio of ~ 100 at ± 0.5 V, with an impressive ideality factor η of 1.15. Additionally, it could be observed that the forward current is clamped at ~ 0.3 V, likely due to the emergence of Schottky barrier between Gr-GaS interface as stated earlier, clamping the forward current injection. Figure 52b represents the I_d - V_d of the device under 405nm illumination under variable input light power



density. A strong built-in potential is observed in the as the illumination density evolves from $0.014\mu\text{W/cm}^2$ to 9mW/cm^2 , demonstrating the device's ability to detect ultra-low light, superior to the devices we presented chapter-3 and chapter-4. Additionally, the I_{SC} under illumination condition is much larger than the devices reported in chapter-3. This is likely due to high efficiency of collection of photogenerated carriers by the FL-Gr, which might have enhanced the overall device performance [67].

We next look at the charge transfer under illumination conditions. As illustrated in figure 53, the pseudo band diagram under illumination conditions is illustrated.

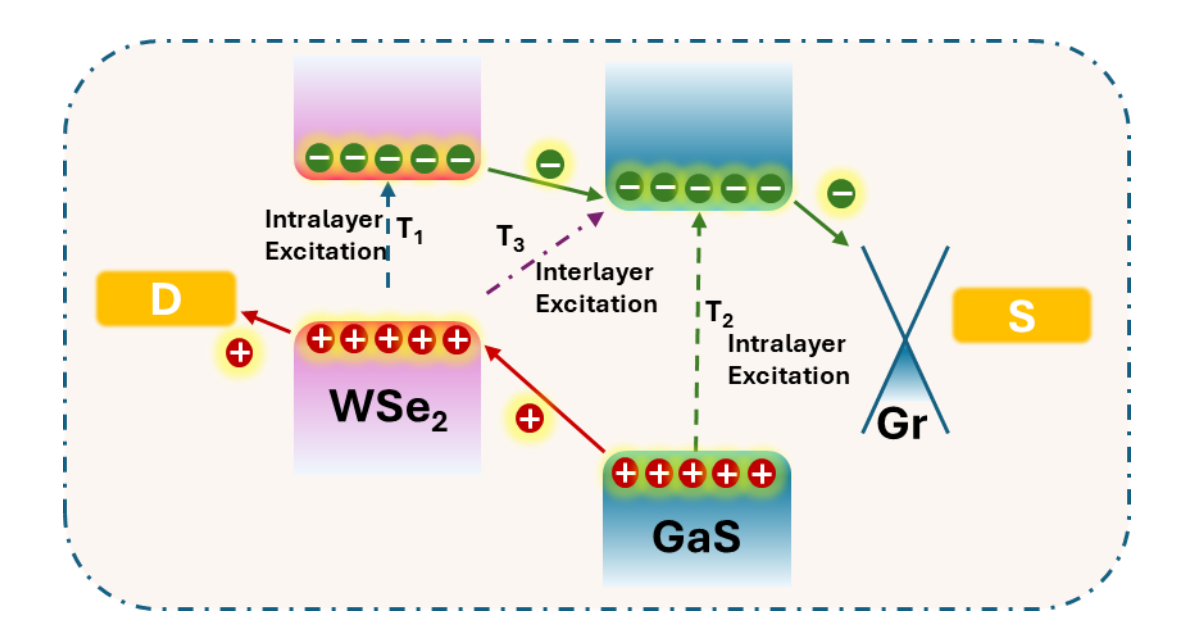


Figure 53. Exciton dissociation and charge transfer in the Gr-GaS-WSe₂ heterojunction.

During quasi-equilibrium state of illumination, at lower wavelengths (< 450nm), the intra layer excitation T₂, dominates the excitonic dissociation in GaS layer producing electron hole-pairs that are separated by the built-in potential in the heterojunction, causing electron and hole transit towards the source and drain contacts respectively, where FL- graphene collects the photo-electrons and the Au vdW contact at the WSe₂ end collects the photogenerated holes. As the excitation wavelength transitions toward higher wavelength, contribution of excitonic transitions from WSe₂ with intralayer excitation T₁ aids to the photocurrent generation with



highest responsivity observed at 450nm as previously discussed. At illumination wavelengths below the bandgap of GaS (i.e. $\lambda >$ 490nm), intra layer excitation T_1 path dominates excitonic transitions and the responsivity of the device starts to decay. As the illumination reaches beyond bandgap of ultra-thinWSe₂, ($\lambda >$ 850nm), interlayer excitonic transition T_3 contributes mostly to the charge transport and excitonic dissociation.

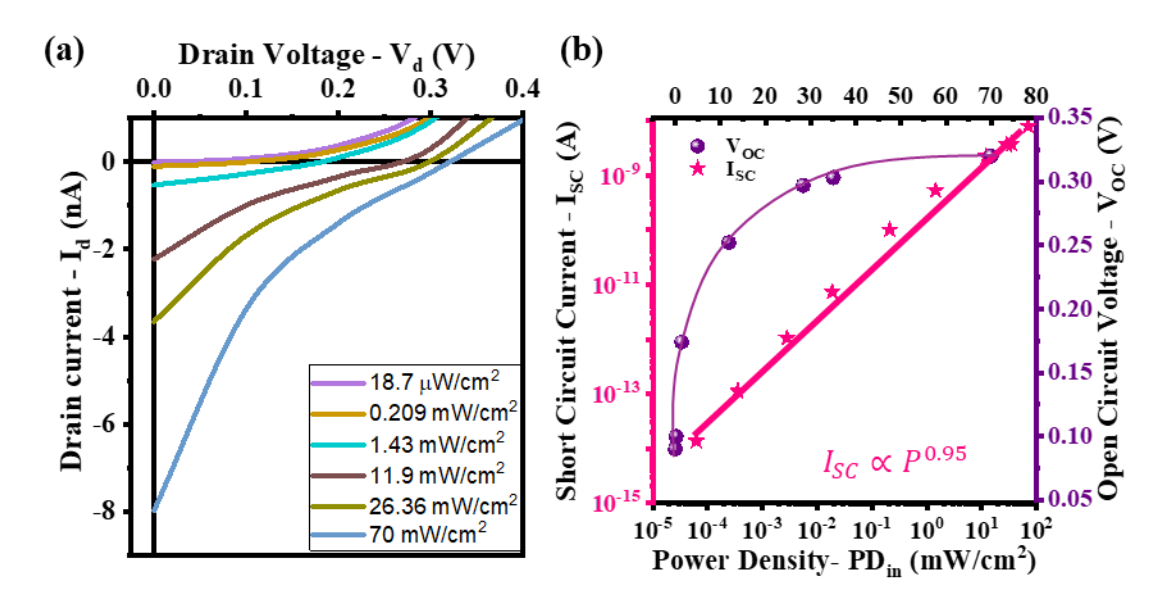


Figure 54. (a) I_d - V_d characteristics of the device showing I_{SC} and V_{OC} cross-overs at respective axis. (b) Input light Power density vs V_{OC} and I_{SC} of the device.

Figure 54a represents the zoomed I_d - V_d characteristics of the Gr-GaS-WSe₂ device under variant illumination conditions. As the illumination power density is increased power increases, a significant increase in the short circuit current (I_{SC}) and open circuit voltage (V_{OC}) is observed clearly from the crossover at the respective axis. The photovoltaic effect of the heterojunction was assessed using the measurements of I_{SC} and V_{OC} , from figure 54b. V_{OC} shows a linear scaling dependence with the log of the input power density (PD_{in}), with no evident saturation as PD_{in} reaches ~70mW/cm², with a maximum V_{OC} of 0.33V. The photocurrent (I_{ph}) of the detector is defined as the difference between drain current under illumination and dark condition ($I_{ph}=I_{light}-I_{dark}$). In the case of our a-vdW Gr-GaS-WSe₂ detector, where there is absence of source-drain bias, the dark current (I_{dark}) of our investigated devices were in the ~fA



range, which is impressively low and the current under illumination (I_{light}) could be written as $I_{light} \approx I_{SC}$. Interestingly, the double log plot of I_{SC} vs PD_{in} , shows an impressive linearity, with no saturation observed in our investigated maximum PD_{in} (70mW/cm²), with an impressive power exponent, α (i.e. $I_{SC} \propto PD_{in}^{\alpha}$) of 0.95. The linear regime of the I_{SC} - PD_{in} , can be quantified by an important figure of merit, the linear dynamic range (LDR) of the photodiode, in dB, and could be obtained. Based on the reported results in figure 54b, the LDR of our optimized junction is 133.97dB. It is worth noting that 133.97 dB is still underestimated due to the limited illumination conditions available at our disposal. This suggests Gr-GaS-WSe₂ vdW heterojunction shows superior performance than our previously reported GaS-WSe₂ p-n junction likely due to the integration of the FL-Gr contact, which allows excellent charge carrier collection efficiency.

Additionally, we also investigated the electrical power production from the diode (P_{el}/I_{ds} . V_{ds}) with a maximum power produced as 0.350nW (figure 55a). The calculated power conversion efficiency (PCE) using the maximum electrical power $P_{el_{max}}$ using equation 12, is presented in figure 54a. It is observed from the figure that with increase in P_{in} , the PCE decreases from a maximum value of 6.23 to 1.58%, demonstrating that the heterojunction reached its saturated capacity of energy conversion and light harvesting at the p-n junction and its capacity to efficiently transport it to the contacts.

The photovoltaic responsivity (R) of the device was obtained using the ratio of the photocurrent to the input optical power (i.e. $R = I_{ph}/P_{in}$). As represented in figure 55b, photovoltaic responsivity shows a gradual increase with increase in light power reaching a maximum photovoltaic responsivity of ~1.5A/W, at ~1mW/cm² before gradual declination.



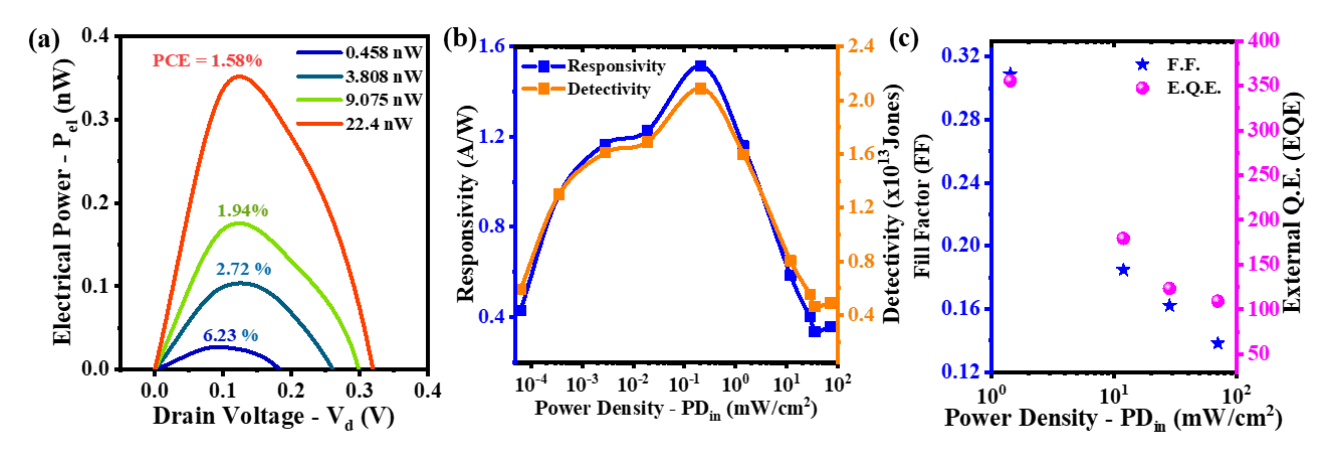


Figure 55. (a) PCE of the Gr-GaS-WSe₂ devices. (b) Responsivity and detectivity of the device. (c) Fill factor and EQE of the device.

Along with responsivity, external quantum efficiency (EQE) is an important bench marking parameter for photovoltaic type devices and could be estimated based on the responsivity of the device and illumination wavelength, using equation 13. The estimated EQE of the photodiode at 405nm illumination at self-biased condition is illustrated in figure 55c. The device shows an excellent EQE evolution, with maximum value of greater than 350% at $\sim 1 \text{mW/cm}^2$ and as illumination intensity is increased, the value drops to 100% at high intensity. Moreover, for competitive performance comparison, the fill factor (FF) of our device was also obtained. FF is a measure of solar cell quality, indicating how closely the actual maximum output power follows the theoretical maximum value for the device and could be obtained using equation 14.

The FF of our device has been presented in figure 55c with varied illumination intensity. Our device exhibits a value of 0.32 at $\sim 1 \text{mW/cm}^2$ and with increasing input power density, it reaches to less than 0.13 at 70 mW/cm² suggesting the device has further scope of improvement for solar cell performance applications.



5.3. Conclusion

While significant attention is dedicated to engineering new vdW-m for ultra-fast, high-efficiency photodetection technologies, equal emphasis should be placed on addressing the existing bottlenecks that hinder the overall performance of currently available vdW-m. By alleviating these limitations, we can better harness the maximum potential of these materials and enhance their effectiveness in practical applications.

On this note, we believe renewed thinking is necessary on how an optimization of photodiode should be performed, especially when it involves moderately wide bandgap semiconductors such as GaS in the heterojunction. We explored and identified key performance enhancement processes for vdW photodiodes. vdW-MC enhances carrier extraction significantly, since most of the traps associated with devices were identified to be at the contact region. Device performance can be further enhanced by tuning thickness of layers to achieve a robust p-n junction that can promote a balance between photogeneration, recombination and extraction.

Hence, a bottom-up pyramid approach is necessary where the first step of optimization should involve careful contact integration strategy to minimize FLP, with a second step of structural optimization of the device to include enhanced photocarrier transportation. The final step should include extracting maximum efficiency of the p-n junction by tuning the thickness of the constituent layers. These steps will ensure a recombination resilient metal-vdW-m interface, striking a favorable balance among photocarrier generation-recombination, separation, transport, and extraction, eventually facilitating a highly sensitive, broadband photodiode.

The conclusions from this work challenge the traditional direct metal deposition for contact integration strategy and support significant advancements in vdW-m photodiodes, especially for reduction in device-to-device variations for industrial scale applications, initiating



alternative research in metal contact integration methods and synergistic multifactorial approach to device optimization.



Appendix:

A1: Supplementary Characterization for a-vdW GaS-WSe2 photodiode:

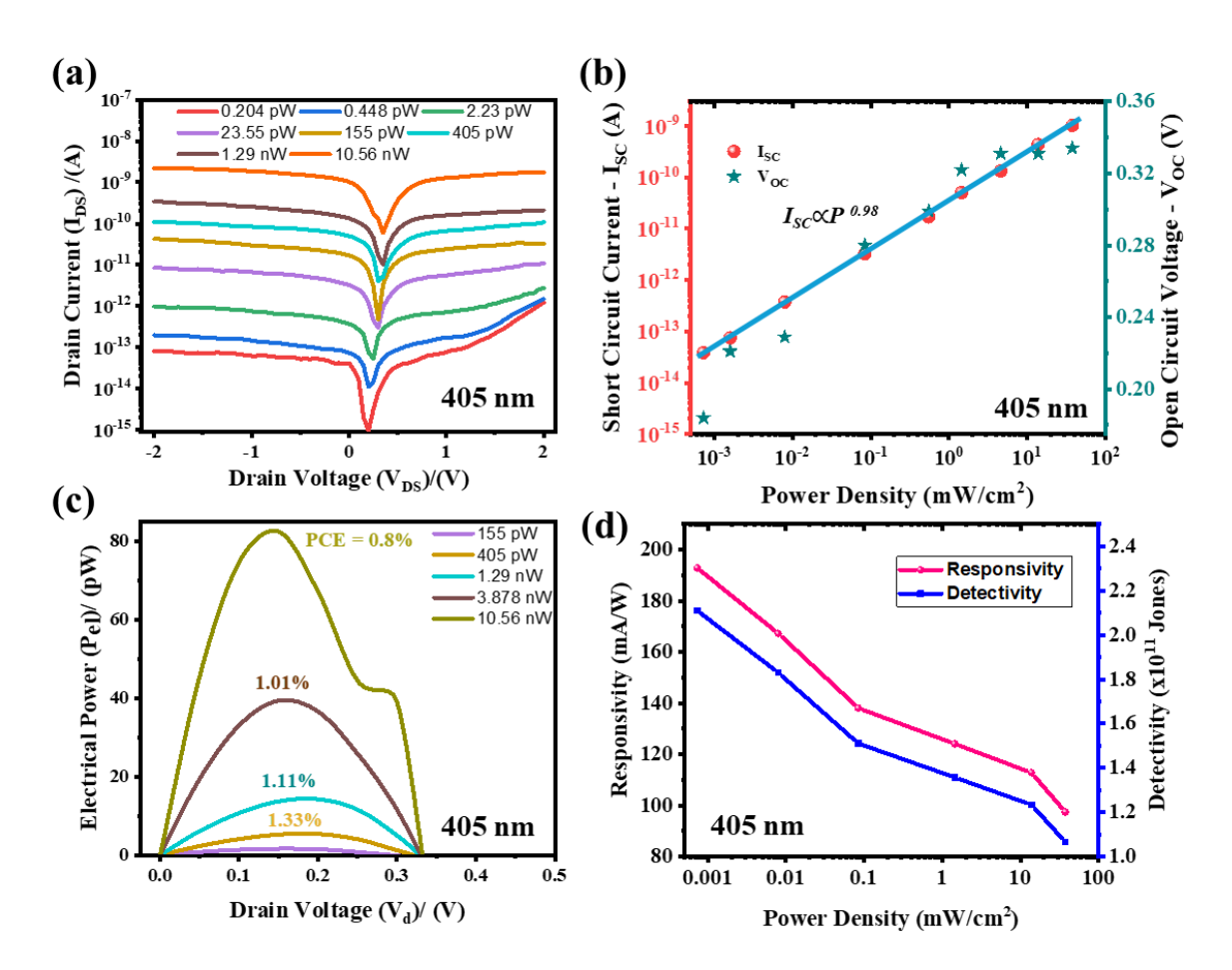


Figure 56. (a) I_d - V_d plot (b) Double log plot of I_{SC} vs PD_{in} showing power exponent (a) (c) Optoelectronic power conversion characteristics and (d) Responsivity and Detectivity of device-1 at 405nm illumination



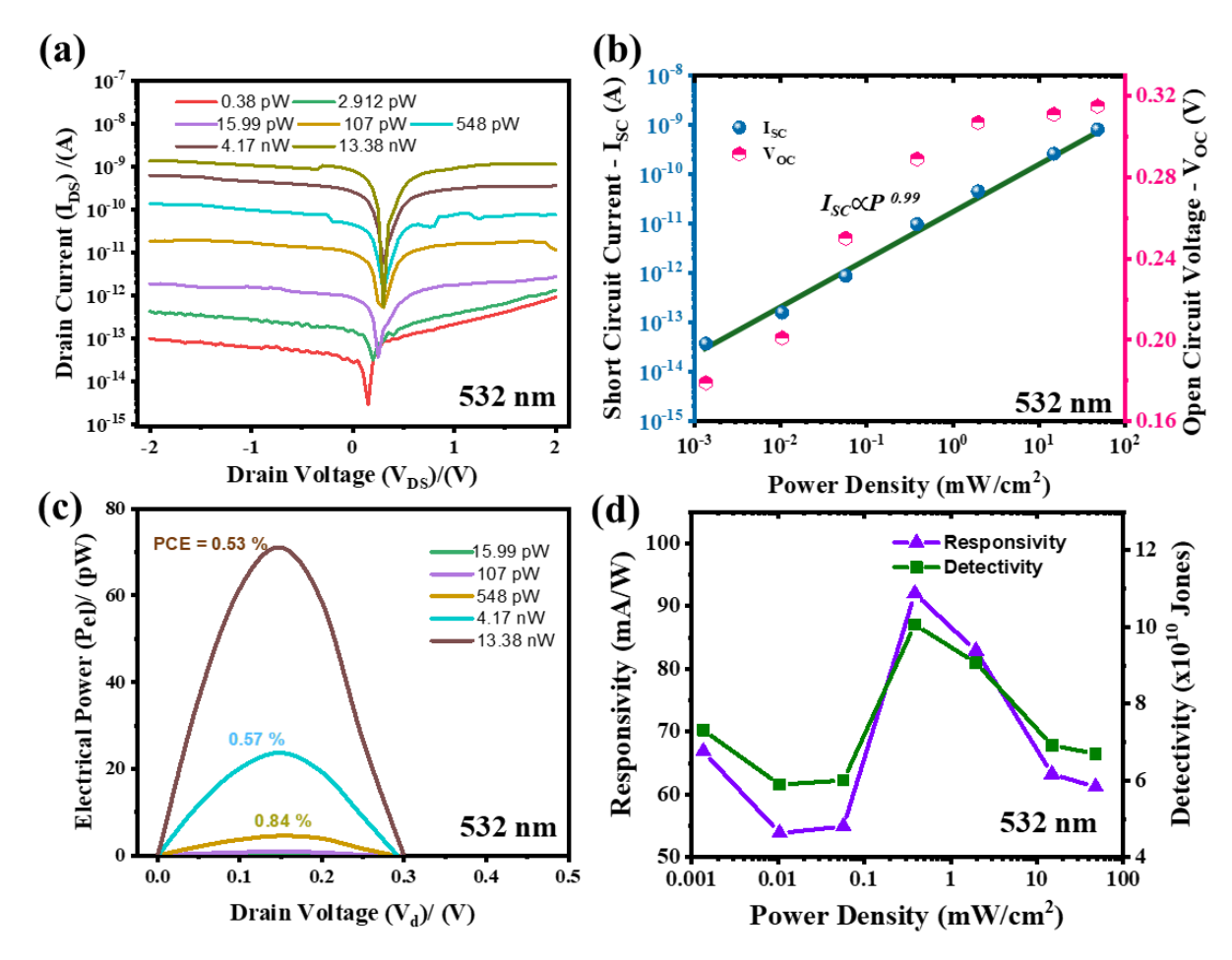


Figure 57.(a) I_d - V_d plot (b) Double log plot of I_{SC} vs PD_{in} showing power exponent (a) (c) Optoelectronic power conversion characteristics and (d) Responsivity and Detectivity of device-1 at 532nm illumination.



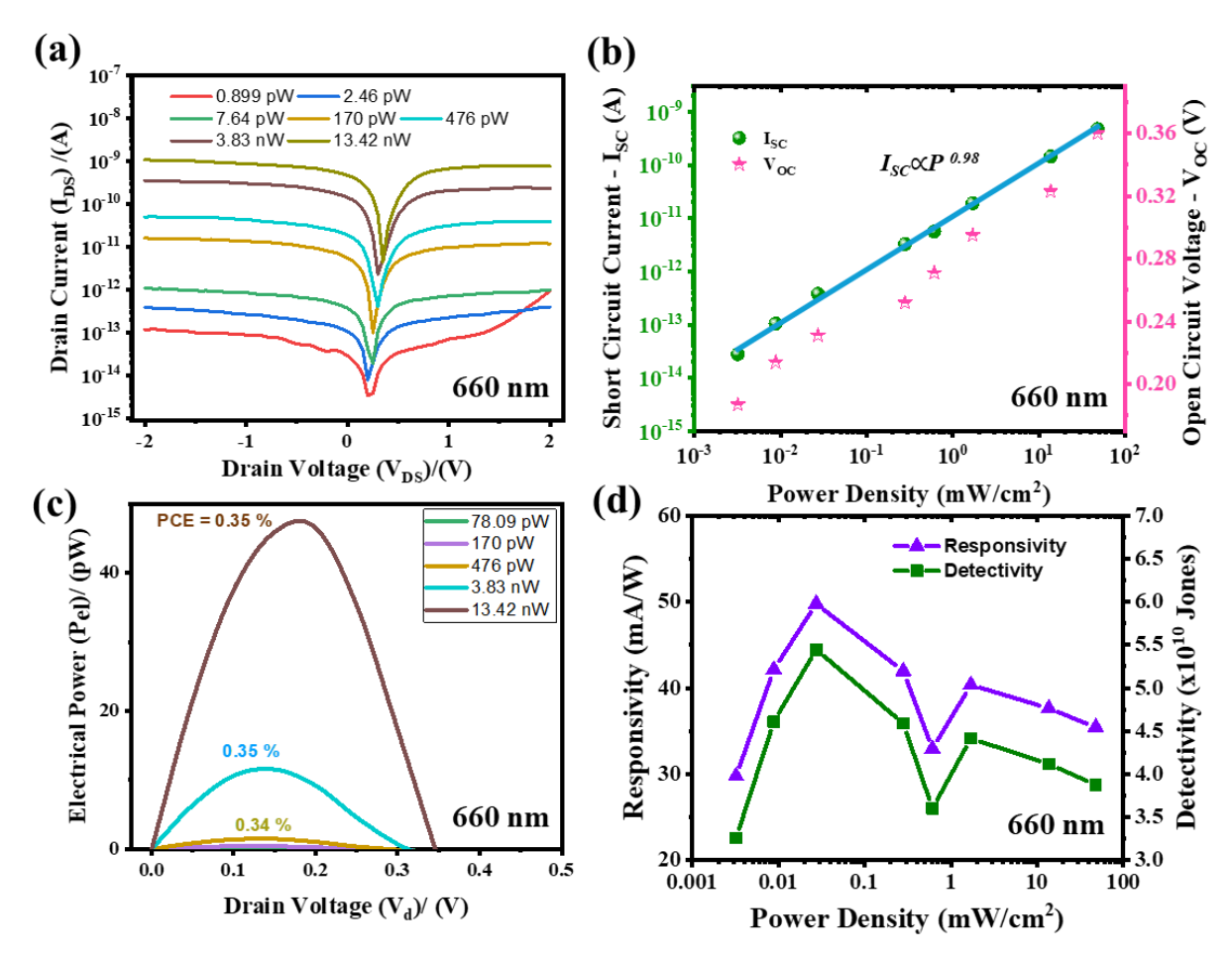


Figure 58. (a) I_d - V_d plot (b) Double log plot of I_{SC} vs PD_{in} showing power exponent (a) (c) Optoelectronic power conversion characteristics and (d) Responsivity and Detectivity of device-1 at 660nm illumination.



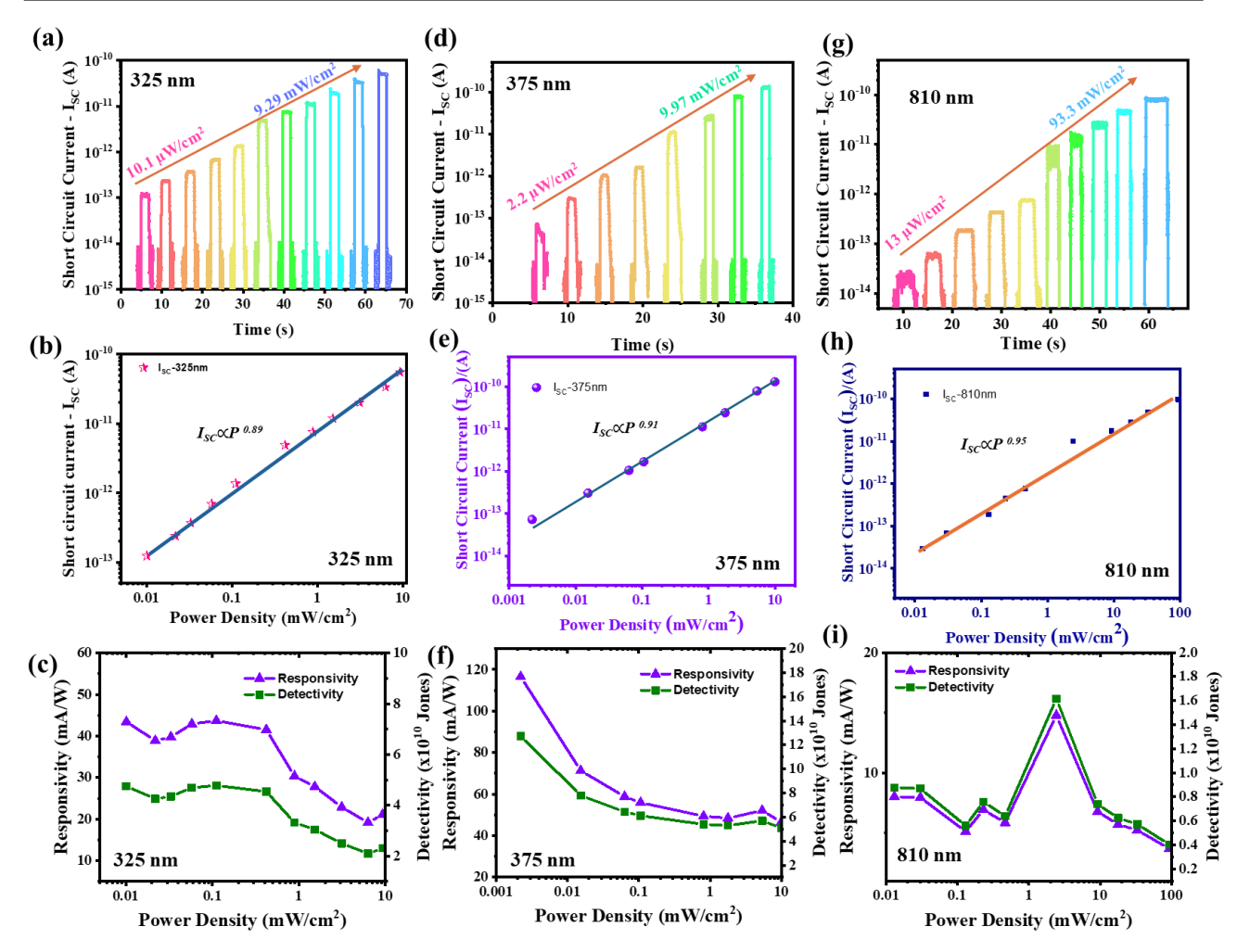


Figure 59. (a) Temporal response of the device under varied illumination intensity (b) double $log I_{SC}$ vs PD_{in} (c) Responsivity and Detectivity vs $log PD_{in}$ at 325nm. (d) Temporal response of the device under varied illumination intensity (e) double $log I_{SC}$ vs PD_{in} (f) Responsivity and Detectivity vs $log PD_{in}$ at 375nm. (g) Temporal response of the device under varied illumination intensity (h) double $log I_{SC}$ vs PD_{in} (i) Responsivity and Detectivity vs $log PD_{in}$ at 810nm. (Device-1)



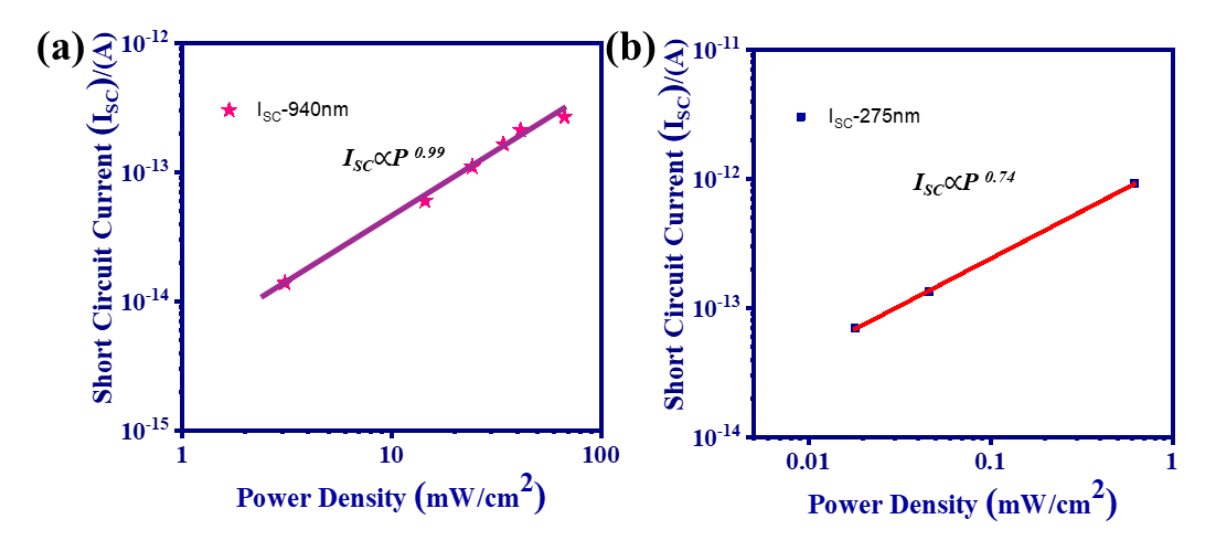


Figure 60. (a) double $\log I_{SC}$ vs PD_{in} at 940nm illumination (b) double $\log I_{SC}$ vs PD_{in} at 275nm illumination (Device-1)

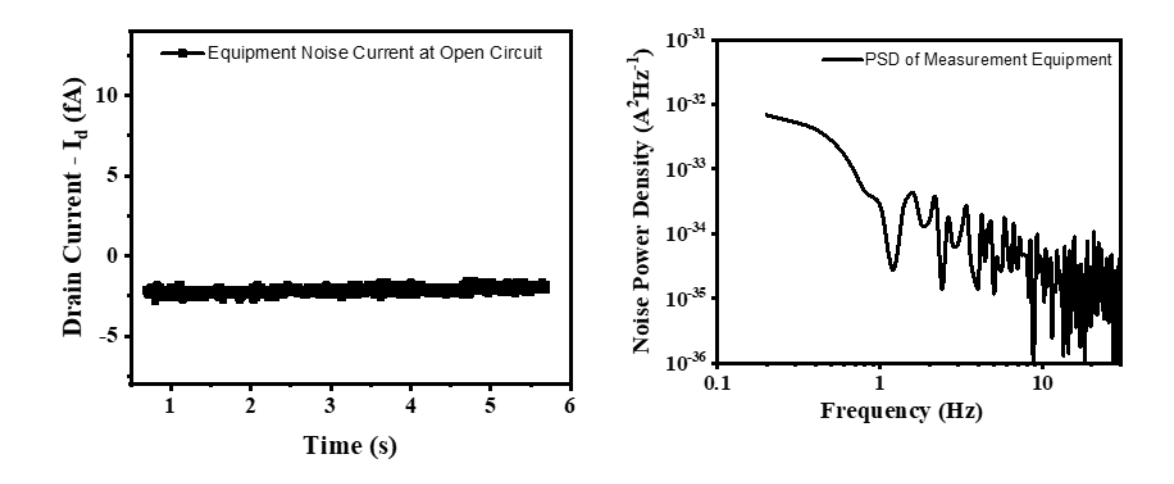


Figure 61. Noise measurement of Instrument at Open circuit. (a) Dark current trace for 5 seconds (b) Corresponding PSD of the instrument at open circuit.



References

- [1] K.S. Novoselov, A.K. Geim, S. V Morozov, D. Jiang, Y. Zhang, S. V Dubonos, I. V Grigorieva, A.A. Firsov, Electric Field Effect in Atomically Thin Carbon Films, Science 306 (2004) 666–669. https://doi.org/10.1126/science.1102896.
- [2] M.C. Lemme, D. Akinwande, C. Huyghebaert, C. Stampfer, 2D materials for future heterogeneous electronics, Nat. Commun. 13 (2022) 1392. https://doi.org/10.1038/s41467-022-29001-4.
- [3] X. Huang, C. Liu, P. Zhou, 2D semiconductors for specific electronic applications: From device to system, NPJ 2D Mater. Appl. 6 (2022) 51. https://doi.org/10.1038/s41699-022-00327-3.
- [4] Y.Y. Illarionov, T. Knobloch, M. Jech, M. Lanza, D. Akinwande, M.I. Vexler, T. Mueller, M.C. Lemme, G. Fiori, F. Schwierz, T. Grasser, Insulators for 2D nanoelectronics: the gap to bridge, Nat. Commun. 11 (2020) 3385. https://doi.org/10.1038/s41467-020-16640-8.
- [5] Y.Y. Illarionov, A.G. Banshchikov, D.K. Polyushkin, S. Wachter, T. Knobloch, M. Thesberg, L. Mennel, M. Paur, M. Stöger-Pollach, A. Steiger-Thirsfeld, M.I. Vexler, M. Waltl, N.S. Sokolov, T. Mueller, T. Grasser, Ultrathin calcium fluoride insulators for two-dimensional field-effect transistors, Nat. Electron. 2 (2019) 230–235. https://doi.org/10.1038/s41928-019-0256-8.
- [6] D. Qiu, C. Gong, S.S. Wang, M. Zhang, C. Yang, X. Wang, J. Xiong, Recent Advances in 2D Superconductors, Adv. Mater. 33 (2021) 2006124. https://doi.org/10.1002/adma.202006124.



- [7] J. Li, P. Song, J. Zhao, K. Vaklinova, X. Zhao, Z. Li, Z. Qiu, Z. Wang, L. Lin, M. Zhao, T.S. Herng, Y. Zuo, W. Jonhson, W. Yu, X. Hai, P. Lyu, H. Xu, H. Yang, C. Chen, S.J. Pennycook, J. Ding, J. Teng, A.H. Castro Neto, K.S. Novoselov, J. Lu, Printable two-dimensional superconducting monolayers, Nat. Mater. 20 (2021) 181–187. https://doi.org/10.1038/s41563-020-00831-1.
- [8] S.N. Kajale, T. Nguyen, C.A. Chao, D.C. Bono, A. Boonkird, M. Li, D. Sarkar, Current-induced switching of a van der Waals ferromagnet at room temperature, Nat. Commun. 15 (2024) 1485. https://doi.org/10.1038/s41467-024-45586-4.
- [9] M. Gibertini, M. Koperski, A.F. Morpurgo, K.S. Novoselov, Magnetic 2D materials and heterostructures, Nat. Nanotechnol. 14 (2019) 408–419. https://doi.org/10.1038/s41565-019-0438-6.
- [10] K. Kang, S. Xie, L. Huang, Y. Han, P.Y. Huang, K.F. Mak, C.J. Kim, D. Muller, J. Park, High-mobility three-atom-thick semiconducting films with wafer-scale homogeneity, Nature 520 (2015) 656–660. https://doi.org/10.1038/nature14417.
- [11] L. Xu, W. Cai, Y. Jia, R. Xing, T. Han, B. Zhang, C. Wang, Graphene–Silicon Hybrid MOSFET Integrated Circuits for High-Linearity Analog Amplification, IEEE Electron Device Letters 43 (2022) 1886–1889. https://doi.org/10.1109/LED.2022.3204950.
- [12] G. Migliato Marega, Y. Zhao, A. Avsar, Z. Wang, M. Tripathi, A. Radenovic, A. Kis, Logic-in-memory based on an atomically thin semiconductor, Nature 587 (2020) 72–77. https://doi.org/10.1038/s41586-020-2861-0.
- [13] T. Dai, C. Chen, L. Huang, J. Jiang, L.M. Peng, Z. Zhang, Ultrasensitive Magnetic Sensors Enabled by Heterogeneous Integration of Graphene Hall Elements and Silicon Processing Circuits, ACS Nano 14 (2020) 17606–17614. https://doi.org/10.1021/acsnano.0c08435.



- [14] S.K. Hong, C.S. Kim, W.S. Hwang, B.J. Cho, Hybrid Integration of Graphene Analog and Silicon Complementary Metal-Oxide-Semiconductor Digital Circuits, ACS Nano 10 (2016) 7142–7146. https://doi.org/10.1021/acsnano.6b03382.
- [15] B. Peng, G. Yu, X. Liu, B. Liu, X. Liang, L. Bi, L. Deng, T.C. Sum, K.P. Loh, Ultrafast charge transfer in MoS₂/WSe₂ p-n Heterojunction, 2d Mater. 3 (2016) 025020. https://doi.org/10.1088/2053-1583/3/2/025020.
- [16] M. Bernardi, M. Palummo, J.C. Grossman, Extraordinary sunlight absorption and one nanometer thick photovoltaics using two-dimensional monolayer materials, Nano Lett. 13 (2013) 3664–3670. https://doi.org/10.1021/nl401544y.
- [17] B. Liu, X. Zhang, J. Du, J. Xiao, H. Yu, M. Hong, L. Gao, Y. Ou, Z. Kang, Q. Liao, Z. Zhang, Y. Zhang, Synergistic-engineered van der Waals photodiodes with high efficiency, InfoMat 4 (2022) e12282. https://doi.org/10.1002/inf2.12282.
- [18] P. V. Pham, S.C. Bodepudi, K. Shehzad, Y. Liu, Y. Xu, B. Yu, X. Duan, 2D Heterostructures for Ubiquitous Electronics and Optoelectronics: Principles, Opportunities, and Challenges, Chem. Rev. 122 (2022) 6514–6613. https://doi.org/10.1021/acs.chemrev.1c00735.
- [19] T.I. Alam, K. Liu, S.U. Hani, S. Ahmed, Y.H. Tsang, Advances in Group-10 Transition Metal Dichalcogenide PdSe₂-Based Photodetectors: Outlook and Perspectives, Sensors 24 (2024) 6127. https://doi.org/10.3390/s24186127.
- [20] M. Samadi, N. Sarikhani, M. Zirak, H. Zhang, H.L. Zhang, A.Z. Moshfegh, Group 6 transition metal dichalcogenide nanomaterials: Synthesis, applications and future perspectives, Nanoscale Horiz. 3 (2018) 90–204. https://doi.org/10.1039/c7nh00137a.



- [21] C.H. Lee, G.H. Lee, A.M. Van Der Zande, W. Chen, Y. Li, M. Han, X. Cui, G. Arefe, C. Nuckolls, T.F. Heinz, J. Guo, J. Hone, P. Kim, Atomically thin p-n junctions with van der Waals heterointerfaces, Nat. Nanotechnol. 9 (2014) 676–681. https://doi.org/10.1038/nnano.2014.150.
- [22] X. Liu, G. Sun, P. Chen, J. Liu, Z. Zhang, J. Li, H. Ma, B. Zhao, R. Wu, W. Dang, X. Yang, C. Dai, X. Tang, Z. Chen, L. Miao, X. Liu, B. Li, Y. Liu, X. Duan, High-performance asymmetric electrodes photodiode based on Sb/WSe₂ heterostructure, Nano Res. 12 (2019) 339–344. https://doi.org/10.1007/s12274-018-2220-8.
- [23] Q. Lv, F. Yan, X. Wei, K. Wang, High-Performance, Self-Driven Photodetector Based on Graphene Sandwiched GaSe/WS₂ Heterojunction, Adv. Opt. Mater. 6 (2018) 1700490. https://doi.org/10.1002/adom.201700490.
- [24] S. Jia, Z. Jin, J. Zhang, J. Yuan, W. Chen, W. Feng, P. Hu, P.M. Ajayan, J. Lou, Lateral Monolayer MoSe₂–WSe₂ p–n Heterojunctions with Giant Built-In Potentials, Small 16 (2020) 2002263. https://doi.org/10.1002/sml1.202002263.
- [25] M.S. Choi, D. Qu, D. Lee, X. Liu, K. Watanabe, T. Taniguchi, W.J. Yoo, Lateral MoS₂ p-n junction formed by chemical doping for use in high-performance optoelectronics, ACS Nano 8 (2014) 9332–9340. https://doi.org/10.1021/nn503284n.
- [26] J.K. Kim, K. Cho, J. Jang, K.Y. Baek, J. Kim, J. Seo, M. Song, J. Shin, J. Kim, S.S.P. Parkin, J.H. Lee, K. Kang, T. Lee, Molecular Dopant-Dependent Charge Transport in Surface-Charge-Transfer-Doped Tungsten Diselenide Field Effect Transistors, Adv. Mater. 33 (2021) 2101598. https://doi.org/10.1002/adma.202101598.
- [27] X. Wei, F. Yan, Q. Lv, W. Zhu, C. Hu, A. Patanè, K. Wang, Enhanced Photoresponse in MoTe₂ Photodetectors with Asymmetric Graphene Contacts, Adv. Opt. Mater. 7 (2019) 1900190. https://doi.org/10.1002/adom.201900190.



- [28] M. Dai, H. Chen, F. Wang, M. Long, H. Shang, Y. Hu, W. Li, C. Ge, J. Zhang, T. Zhai, Y. Fu, P. Hu, Ultrafast and Sensitive Self-Powered Photodetector Featuring Self-Limited Depletion Region and Fully Depleted Channel with van der Waals Contacts, ACS Nano 14 (2020) 9098–9106. https://doi.org/10.1021/acsnano.0c04329.
- [29] Z. Qi, T. Yang, D. Li, H. Li, X. Wang, X. Zhang, F. Li, W. Zheng, P. Fan, X. Zhuang, A. Pan, High-responsivity two-dimensional p-PbI₂/n-WS₂ vertical heterostructure photodetectors enhanced by photogating effect, Mater. Horiz. 6 (2019) 1474–1480. https://doi.org/10.1039/c9mh00335e.
- [30] S. Quan, L. Li, S. Guo, X. Zhao, D. Weller, X. Wang, S. Fu, R. Liu, Y. Hao, SnS₂/MoS₂ van der Waals Heterostructure Photodetector with Ultrahigh Responsivity Realized by a Photogating Effect, ACS Appl. Mater. Interfaces 15 (2023) 59592–59599. https://doi.org/10.1021/acsami.3c13004.
- [31] W.L. Chow, P. Yu, F. Liu, J. Hong, X. Wang, Q. Zeng, C.H. Hsu, C. Zhu, J. Zhou, X. Wang, J. Xia, J. Yan, Y. Chen, D. Wu, T. Yu, Z. Shen, H. Lin, C. Jin, B.K. Tay, Z. Liu, High Mobility 2D Palladium Diselenide Field-Effect Transistors with Tunable Ambipolar Characteristics, Adv. Mater. 29 (2017) 1602969. https://doi.org/10.1002/adma.201602969.
- [32] T. Lei, H. Tu, W. Lv, H. Ma, J. Wang, R. Hu, Q. Wang, L. Zhang, B. Fang, Z. Liu, W. Shi, Z. Zeng, Ambipolar Photoresponsivity in an Ultrasensitive Photodetector Based on a WSe2/InSe Heterostructure by a Photogating Effect, ACS Appl. Mater. Interfaces 13 (2021) 50213–50219. https://doi.org/10.1021/acsami.1c12330.
- [33] H. Jiang, J. Wei, F. Sun, C. Nie, J. Fu, H. Shi, J. Sun, X. Wei, C.W. Qiu, Enhanced Photogating Effect in Graphene Photodetectors via Potential Fluctuation Engineering, ACS Nano 16 (2022) 4458–4466. https://doi.org/10.1021/acsnano.1c10795.



- [34] K. Zhang, M. Peng, A. Yu, Y. Fan, J. Zhai, Z.L. Wang, A substrate-enhanced MoS₂ photodetector through a dual-photogating effect, Mater. Horiz. 6 (2019) 826–833. https://doi.org/10.1039/c8mh01429a.
- [35] L. Viti, J. Hu, D. Coquillat, W. Knap, A. Tredicucci, A. Politano, M.S. Vitiello, Black Phosphorus Terahertz Photodetectors, Adv. Mater. 27 (2015) 5567–5572. https://doi.org/10.1002/adma.201502052.
- [36] L. Viti, A. Politano, K. Zhang, M.S. Vitiello, Thermoelectric terahertz photodetectors based on selenium-doped black phosphorus flakes, Nanoscale 11 (2019) 1995–2002. https://doi.org/10.1039/c8nr09060b.
- [37] H. Morkoç, S. Strite, G.B. Gao, M.E. Lin, B. Sverdlov, M. Burns, Large-band-gap SiC, III-V nitride, and II-VI ZnSe-based semiconductor device technologies, J Appl. Phys. 76 (1994) 1363–1398. https://doi.org/10.1063/1.358463.
- [38] Y. Wang, M. Chhowalla, Making clean electrical contacts on 2D transition metal dichalcogenides, Nat. Rev. Phy. 4 (2022) 101–112. https://doi.org/10.1038/s42254-021-00389-0.
- [39] A. Allain, J. Kang, K. Banerjee, A. Kis, Electrical contacts to two-dimensional semiconductors, Nat. Mater. 14 (2015) 1195–1205. https://doi.org/10.1038/nmat4452.
- [40] D. Jena, K. Banerjee, H.X. Grace, Intimate Contacts, Nat. Mater. 13 (2014) 1076–1078. https://doi.org/https://doi.org/10.1038/nmat4121.
- [41] L. Wang, I. Meric, P.Y. Huang, Q. Gao, Y. Gao, H. Tran, T. Taniguchi, K. Watanabe, L.M. Campos, D.A. Muller, J. Guo, P. Kim, J. Hone, K.L. Shepard, C.R. Dean, One-dimensional electrical contact to a two-dimensional material, Science 342 (2013) 614–617. https://doi.org/10.1126/science.1244358.



- [42] N. Shetty, H. He, R. Mitra, J. Huhtasaari, K. Iordanidou, J. Wiktor, S. Kubatkin, S.P. Dash, R. Yakimova, L. Zeng, E. Olsson, S. Lara-Avila, Scalable Fabrication of Edge Contacts to 2D Materials: Implications for Quantum Resistance Metrology and 2D Electronics, ACS Appl. Nano Mater. 6 (2023) 6292–6298. https://doi.org/10.1021/acsanm.3c00652.
- [43] M.H.D. Guimarães, H. Gao, Y. Han, K. Kang, S. Xie, C.J. Kim, D.A. Muller, D.C. Ralph, J. Park, Atomically Thin Ohmic Edge Contacts between Two-Dimensional Materials, ACS Nano 10 (2016) 6392–6399. https://doi.org/10.1021/acsnano.6b02879.
- [44] L.Y. Gan, Y.J. Zhao, D. Huang, U. Schwingenschlögl, First-principles analysis of MoS₂/Ti₂C and MoS₂/Ti₂CY₂ (Y=F and OH) all-2D semiconductor/metal contacts, Phys. Rev. B Condens. Matter. Mater. Phys. 87 (2013) 245307. https://doi.org/10.1103/PhysRevB.87.245307.
- [45] W.S. Leong, C.T. Nai, J.T.L. Thong, What does annealing do to metal-graphene contacts?, Nano Lett. 14 (2014) 3840–3847. https://doi.org/10.1021/nl500999r.
- [46] Y. Liu, P. Stradins, S.H. Wei, Van der Waals metal-semiconductor junction: Weak Fermi level pinning enables effective tuning of Schottky barrier, Sci. Adv. 2 (2016) e1600069. https://doi.org/10.1126/sciadv.1600069.
- [47] X. Liu, M.S. Choi, E. Hwang, W.J. Yoo, J. Sun, Fermi Level Pinning Dependent 2D Semiconductor Devices: Challenges and Prospects, Adv. Mater. 34 (2022) 2108425. https://doi.org/10.1002/adma.202108425.
- [48] J. Wang, Q. Yao, C.W. Huang, X. Zou, L. Liao, S. Chen, Z. Fan, K. Zhang, W. Wu, X. Xiao, C. Jiang, W.W. Wu, High Mobility MoS₂ Transistor with Low Schottky Barrier Contact by Using Atomic Thick h-BN as a Tunneling Layer, Adv. Mater. 28 (2016) 8302–8308. https://doi.org/10.1002/adma.201602757.



- [49] X. Cui, E.M. Shih, L.A. Jauregui, S.H. Chae, Y.D. Kim, B. Li, D. Seo, K. Pistunova, J. Yin, J.H. Park, H.J. Choi, Y.H. Lee, K. Watanabe, T. Taniguchi, P. Kim, C.R. Dean, J.C. Hone, Low temperature Ohmic Contact to Monolayer MoS₂ by van der Waals Bonded Co/h-BN Electrodes, Nano Lett. 17 (2017) 4781–4786. https://doi.org/10.1021/acs.nanolett.7b01536.
- [50] X.X. Li, Z.Q. Fan, P.Z. Liu, M.L. Chen, X. Liu, C.K. Jia, D.M. Sun, X.W. Jiang, Z. Han, V. Bouchiat, J.J. Guo, J.H. Chen, Z.D. Zhang, Gate-controlled reversible rectifying behaviour in tunnel contacted atomically-thin MoS₂ transistor, Nat. Commun. 8 (2017) 970. https://doi.org/10.1038/s41467-017-01128-9.
- [51] A. Dankert, L. Langouche, M.V. Kamalakar, S.P. Dash, High-performance molybdenum disulfide field-effect transistors with spin tunnel contacts, ACS Nano 8 (2014) 476–482. https://doi.org/10.1021/nn404961e.
- [52] M. Venkata Kamalakar, B.N. Madhushankar, A. Dankert, S.P. Dash, Low schottky barrier black phosphorus field-effect devices with ferromagnetic tunnel contacts, Small 11 (2015) 2209–2216. https://doi.org/10.1002/smll.201402900.
- [53] N. Kaushik, D. Karmakar, A. Nipane, S. Karande, S. Lodha, Interfacial n-Doping Using an Ultrathin TiO2 Layer for Contact Resistance Reduction in MoS₂, ACS Appl. Mater. Interfaces 8 (2016) 256–263. https://doi.org/10.1021/acsami.5b08559.
- [54] J. Cheng, J. He, C. Pu, C. Liu, X. Huang, D. Zhang, H. Yan, P.K. Chu, MoS₂ Transistors with Low Schottky Barrier Contact by Optimizing the Interfacial Layer Thickness, Energies (Basel) 15 (2022) 6169. https://doi.org/10.3390/en15176169.
- [55] W. Wang, Y. Liu, L. Tang, Y. Jin, T. Zhao, F. Xiu, Controllable Schottky barriers between MoS₂ and permalloy, Sci. Rep. 4 (2014) 6928. https://doi.org/10.1038/srep06928.



- [56] S. Zheng, H. Lu, H. Liu, D. Liu, J. Robertson, Insertion of an ultrathin Al₂O₃ interfacial layer for Schottky barrier height reduction in WS₂ field-effect transistors, Nanoscale 11 (2019) 4811–4821. https://doi.org/10.1039/c8nr07812b.
- [57] Y. Liu, J. Guo, E. Zhu, L. Liao, S.J. Lee, M. Ding, I. Shakir, V. Gambin, Y. Huang, X. Duan, Approaching the Schottky-Mott limit in van der Waals metal-semiconductor junctions, Nature 557 (2018) 696–700. https://doi.org/10.1038/s41586-018-0129-8.
- [58] X. Zhang, Z. Kang, L. Gao, B. Liu, H. Yu, Q. Liao, Z. Zhang, Y. Zhang, Molecule-Upgraded van der Waals Contacts for Schottky-Barrier-Free Electronics, Adv. Mater. 33 (2021) 2104935. https://doi.org/10.1002/adma.202104935.
- [59] C.M. Went, J. Wong, P.R. Jahelka, M. Kelzenberg, S. Biswas, M.S. Hunt, A. Carbone, H.A. Atwater, A new metal transfer process for van der Waals contacts to vertical Schottky-junction transition metal dichalcogenide photovoltaics, Sci. Adv. 5 (2019) eaax6061. https://www.science.org.
- [60] L. Liu, L. Kong, Q. Li, C. He, L. Ren, Q. Tao, X. Yang, J. Lin, B. Zhao, Z. Li, Y. Chen, W. Li, W. Song, Z. Lu, G. Li, S. Li, X. Duan, A. Pan, L. Liao, Y. Liu, Transferred van der Waals metal electrodes for sub-1-nm MoS₂ vertical transistors, Nat. Electron. 4 (2021) 342–347. https://doi.org/10.1038/s41928-021-00566-0.
- [61] L. Kong, X. Zhang, Q. Tao, M. Zhang, W. Dang, Z. Li, L. Feng, L. Liao, X. Duan, Y. Liu, Doping-free complementary WSe₂ circuit via van der Waals metal integration, Nat. Commun. 11 (2020) 1866. https://doi.org/10.1038/s41467-020-15776-x.
- [62] Y. Jung, M.S. Choi, A. Nipane, A. Borah, B. Kim, A. Zangiabadi, T. Taniguchi, K. Watanabe, W.J. Yoo, J. Hone, J.T. Teherani, Transferred via contacts as a platform for ideal two-dimensional transistors, Nat. Electron. 2 (2019) 187–194. https://doi.org/10.1038/s41928-019-0245-y.



- [63] G. Kwon, Y.H. Choi, H. Lee, H.S. Kim, J. Jeong, K. Jeong, M. Baik, H. Kwon, J. Ahn, E. Lee, M.H. Cho, Interaction- and defect-free van der Waals contacts between metals and two-dimensional semiconductors, Nat. Electron. 5 (2022) 241–247. https://doi.org/10.1038/s41928-022-00746-6.
- [64] L. Kong, R. Wu, Y. Chen, Y. Huangfu, L. Liu, W. Li, D. Lu, Q. Tao, W. Song, W. Li, Z. Lu, X. Liu, Y. Li, Z. Li, W. Tong, S. Ding, S. Liu, L. Ma, L. Ren, Y. Wang, L. Liao, X. Duan, Y. Liu, Wafer-scale and universal van der Waals metal semiconductor contact, Nat. Commun. 14 (2023) 1014. https://doi.org/10.1038/s41467-023-36715-6.
- [65] Y. Wang, J.C. Kim, R.J. Wu, J. Martinez, X. Song, J. Yang, F. Zhao, A. Mkhoyan, H.Y. Jeong, M. Chhowalla, Van der Waals contacts between three-dimensional metals and two-dimensional semiconductors, Nature 568 (2019) 70–74. https://doi.org/10.1038/s41586-019-1052-3.
- [66] J. Bullock, M. Amani, J. Cho, Y.Z. Chen, G.H. Ahn, V. Adinolfi, V.R. Shrestha, Y. Gao, K.B. Crozier, Y.L. Chueh, Polarization-resolved A. Javey, black phosphorus/molybdenum disulfide mid-wave infrared photodiodes with high detectivity (2018)at room temperature, Nat. Photonics. 12 601-607. https://doi.org/10.1038/s41566-018-0239-8.
- [67] M. Long, Y. Wang, P. Wang, X. Zhou, H. Xia, C. Luo, S. Huang, G. Zhang, H. Yan, Z. Fan, X. Wu, X. Chen, W. Lu, W. Hu, Palladium diselenide long-wavelength infrared photodetector with high sensitivity and stability, ACS Nano 13 (2019) 2511–2519. https://doi.org/10.1021/acsnano.8b09476.
- [68] S. Cakmakyapan, P.K. Lu, A. Navabi, M. Jarrahi, Gold-patched graphene nano-stripes for high-responsivity and ultrafast photodetection from the visible to infrared regime, Light Sci. Appl. 7 (2018) 20. https://doi.org/10.1038/s41377-018-0020-2.



- [69] M. Amani, E. Regan, J. Bullock, G.H. Ahn, A. Javey, Mid-Wave Infrared Photoconductors Based on Black Phosphorus-Arsenic Alloys, ACS Nano 11 (2017) 11724–11731. https://doi.org/10.1021/acsnano.7b07028.
- [70] L. Tong, X. Huang, P. Wang, L. Ye, M. Peng, L. An, Q. Sun, Y. Zhang, G. Yang, Z. Li, F. Zhong, F. Wang, Y. Wang, M. Motlag, W. Wu, G.J. Cheng, W. Hu, Stable mid-infrared polarization imaging based on quasi-2D tellurium at room temperature, Nat. Commun. 11 (2020) 2308. https://doi.org/10.1038/s41467-020-16125-8.
- [71] A. Rogalski, HgCdTe infrared detector material: History, status and outlook, Reports on Progress in Physics 68 (2005) 2267–2336. https://doi.org/10.1088/0034-4885/68/10/R01.
- [72] A. Rogalski, Infrared detectors: status and trends, Prog Quantum Electron 27 (2003) 59–210.
- [73] J. Jiang, T. Xu, J. Lu, L. Sun, Z. Ni, Defect Engineering in 2D Materials: Precise Manipulation and Improved Functionalities, Research 2019 (2019) 4641739. https://doi.org/10.34133/2019/4641739.
- [74] Z. Hu, Z. Wu, C. Han, J. He, Z. Ni, W. Chen, Two-dimensional transition metal dichalcogenides: Interface and defect engineering, Chem. Soc. Rev. 47 (2018) 3100– 3128. https://doi.org/10.1039/c8cs00024g.
- [75] M. Zhou, W. Wang, J. Lu, Z. Ni, How defects influence the photoluminescence of TMDCs, Nano Res. 14 (2021) 29–39. https://doi.org/10.1007/s12274-020-3037-9.
- [76] B.K. Jung, H.K. Woo, C. Shin, T. Park, N. Li, K.J. Lee, W. Kim, J.H. Bae, J.P. Ahn, T.N. Ng, S.J. Oh, Suppressing the Dark Current in Quantum Dot Infrared Photodetectors by



- Controlling Carrier Statistics, Adv. Opt. Mater. 10 (2022) 2101611. https://doi.org/10.1002/adom.202101611.
- [77] S. Maimon, G.W. Wicks, nBn detector, an infrared detector with reduced dark current and higher operating temperature, Appl. Phys. Lett. 89 (2006) 151109. https://doi.org/10.1063/1.2360235.
- [78] M.A. Kinch, Fundamental physics of infrared detector materials, J. Electron. Mater. 29(2000) 809–817.
- [79] H. Son, J. Lee, T.H. Kim, S. Choi, H. Choi, Y.H. Kim, S. Lee, Emergence of multiple negative differential transconductance from a WSe₂ double lateral homojunction platform, Appl. Surf. Sci. 581 (2022) 152396. https://doi.org/10.1016/j.apsusc.2021.152396.
- [80] A. Gao, J. Lai, Y. Wang, Z. Zhu, J. Zeng, G. Yu, N. Wang, W. Chen, T. Cao, W. Hu, D. Sun, X. Chen, F. Miao, Y. Shi, X. Wang, Observation of ballistic avalanche phenomena in nanoscale vertical InSe/BP heterostructures, Nat. Nanotechnol. 14 (2019) 217–222. https://doi.org/10.1038/s41565-018-0348-z.
- [81] A.H. Jones, S.D. March, S.R. Bank, J.C. Campbell, Low-noise high-temperature AlInAsSb/GaSb avalanche photodiodes for 2-µm applications, Nat. Photonics. 14 (2020) 559–563. https://doi.org/10.1038/s41566-020-0637-6.
- [82] J. Xu, X. Luo, X. Lin, X. Zhang, F. Liu, Y. Yan, S. Hu, M. Zhang, N. Han, X. Gan, Y. Cheng, W. Huang, Approaching the Robust Linearity in Dual-Floating van der Waals Photodiode, Adv. Funct. Mater. 34 (2024) 2310811. https://doi.org/10.1002/adfm.202310811.



- [83] Y. Jiang, R. Wang, X. Li, Z. Ma, L. Li, J. Su, Y. Yan, X. Song, C. Xia, Photovoltaic Field-Effect Photodiodes Based on Double van der Waals Heterojunctions, ACS Nano 15 (2021) 14295–14304. https://doi.org/10.1021/acsnano.1c02830.
- [84] P. Luo, F. Wang, J. Qu, K. Liu, X. Hu, K. Liu, T. Zhai, Self-Driven WSe₂/Bi₂O₂Se Van der Waals Heterostructure Photodetectors with High Light On/Off Ratio and Fast Response, Adv. Funct. Mater. 31 (2021) 2008351. https://doi.org/10.1002/adfm.202008351.
- [85] F. Wang, P. Luo, Y. Zhang, Y. Huang, Q. Zhang, Y. Li, T. Zhai, Band structure engineered heterostructures for high-performance visible and near-infrared tunneling photodetection, Sci. China. Mater. 63 (2020)1537–1547. https://doi.org/10.1007/s40843-020-1353-3.
- [86] J. Lee, N.T. Duong, S. Bang, C. Park, D.A. Nguyen, H. Jeon, J. Jang, H.M. Oh, M.S. Jeong, Modulation of Junction Modes in SnSe₂/MoTe₂ Broken-Gap van der Waals Heterostructure for Multifunctional Devices, Nano Lett. 20 (2020) 2370–2377. https://doi.org/10.1021/acs.nanolett.9b04926.
- [87] H. Jiao, X. Wang, Y. Chen, S. Guo, S. Wu, C. Song, S. Huang, X. Huang, X. Tai, T. Lin, H. Shen, H. Yan, W. Hu, X. Meng, J. Chu, Y. Zhang, J. Wang, HgCdTe/black phosphorus van der Waals heterojunction for high-performance polarization-sensitive midwave infrared photodetector, Sci. Adv. 8 (2022) 1811. https://doi.org/10.1126/sciadv.abn1811.
- [88] S. Ghosh, A. Varghese, H. Jawa, Y. Yin, N. V. Medhekar, S. Lodha, Polarity-Tunable Photocurrent through Band Alignment Engineering in a High-Speed WSe₂/SnSe₂ Diode with Large Negative Responsivity, ACS Nano 16 (2022) 4578–4587. https://doi.org/10.1021/acsnano.1c11110.



- [89] H.S. Lee, J.Y. Lim, S. Yu, Y. Jeong, S. Park, K. Oh, S. Hong, S. Yang, C.H. Lee, S. Im, Seamless MoTe₂ Homojunction PIN Diode toward 1300 nm Short-Wave Infrared Detection, Adv. Opt. Mater. 7 (2019) 1900768. https://doi.org/10.1002/adom.201900768.
- [90] X. Wang, P. Wang, J. Wang, W. Hu, X. Zhou, N. Guo, H. Huang, S. Sun, H. Shen, T. Lin, M. Tang, L. Liao, A. Jiang, J. Sun, X. Meng, X. Chen, W. Lu, J. Chu, Ultrasensitive and Broadband MoS₂ Photodetector Driven by Ferroelectrics, Adv. Mater. 27 (2015) 6575–6581. https://doi.org/10.1002/adma.201503340.
- [91] G. Wu, X. Wang, Y. Chen, S. Wu, B. Wu, Y. Jiang, H. Shen, T. Lin, Q. Liu, X. Wang, P. Zhou, S. Zhang, W. Hu, X. Meng, J. Chu, J. Wang, MoTe₂ p—n Homojunctions Defined by Ferroelectric Polarization, Adv. Mater. 32 (2020) 1907937. https://doi.org/10.1002/adma.201907937.
- [92] Y. Chen, X. Wang, L. Huang, X. Wang, W. Jiang, Z. Wang, P. Wang, B. Wu, T. Lin, H. Shen, Z. Wei, W. Hu, X. Meng, J. Chu, J. Wang, Ferroelectric-tuned van der Waals heterojunction with band alignment evolution, Nat. Commun. 12 (2021) 4030. https://doi.org/10.1038/s41467-021-24296-1.
- [93] J.W. Chen, S.T. Lo, S.C. Ho, S.S. Wong, T.H.Y. Vu, X.Q. Zhang, Y. De Liu, Y.Y. Chiou, Y.X. Chen, J.C. Yang, Y.C. Chen, Y.H. Chu, Y.H. Lee, C.J. Chung, T.M. Chen, C.H. Chen, C.L. Wu, A gate-free monolayer WSe₂ p-n diode, Nat. Commun. 9 (2018) 3143. https://doi.org/10.1038/s41467-018-05326-x.
- [94] N. Zarrabi, O.J. Sandberg, S. Zeiske, W. Li, D.B. Riley, P. Meredith, A. Armin, Charge-generating mid-gap trap states define the thermodynamic limit of organic photovoltaic devices, Nat. Commun. 11 (2020) 5567. https://doi.org/10.1038/s41467-020-19434-0.



- [95] O.J. Sandberg, C. Kaiser, S. Zeiske, N. Zarrabi, S. Gielen, W. Maes, K. Vandewal, P. Meredith, A. Armin, Mid-gap trap state-mediated dark current in organic photodiodes, Nat. Photonics. 17 (2023) 368–374. https://doi.org/10.1038/s41566-023-01173-5.
- [96] G. Wang, T. Pang, K. Sun, S. Luan, Y. Zhang, L. Yuan, R. Jia, High-performance layer-structured Si/Ga₂O₃/CH₃NH₃PbI₃ heterojunction photodetector based on a Ga₂O₃ buffer interlayer, Appl. Opt. 62 (2023) A76–A82. https://doi.org/10.1364/AO.472922.
- [97] Q. Zhu, Y. Chen, X. Zhu, Y. Sun, Z. Cheng, J. Xu, M. Xu, High-performance near-infrared PtSe₂/n-Ge heterojunction photodetector with ultrathin Al₂O₃ passivation interlayer, Sci. China. Mater. 66 (2023) 2777–2787. https://doi.org/10.1007/s40843-022-2402-3.
- [98] R. Rojas Delgado, R.M. Jacobberger, S.S. Roy, V.S. Mangu, M.S. Arnold, F. Cavallo, M.G. Lagally, Passivation of Germanium by Graphene, ACS Appl. Mater. Interfaces 9 (2017) 17629–17636. https://doi.org/10.1021/acsami.7b03889.
- [99] B.G. Singidas, A.E. De Los Reyes, H.R. Bardolaza, J.D.E. Vasquez, A.A. Salvador, E.S. Estacio, R. V. Sarmago, Graphene transfer passivates GaAs, Appl. Phys. Lett. 117 (2020) 171105. https://doi.org/10.1063/5.0015145.
- [100] W. Seo, W. Park, H.Y. Seo, S. Oh, O. Kwon, S.H. Jeong, D.H. Kim, M.J. Kim, S.K. Lee, B.H. Lee, B. Cho, MoS₂/p-Si heterojunction with graphene interfacial layer for high performance 940 nm infrared photodetector, Appl. Surf. Sci. 604 (2022) 154485. https://doi.org/10.1016/j.apsusc.2022.154485.
- [101] H. Wang, Z. Li, D. Li, P. Chen, L. Pi, X. Zhou, T. Zhai, Van der Waals Integration Based on Two-Dimensional Materials for High-Performance Infrared Photodetectors, Adv. Funct. Mater. 31 (2021) 2103106. https://doi.org/10.1002/adfm.202103106.



- [102] H. Wang, S. Gao, F. Zhang, F. Meng, Z. Guo, R. Cao, Y. Zeng, J. Zhao, S. Chen, H. Hu, Y.J. Zeng, S.J. Kim, D. Fan, H. Zhang, P.N. Prasad, Repression of Interlayer Recombination by Graphene Generates a Sensitive Nanostructured 2D vdW Heterostructure Based Photodetector, Adv. Sci. 8 (2021) 2100503. https://doi.org/10.1002/advs.202100503.
- [103] D. Wu, J. Guo, C. Wang, X. Ren, Y. Chen, P. Lin, L. Zeng, Z. Shi, X.J. Li, C.X. Shan, J. Jie, Ultrabroadband and High-Detectivity Photodetector Based on WS₂/Ge Heterojunction through Defect Engineering and Interface Passivation, ACS Nano 15 (2021) 10119–10129. https://doi.org/10.1021/acsnano.1c02007.
- [104] M.I.B. Utama, H. Kleemann, W. Zhao, C.S. Ong, F.H. da Jornada, D.Y. Qiu, H. Cai, H. Li, R. Kou, S. Zhao, S. Wang, K. Watanabe, T. Taniguchi, S. Tongay, A. Zettl, S.G. Louie, F. Wang, A dielectric-defined lateral heterojunction in a monolayer semiconductor, Nat. Electron. 2 (2019) 60–65. https://doi.org/10.1038/s41928-019-0207-4.
- [105] L.H. Li, E.J.G. Santos, T. Xing, E. Cappelluti, R. Roldán, Y. Chen, K. Watanabe, T. Taniguchi, Dielectric screening in atomically thin boron nitride nanosheets, Nano Lett. 15 (2015) 218–223. https://doi.org/10.1021/nl503411a.
- [106] S. Park, T. Schultz, D. Shin, N. Mutz, A. Aljarb, H.S. Kang, C.H. Lee, L.J. Li, X. Xu, V. Tung, E.J.W. List-Kratochvil, S. Blumstengel, P. Amsalem, N. Koch, The Schottky-Mott Rule Expanded for Two-Dimensional Semiconductors: Influence of Substrate Dielectric Screening, ACS Nano 15 (2021) 14794–14803. https://doi.org/10.1021/acsnano.1c04825.



- [107] D. Tebbe, M. Schütte, K. Watanabe, T. Taniguchi, C. Stampfer, B. Beschoten, L. Waldecker, Tailoring the dielectric screening in WS₂–graphene heterostructures, NPJ 2D Mater. Appl. 7 (2023) 29. https://doi.org/10.1038/s41699-023-00394-0.
- [108] H. Yu, Y. Wang, H. Zeng, Z. Cao, Q. Zhang, L. Gao, M. Hong, X. Wei, Y. Zheng, Z. Zhang, X. Zhang, Y. Zhang, High-Spike Barrier Photodiodes Based on 2D Te/WS₂ Heterostructures, ACS Nano 18 (2024) 17100–17110. https://doi.org/10.1021/acsnano.4c03729.
- [109] L. Britnell, R.M. Ribeiro, A. Eckmann, R. Jalil, B.D. Belle, A. Mishchenko, Y.-J. Kim, R. V Gorbachev, T. Georgiou, S. V Morozov, A.N. Grigorenko, A.K. Geim, C. Casiraghi, A.H. Castro Neto, K.S. Novoselov, Strong Light-Matter Interactions in Heterostructures of Atomically Thin Films, Science 340 (2013) 1311–1314. https://doi.org/10.1126/science.1235547.
- [110] J. Wong, D. Jariwala, G. Tagliabue, K. Tat, A.R. Davoyan, M.C. Sherrott, H.A. Atwater, High Photovoltaic Quantum Efficiency in Ultrathin van der Waals Heterostructures, ACS Nano 11 (2017) 7230–7240. https://doi.org/10.1021/acsnano.7b03148.
- [111] P. Hu, L. Wang, M. Yoon, J. Zhang, W. Feng, X. Wang, Z. Wen, J.C. Idrobo, Y. Miyamoto, D.B. Geohegan, K. Xiao, Highly responsive ultrathin GaS nanosheet photodetectors on rigid and flexible substrates, Nano Lett. 13 (2013) 1649–1654. https://doi.org/10.1021/nl400107k.
- [112] B. Chitara, A. Ya'Akobovitz, Elastic properties and breaking strengths of GaS, GaSe and GaTe nanosheets, Nanoscale 10 (2018) 13022–13027. https://doi.org/10.1039/c8nr01065j.
- [113] F.D.V. Araujo, V. V. Oliveira, A.C. Gadelha, T.C.V. Carvalho, T.F.D. Fernandes, F.W.N. Silva, R. Longuinhos, J. Ribeiro-Soares, A. Jorio, A.G. Souza Filho, R.S. Alencar, B.C.



- Viana, Temperature-dependent phonon dynamics and anharmonicity of suspended and supported few-layer gallium sulfide, Nanotechnology 31 (2020) 495702. https://doi.org/10.1088/1361-6528/abb107.
- [114] V. Zólyomi, N.D. Drummond, V.I. Fal'Ko, Band structure and optical transitions in atomic layers of hexagonal gallium chalcogenides, Phys. Rev. B Condens. Matter. Mater. Phys. 87 (2013) 195403. https://doi.org/10.1103/PhysRevB.87.195403.
- [115] Y. Lu, J. Chen, T. Chen, Y. Shu, R.J. Chang, Y. Sheng, V. Shautsova, N. Mkhize, P. Holdway, H. Bhaskaran, J.H. Warner, Controlling Defects in Continuous 2D GaS Films for High-Performance Wavelength-Tunable UV-Discriminating Photodetectors, Adv. Mater. 32 (2020) 1906958. https://doi.org/10.1002/adma.201906958.
- [116] T. Chen, Y. Lu, Y. Sheng, Y. Shu, X. Li, R.J. Chang, H. Bhaskaran, J.H. Warner, Ultrathin All-2D Lateral Graphene/GaS/Graphene UV Photodetectors by Direct CVD Growth, ACS Appl. Mater. Interfaces 11 (2019) 48172–48178. https://doi.org/10.1021/acsami.9b11984.
- [117] Y. Lu, T. Chen, N. Mkhize, R.J. Chang, Y. Sheng, P. Holdway, H. Bhaskaran, J.H. Warner, GaS:WS2Heterojunctions for Ultrathin Two-Dimensional Photodetectors with Large Linear Dynamic Range across Broad Wavelengths, ACS Nano 15 (2021) 19570–19580. https://doi.org/10.1021/acsnano.1c06587.
- [118] X. Zhang, R. Li, Y. Yu, F. Dai, R. Jiang, J. Guo, W. Hu, Z. Ni, J. Lu, Dark Current Mechanisms and Suppression Strategies for Infrared Photodetectors Based on Two-Dimensional Materials, Laser Photonics Rev. 18 (2024) 2300936. https://doi.org/10.1002/lpor.202300936.



- [119] X. Zhang, Z. Kang, L. Gao, B. Liu, H. Yu, Q. Liao, Z. Zhang, Y. Zhang, Molecule-Upgraded van der Waals Contacts for Schottky-Barrier-Free Electronics, Adv. Mater. 33 (2021) 2104935. https://doi.org/10.1002/adma.202104935.
- [120] Y. Jung, M.S. Choi, A. Nipane, A. Borah, B. Kim, A. Zangiabadi, T. Taniguchi, K. Watanabe, W.J. Yoo, J. Hone, J.T. Teherani, Transferred via contacts as a platform for ideal two-dimensional transistors, Nat. Electron. 2 (2019) 187–194. https://doi.org/10.1038/s41928-019-0245-y.
- [121] W. Song, L. Kong, Q. Tao, Q. Liu, X. Yang, J. Li, H. Duan, X. Duan, L. Liao, Y. Liu, High-Resolution Van der Waals Stencil Lithography for 2D Transistors, Small 17 (2021) 2101209. https://doi.org/10.1002/smll.202101209.
- [122] X. Zhou, X. Hu, S. Zhou, H. Song, Q. Zhang, L. Pi, L. Li, H. Li, J. Lü, T. Zhai, Tunneling Diode Based on WSe₂/SnS₂ Heterostructure Incorporating High Detectivity and Responsivity, Adv. Mater. 30 (2018) 1703286. https://doi.org/10.1002/adma.201703286.
- [123] Z. Bian, J. Miao, T. Zhang, H. Chen, Q. Zhu, J. Chai, F. Tian, S. Wu, Y. Xu, B. Yu, Y. Chai, Y. Zhao, Carrier Modulation in 2D Transistors by Inserting Interfacial Dielectric Layer for Area-Efficient Computation, Small 19 (2023) 2206791. https://doi.org/10.1002/sml1.202206791.
- [124] D.J. Late, B. Liu, H.S.S.R. Matte, C.N.R. Rao, V.P. Dravid, Rapid characterization of ultrathin layers of chalcogenides on SiO₂/Si substrates, Adv. Funct. Mater. 22 (2012) 1894–1905. https://doi.org/10.1002/adfm.201102913.
- [125] H.S. Ra, M.H. Jeong, T. Yoon, S. Kim, Y.J. Song, J.S. Lee, Probing the Importance of Charge Balance and Noise Current in WSe₂/WS₂/MoS₂ van der Waals Heterojunction



- Phototransistors by Selective Electrostatic Doping, Adv. Sci. 7 (2020) 2001475. https://doi.org/10.1002/advs.202001475.
- [126] C. Jastrzebski, K. Olkowska, D.J. Jastrzebski, M. Wierzbicki, W. Gebicki, S. Podsiadlo, Raman scattering studies on very thin layers of gallium sulfide (GaS) as a function of sample thickness and temperature, J. Phys.: Condens. Matter 31 (2019) 075303. https://doi.org/10.1088/1361-648X/aaf53b.
- [127] W. Zhao, Z. Ghorannevis, L. Chu, M. Toh, C. Kloc, P.H. Tan, G. Eda, Evolution of Electronic Structure in Atomically Thin Sheets of WS₂ and WSe₂, ACS Nano 7 (2013) 791–797. https://doi.org/10.1021/nn305275h.
- [128] P. Chen, T.L. Atallah, Z. Lin, P. Wang, S.J. Lee, J. Xu, Z. Huang, X. Duan, Y. Ping, Y. Huang, J.R. Caram, X. Duan, Approaching the intrinsic exciton physics limit in two-dimensional semiconductor diodes, Nature 599 (2021) 404–410. https://doi.org/10.1038/s41586-021-03949-7.
- [129] S. Yang, Y. Li, X. Wang, N. Huo, J.B. Xia, S.S. Li, J. Li, High performance few-layer GaS photodetector and its unique photo-response in different gas environments, Nanoscale 6 (2014) 2582–2587. https://doi.org/10.1039/c3nr05965k.
- [130] B.J. Carey, J.Z. Ou, R.M. Clark, K.J. Berean, A. Zavabeti, A.S.R. Chesman, S.P. Russo, D.W.M. Lau, Z.Q. Xu, Q. Bao, O. Kevehei, B.C. Gibson, M.D. Dickey, R.B. Kaner, T. Daeneke, K. Kalantar-Zadeh, Wafer-scale two-dimensional semiconductors from printed oxide skin of liquid metals, Nat. Commun. 8 (2017) 14482. https://doi.org/10.1038/ncomms14482.
- [131] G. Iannaccone, F. Bonaccorso, L. Colombo, G. Fiori, Quantum engineering of transistors based on 2D materials heterostructures, Nat. Nanotechnol. 13 (2018) 183–191. https://doi.org/10.1038/s41565-018-0082-6.



- [132] P. Zhang, Y.S. Ang, A.L. Garner, Á. Valfells, J.W. Luginsland, L.K. Ang, Space-charge limited current in nanodiodes: Ballistic, collisional, and dynamical effects, J. Appl. Phys. 129 (2021) 100902. https://doi.org/10.1063/5.0042355.
- [133] Y. Pan, T. Zheng, F. Gao, L. Qi, W. Gao, J. Zhang, L. Li, K. An, H. Gu, H. Chen, High-Performance Photoinduced Tunneling Self-Driven Photodetector for Polarized Imaging and Polarization-Coded Optical Communication based on Broken-Gap ReSe₂/SnSe₂ van der Waals Heterojunction, Small 20 (2024) 2311606. https://doi.org/10.1002/sml1.202311606.
- [134] M. Chen, X. Chen, Z. Wu, Z. Huang, W. Gao, M. Yang, Y. Xiao, Y. Zhao, Z. Zheng, J. Yao, J. Li, An Ultrasensitive Bi₂O₂Se/In₂S₃ Photodetector with Low Detection Limit and Fast Response toward High-Precision Unmanned Driving, ACS Nano 18 (2024) 27579–27589. https://doi.org/10.1021/acsnano.4c08636.
- [135] Y.S. Shin, K. Lee, Y.R. Kim, H. Lee, I.M. Lee, W.T. Kang, B.H. Lee, K. Kim, J. Heo, S. Park, Y.H. Lee, W.J. Yu, Mobility Engineering in Vertical Field Effect Transistors Based on Van der Waals Heterostructures, Adv. Mater. 30 (2018) 1704435. https://doi.org/10.1002/adma.201704435.
- [136] Y. Chen, X. Wang, G. Wu, Z. Wang, H. Fang, T. Lin, S. Sun, H. Shen, W. Hu, J. Wang, J. Sun, X. Meng, J. Chu, High-Performance Photovoltaic Detector Based on MoTe₂/MoS₂ Van der Waals Heterostructure, Small 14 (2018) 1703293. https://doi.org/10.1002/sml1.201703293.
- [137] M.M. Furchi, A. Pospischil, F. Libisch, J. Burgdörfer, T. Mueller, Photovoltaic effect in an electrically tunable Van der Waals heterojunction, Nano Lett. 14 (2014) 4785–4791. https://doi.org/10.1021/nl501962c.



- [138] M. Dai, H. Chen, F. Wang, M. Long, H. Shang, Y. Hu, W. Li, C. Ge, J. Zhang, T. Zhai, Y. Fu, P. Hu, Ultrafast and Sensitive Self-Powered Photodetector Featuring Self-Limited Depletion Region and Fully Depleted Channel with van der Waals Contacts, ACS Nano 14 (2020) 9098–9106. https://doi.org/10.1021/acsnano.0c04329.
- [139] M. Che, B. Wang, X. Zhao, Y. Li, C. Chang, M. Liu, Y. Du, L. Qi, N. Zhang, Y. Zou, S. Li, PdSe₂ / 2H–MoTe₂ Heterojunction Self-Powered Photodetector: Broadband Photodetection and Linear/Circular Polarization Capability, ACS Nano 18 (2024) 30884–30895. https://doi.org/10.1021/acsnano.4c12298.
- [140] S. Wang, D. Yan, J. Ibarra Michel, A. Corletto, A.A. Wibowo, S. Balendhran, H.Y. Lee, S. Byun, S. Kim, K.B. Crozier, P.C. Sherrell, D. Macdonald, J. Bullock, Improved Efficiency in WSe₂ Solar Cells Using Amorphous InO_x Heterocontacts, ACS Nano 18 (2024) 25046–25052. https://doi.org/10.1021/acsnano.4c06525.
- [141] Y. Cen, Y. Tu, J. Zhu, Y. Hu, Q. Hao, W. Zhang, Photoinduced Contact Evolution and Junction Rearrangement in Two-Dimensional van der Waals Heterostructure, Adv. Funct. Mater. 33 (2023) 2306668. https://doi.org/10.1002/adfm.202306668.
- [142] A. Di Bartolomeo, A. Grillo, F. Urban, L. Iemmo, F. Giubileo, G. Luongo, G. Amato, L. Croin, L. Sun, S.J. Liang, L.K. Ang, Asymmetric Schottky Contacts in Bilayer MoS₂ Field Effect Transistors, Adv. Funct. Mater. 28 (2018) 1800657. https://doi.org/10.1002/adfm.201800657.
- [143] Z. Shao, T. Jiang, X. Zhang, X. Zhang, X. Wu, F. Xia, S. Xiong, S.T. Lee, J. Jie, Memory phototransistors based on exponential-association photoelectric conversion law, Nat. Commun. 10 (2019) 1294. https://doi.org/10.1038/s41467-019-09206-w.



- [144] Y. Wang, Z. He, J. Zhang, H. Liu, X. Lai, B. Liu, Y. Chen, F. Wang, L. Zhang, UV illumination enhanced desorption of oxygen molecules from monolayer MoS₂ surface, Nano Res. 13 (2020) 358–365. https://doi.org/10.1007/s12274-020-2614-2.
- [145] W. Tress, K. Leo, M. Riede, Optimum mobility, contact properties, and open-circuit voltage of organic solar cells: A drift-diffusion simulation study, Phys. Rev. B Condens. Matter. Mater. Phys. 85 (2012) 155201. https://doi.org/10.1103/PhysRevB.85.155201.
- [146] M. Zubair, H. Wang, Q. Zhao, M. Kang, M. Xia, M. Luo, Y. Dong, S. Duan, F. Dai, W. Wei, Y. Li, J. Wang, T. Li, Y. Fang, Y. Liu, R. Xie, X. Fu, L. Dong, J. Miao, Gate-Tunable van der Waals Photodiodes with an Ultrahigh Peak-to-Valley Current Ratio, Small 19 (2023) 2300010. https://doi.org/10.1002/smll.202300010.
- [147] P. Zeng, W. Wang, D. Han, J. Zhang, Z. Yu, J. He, P. Zheng, H. Zheng, L. Zheng, W. Su, D. Huo, Z. Ni, Y. Zhang, Z. Wu, MoS₂/WSe₂ vdW Heterostructures Decorated with PbS Quantum Dots for the Development of High-Performance Photovoltaic and Broadband Photodiodes, ACS Nano 16 (2022) 9329–9338. https://doi.org/10.1021/acsnano.2c02012.
- [148] M.Y. Li, Y. Shi, C.C. Cheng, L.S. Lu, Y.C. Lin, H.L. Tang, M.L. Tsai, C.W. Chu, K.H. Wei, J.H. He, W.H. Chang, K. Suenaga, L.J. Li, Epitaxial growth of a monolayer WSe₂-MoS₂ lateral p-n junction with an atomically sharp interface, Science 349 (2015) 524–528. https://doi.org/10.1126/science.aab4097.
- [149] M.L. Tsai, M.Y. Li, J.R.D. Retamal, K.T. Lam, Y.C. Lin, K. Suenaga, L.J. Chen, G. Liang, L.J. Li, J.H. He, Single Atomically Sharp Lateral Monolayer p-n Heterojunction Solar Cells with Extraordinarily High Power Conversion Efficiency, Advanced Materials 29 (2017) 1701168. https://doi.org/10.1002/adma.201701168.



- [150] M. Long, E. Liu, P. Wang, A. Gao, H. Xia, W. Luo, B. Wang, J. Zeng, Y. Fu, K. Xu, W. Zhou, Y. Lv, S. Yao, M. Lu, Y. Chen, Z. Ni, Y. You, X. Zhang, S. Qin, Y. Shi, W. Hu, D. Xing, F. Miao, Broadband Photovoltaic Detectors Based on an Atomically Thin Heterostructure, Nano Lett 16 (2016) 2254–2259. https://doi.org/10.1021/acs.nanolett.5b04538.
- [151] Y. Zhang, H. Su, H. Li, Z. Xie, Y. Zhang, Y. Zhou, L. Yang, H. Lu, G. Yuan, H. Zheng, Enhanced photovoltaic-pyroelectric coupled effect of BiFeO₃/Au/ZnO heterostructures, Nano Energy 85 (2021) 105968. https://doi.org/10.1016/j.nanoen.2021.105968.
- [152] X. Hu, X. Li, G. Li, T. Ji, F. Ai, J. Wu, E. Ha, J. Hu, Recent Progress of Methods to Enhance Photovoltaic Effect for Self-Powered Heterojunction Photodetectors and Their Applications in Inorganic Low-Dimensional Structures, Adv. Funct. Mater. 31 (2021) 2011284. https://doi.org/10.1002/adfm.202011284.
- [153] Z. Wang, R. Yu, C. Pan, Z. Li, J. Yang, F. Yi, Z.L. Wang, Light-induced pyroelectric effect as an effective approach for ultrafast ultraviolet nanosensing, Nat. Commun. 6 (2015) 8401. https://doi.org/10.1038/ncomms9401.